On the Modelling of Solar Radiation in Urban Environments – Applications of Geomatics and Climatology Towards Climate Action in Victoria

by

Christopher B. Krasowski
B.Sc., University of Victoria, 2012

A Thesis Submitted in Partial Fulfillment
of the Requirements for the Degree of

MASTER OF SCIENCE

in the Department of Geography

© Christopher B. Krasowski 2019
All rights reserved. This Thesis may not be reproduced in whole or in part, by photocopy
or other means, without the permission of the author.

On the Modelling of Solar Radiation in Urban Environments – Applications of Geomatics and Climatology Towards Climate Action

by

Christopher B. Krasowski
B.Sc., University of Victoria, 2012

Supervisory Committee

Dr. David E. Atkinson, Department of Geography
Supervisor

Dr. Johannes Feddema, Department of Geography
Member

Abstract

Modelling solar radiation data at a high spatiotemporal resolution for an urban environment can inform many different applications related to climate action, such as urban agriculture, forest, building, and renewable energy studies. However, the complexity of urban form, vastness of city-wide coverage, and general dearth of climatological information pose unique challenges doing so. To address some climate action goals related to reducing building emissions in the City of Victoria, British Columbia, Canada, applied geomatics and climatology were used to model solar radiation data suitable for informing renewable energy feasibility studies, including photovoltaic system sizing, costing, carbon offsets, and financial payback.

The research presents a comprehensive review of solar radiation attenuates, as well as methods of accounting for them, specifically in urban environments. A novel methodology is derived from the review and integrates existing models, data, and tools – those typically available to a local government. Using Light Detection and Ranging (LiDAR), a solar climatology, Esri's ArcGIS Solar Analyst tool, and Python scripting, daily insolation (kWh/m^2) maps are produced for the city of Victoria.

Particular attention is paid to the derivation of daily diffuse fraction from atmospheric clearness indices, as well as LiDAR classification and generation of a Digital Surface Model (DSM). Novel and significant improvements in computation time are realized through parallel processing. Model results exhibit strong correlation with empirical data and support the use of Solar Analyst for urban solar assessments when great care is taken to accurately and consistently represent model inputs and outputs integrated in a methodological approach.

Table of Contents

List of Tables

List of Figures

List of Equations

Glossary

AM	Optical air mass (AM). Used to approximate atmospheric extinction the solar beam encounters relative to its shortest path length at zenith (termed AM1).
DHI	Direct Horizontal Irradiance (or Insolation)
DNI	Direct Normal Irradiance (or Insolation)
ETR	Extraterrestrial Global Horizontal Radiation (or Horizontal Top-of-Atmosphere Radiation). The amount of global horizontal radiation (W/m^2) that a location on Earth would receive if no atmosphere or clouds was present (i.e., in outer space).
ETRN	Extraterrestrial direct normal solar irradiance. Amount of solar radiation (W/m^2) received on a surface normal to the sun at the top of the atmosphere.
GHG	Greenhouse Gases
GHI	Global Horizontal Irradiance (or Insolation)
SC	Solar Constant (World Radiation Center's standard of 1367 W/m^2. Amount of solar radiation received on a surface exposed normally to the sun at one astronomical unit (mean Earth-Sun distance).
Sky Dome	Synonymous with hemisphere, refers to a 2π solid angle sky above a reference surface.
SZA	Solar Zenith Angle. Solar elevation in degrees from zenith (90°) and used to correct for atmospheric diffraction to account for optimal air mass (or atmospheric path length)
TOA	Top-of-Atmosphere Radiation (or Extraterrestrial Radiation). The amount of global horizontal radiation that a location on Earth would receive if no atmosphere or clouds was present (i.e., in outer space). This number is used as the reference amount against which actual solar energy measurements are compared.

Acknowledgments

I acknowledge with respect the Lekwungen peoples on whose traditional territory I have been able to study, and the Songhees, Esquimalt and WSÁNEĆ peoples whose historical relationships with the land continue to this day – Hay’sxw’qa si’em!

A heartfelt thank you to David Atkinson, my academic supervisor – without you, none of this would have been possible. Beyond providing guidance, patience, and expertise along the way, most importantly you believed in me. Being independent research, I acknowledge and respect the risk you assumed when you took me on, and I thank you.

Just as warm of a thank you to Steve Young, my industrial supervisor. The faith and respect you showed me provided the space for our collaboration and innovation to occur – thank you for indulging my idea(s) and the fine work you put into climate action at the City of Victoria – cheers!

A very special thank you to Claude Labine, the Founder and Retired Chief Scientific Officer of Campbell Scientific Canada. Your sponsorship of this research helped realize it, your enthusiasm for the science made it fun, and your kindness, generosity, and thoughtfulness has led to a great friendship that will last for years to come.

This research was funded in part by the Natural Sciences and Engineering Research Council of Canada (NSERC) as part of an Industrial Post-Graduate Scholarship (IPS), the City of Victoria, Campbell Scientific Canada, and the University of Victoria (Graduate Research Award, Sara Spencer Foundation Research Award, W.R. Derrick Sewell Scholarship, and a Graduate Fellowship Award).

Thank you to many of the faculty, staff, and colleagues in the University of Victoria’s Department of Geography – your passion for our craft has helped inspire and shape my academic and personal growth. Thank you to my Climate Lab comrades – Norman, Katie, Weixun, Adam, Mohammed, Eric, Ben, Tuonan, and Vida. Your friendship, banter, support, skills, and company (especially to the Grad House!) will be remembered and appreciated forever.

So many friends have been sources of encouragement, support, debate, and insight over the years that I will not attempt to name any – you know who you are, and thanks eh.

To the families that have helped, befriended, and loved me over the years, thank you from the bottom of my heart. To the Brown, Chalmers, and Freelove families, specifically the matriarchs of those families, please know how important your love has been, and continues to be, for me on this journey – this is for you, because of you, and I cannot thank you enough.

Dedication

I dedicate this work to my late mother – Dawn Bucharski (née Freelove), as well as my grandmother – Yvonne Freelove (née Lucas).

I also dedicate this work to you – the reader. I've followed this path because I was open to it, and strongly encourage anyone reading this to follow the path that calls you, no matter where you originally thought your destination to be – openness is key.

Lastly, I dedicate this work to those on the front lines of climate change research and in the trenches of climate action – your work is imperative, valued, and noble.

"We shall require a substantially new manner of thinking if mankind is to survive"
-Albert Einstein

Introduction

Conversations regarding the urgency and responsibility of acting on climate change have matured over the decades, but at a great cost – to people, the biosphere, and our window of opportunity. The "climate crisis", as it's now referred to, will define this generation for centuries to come, if not millennia, if we do not begin to redress that which got us here in the first place – the anthropogenic emission of greenhouse gases (GHGs).

The Intergovernmental Panel on Climate Change (IPCC) leads the global effort related to the science of climate change, its projected impacts, and possible emission reduction pathways, response options, or in other words – *climate action*. The IPCC has robustly determined that to avoid catastrophic climate-driven impacts, global warming needs to be limited to 2°C above pre-industrial levels, with a strong recommendation that "rapid, far-reaching, and unprecedented changes in all aspects of society" be taken to limit it to 1.5°C (IPCC, 2019). The 2015 Paris Climate Agreement was the instrument that binds 195 nations to this adopting this goal, and commits them to achieving this by 2100.

Limiting global warming to 1.5°C means anthropogenic carbon dioxide (CO_2) emissions must fall "about 45 percent from 2010 levels by 2030, reaching 'net zero' around 2050" (IPCC, 2019). In Canada (a signatory of the Paris Agreement, entering into force November 4th 2016), the current federal government has proposed emissions with a "2030 target of 30% below 2005 levels, which is equal to 523 megatonnes" (Environment and Climate Change Canada, 2016) through its *Pan-Canadian Framework.*

The province of British Columbia (B.C.) has been a provincial climate action leader in Canada for well over a decade. In May 2018, B.C. updated its legislated provincial emissions targets, setting an even more ambitious goal of 40% reductions by 2030 from a 2007 baseline, which is equal to 25.4 megatonnes (Climate Change Accountability Act, 2007). Municipalities and regional districts in B.C. play an important role in realizing provincial targets, and almost every local government in the province has committed to climate action under the B.C. Climate Action Charter (B.C. Climate Action Charter, 2007). In July 2018, the capital of B.C., Victoria, took its Climate Action Charter commitments to new heights with its Climate Leadership Plan (CLP). The CLP is Victoria's plan to achieve an 80% reduction in GHGs, while transitioning to 100% renewable energy, by 2050. To track progress and provide any mid-course corrections, Victoria set an interim target of reducing community GHG emissions by 50% and its corporate emissions by 60%, both from 2007 levels, by 2030 (City of Victoria, 2018).

Victoria's carbon footprint – 370,000 tonnes of CO_{2e}[1] in 2017 – stems largely from its building stock. Approximately 50% of these emissions come from buildings. Though the city currently receives approximately 40% of its energy from renewable (hydroelectric) sources, the rest is primarily from the combustion of heating oil and natural gas (City of Victoria, 2018). For the city to reach its 100% renewable target, it needs to explore incorporating all emission-less power sources to supplement its renewable energy mix, as well as help increase its resilience and energy security in a climate change future.

As has the climate conversation, solar energy technologies have also matured over the years, becoming economically and technically viable sources of large-scale sustainable energy (Wiginton, Nguyen, & Pearce, 2010). In the urban environment, distributed solar technologies such as rooftop photovoltaic (PV) panels or solar hot water (SHW) heaters can be effective means of reducing GHGs of buildings. Moreover, research has shown that PV panels can reduce Urban Heat Island (UHI) effects – the phenomenon where an urban environment is relatively warmer than the surrounding rural areas – thereby further reducing emissions. These emission reduction benefits are additional to provisioning renewable energy, and related to decreasing cooling needs through shading, removing energy otherwise available as input to the UHI energy balance, and mitigating UHI during the night by altering the interactions between urban surfaces and the atmospheric layer above a city (Masson, Bonhomme, Salagnac, Briottet, & Lemonsu, 2014).

---

[1] CO_{2e} – The "e" refers to "equivalent", as it relays total GHG effectiveness by accounting for the global warming potentials of all GHG emissions and presents the total in a standardized unit.

Understanding and communicating the solar energy potential of rooftops in an urban environment is a critical first step towards increasing awareness, and ultimately adoption, of solar technologies. Assessing the solar energy potential of an area is referred to as *solar mapping*, and can help sizing a system (PV or SHW), assessing storage needs (if any), developing renewable energy policies, performing cost-benefit analyses, or planning utility and grid capacity needs (Wiginton et al., 2010). As well, this information is useful beyond estimating renewable energy resources, as it can inform vegetation-related (e.g., urban forests, community gardens, green roofs), medical-related (e.g., skin cancer, heat susceptibility), and climate-related (e.g., UHI research, hazard mapping, and climate adaptation) applications. Either way, accurate and precise solar maps of large-scale urban environments provide valuable information with many applications (Manni, Lobaccaro, & Goia, 2018; Yang et al., 2018; Zölch, Maderspacher, Wamsler, & Pauleit, 2016).

The purpose of this research is to model solar radiation data suitable for a high-quality, high-spatiotemporal resolution solar mapping assessment of rooftops throughout the city of Victoria. These data will help facilitate the city’s climate action initiatives related to increasing awareness and uptake of solar energy technologies in an effort to reduce GHG emissions in its built environment. Subsequent goals of this study are:

1) Conducting a comprehensive review of methods for modeling solar energy at the Earth surface, specifically in urban environments.
2) Constructing a methodology in accordance with the review and available data / tools.
3) Executing the methodology while ensuring integrated models support the main purpose of providing high-quality, high-resolution solar maps by focusing on the suitability and representativeness of data and methods used.

The thesis is structured according to the above goals, where: Chapter 1 will provide an exhaustive review of the factors that determine solar radiation received at the Earth surface, as well as discuss modelling approaches to that end; Chapter 2 will present a methodology, the integrated models, and the data used therein; Chapter 3 will present results; Chapter 4 will provide a discussion, and; Chapter 5 will offer a conclusion.

Chapter 1: Solar Radiation at the Earth Surface

Solar Energy

Solar energy is a colloquial term referring to the energy made available from sunlight by processes or technology. More technically, it is the electromagnetic radiation emitted from the Sun, altered spectrally by the Earth's atmosphere and surfaces, and ultimately incident to a reference surface that converts it to a usable form. This definition lends itself well as a framework for introducing some of the context, terminology, and approaches relevant to determining citywide solar potential of rooftops, beginning with:

1) The source of energy (the Sun);
2) The amount received by Earth (Sun-Earth geometry);
3) Its path through atmosphere towards a surface of Earth (solar cascade), and;
4) Quantifying the irradiance incident to a surface (solar energy modelling).

The Sun

The Sun is a star (a luminous sphere of gaseous plasma held together under its own gravity) at the centre of our Solar System. It formed from the gravitational collapse of matter in a molecular dust cloud roughly 4.6 billion years ago (Bonanno, Schlattl, & Paterno, 2002). This collapse led to the density and heat required to catalyze perpetual thermonuclear fusion of the Sun's main constituent of hydrogen (~73% of total mass) to its heavier nucleic form of helium (~25% of total mass) (Eddington, 1926). This constant reaction is the extraterrestrial radiative engine (or primary exogenic force) that drives all climate and life on Earth (Versteegh, 2005). Consequently, the Sun has long since been an object of humankind's interests.

Some cultures regarded the Sun a deity, while others simply looked to it as a timepiece; they all, however, physically observed it the same – as a static, homogenous disc of light (Hathaway, 2010). Galileo's time (~1600s) began to shed light on the dynamic nature of the Sun by turning telescopes towards studying sunspots; Arthur Eddington wrote *The Internal Constitution of the Stars* (1926) which sought to explain the Sun's plasmatic and nuclear inner workings through theoretical physics; in 1962 the field of helioseismology began studying solar oscillations to better map regions and interior dynamics (Basu & Antia, 2008); and since 1996, the international Solar and Heliospheric Observatory (SOHO) has been observing the Sun in great detail with sensors specifically designed to study its deep core, corona, and solar winds (NASA, 2015). Today, humankind has an unprecedented level of precision and accuracy with which to comment on the Sun's structure and dynamics.

Structure

The Sun's interior is divided into three main categories (core, radiative, and convective zones) delineating regional energy flows. The core is the reactor, where the temperature and pressure is sufficient for nuclear fusion of hydrogen to occur; the radiative zone is where energy transfers via thermal radiation to an outward point in which it can begin to convect; the convective zone is where the outward heat transfer continues, similar to cells in Earth's atmosphere. Outside the convective zone is the Photosphere (or the Sun's "surface"), where visible light above this point is free to propagate to space. Outside the Photoshere is the Sun's atmosphere, which is comprised of four parts: the *chromosphere*, *transition region*, *corona*, and *heliosphere* (Figure 1).

The visible light arriving at Earth's surface is from the Photosphere – this is what is perceived as light from the Sun on the surface of the Earth. The Photosphere was first observed as a penumbral halo during the totality of a solar eclipse (Stewart & MacCracken, 1940). The constant chaos of this region plays an important role in creating space weather:

- *Sunspots* occur as dark patches on the photosphere of relatively cooler plasma surrounded by brighter (hotter) plasma called *granules* (Hathaway, 2010);
- *Spicules* jettison dense gas from the chromosphere region;
- *Coronal mass ejections* (CMEs) and *solar flares* eject massive amounts of plasma from sunspots and other active areas of the photosphere to space (NASA, 2015);
- *Faculae* and *plages* appear on the surface and chromosphere (respectively) as bright convection cells and significantly vary the radiation emitted to space (Gueymard, 2004);
- *Prominences* and *filaments* extend cooler plasma outwards forming a loop tethered from the photosphere, to the corona, and back to the surface; and
- *Solar winds* constantly "blow" a flow of plasma from the corona outward to interplanetary space, while *coronal holes* speed this stream of solar wind greatly (UCAR, 2014).

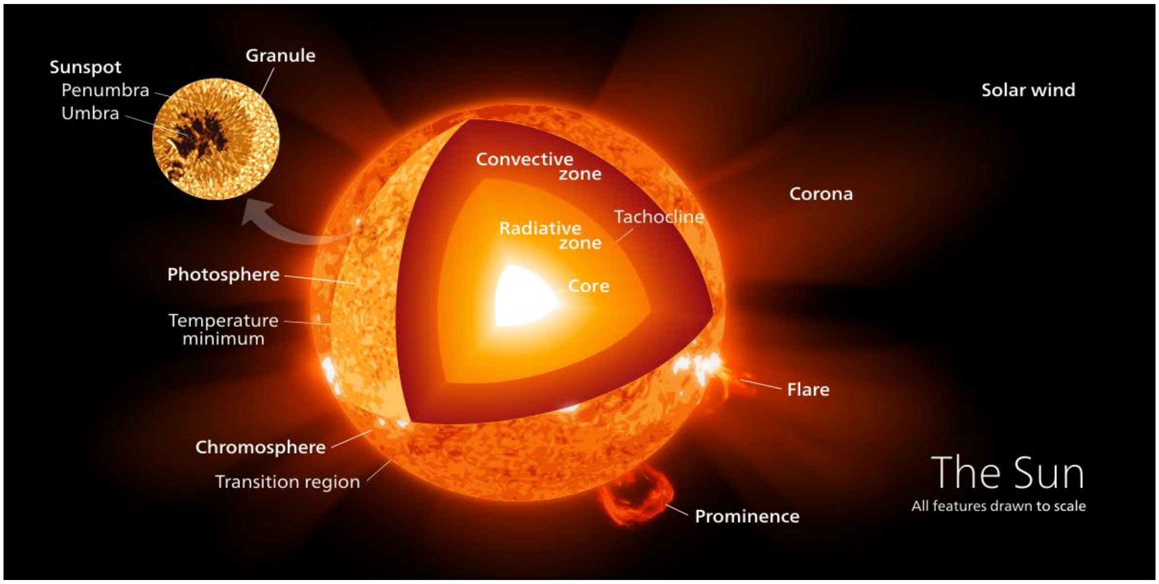

Figure 1 - The Sun's structure and components. "Diagram of the Sun" Kelvinsong [CC BY-SA 3.0 (https://creativecommons.org/licenses/by-sa/3.0)], from Wikimedia Commons

The Sun is not static, nor homogenous; rather, it is a chaotic, gaseous mass of thermonuclear churn that is highly variable over very short time periods. However, over longer time horizons these perturbations average out over space and time while exhibiting some periodicity.

Cycle

Sunspots are visible features occurring on the surface (photosphere) of the Sun. As such, they provide observers foci for marking activity and the Sun's position. Sunspot observations by the naked eye have been reported to occur over 2000 years ago, yet came as a surprise to westerners first turning telescopes on the sun in the 17th century (Vaquero, 2007; Wittmann & Xu, 1988). This can be attributed to western philosophy that the Sun, like the heavens, was perfect and unblemished (Hathaway, 2010).

Christian Horrebow was the first to note a possible pattern of sunspot activity in 1776, but Heinrich Schwabe is credited with discovering the 11-year sunspot cycle with his 1843 report titled *Astronomische Nachrichten* (or "Astronomical News"). Since then, details of the patterns (orientation, grouping, size, and migration about the Sun's surface), "have subsequently been characterized with exquisite observations spanning many decades" (Metcalfe & van Saders, 2017). Describing the nature of these patterns will be left to Astrophysics, but the pursuit of better understanding them led to progress relevant to modelling solar radiation reaching Earth's surface.

Solar Radiation

Solar radiation is electromagnetic radiation emitted by the Sun. The science of measuring electromagnetic radiation is called *radiometry*, and a *radiometer* is an instrument used in its detection. The following radiometric terms will be used in this thesis:

Table 1 - Radiometric Terminology and Units

Quantity	*Unit*	*Abbreviation*	*Description*
Radiant flux	Watt	W	Radiant energy (or power) per unit time
Irradiance (or flux density)	Watt per square meter	W/m^2	Power per unit area
Insolation	Watt per square meter per unit time	W/ m^2 / (time)	Power per unit area integrated over unit time

Any blackbody with a temperature above absolute zero emits radiation. The Stefan-Boltzmann law describes radiant flux being directly proportional to the fourth power of temperature (Equation 1).

Equation 1 - Stefan Boltzmann

$$P = e\sigma T^4$$

Where P = power in W/m^2 or J/s; e = emissivity of object; σ = Stefan-Boltzmann constant: 5.6703 x 10-8 W/m^2 K^4; and T = temperature in Kelvin

Josef Stefan was the first to provide a good estimate of the temperature of the Sun in 1879. He employed what is now known as the Stefan-Boltzmann equation, and calculated the Sun's temperature to be 5700 K, compared to the modern value of 5778 K; his estimate would have been even more accurate had he better estimated atmospheric transmissivity (D. Williams, 2018). Shortly after Stefan's estimate, actual solar measurements were made using ground-based radiometric observations (Abbot, Fowle, & Aldrich, 1913), but accurate measurements only became available with access to space (Hathaway, 2010).

Since 1978, several satellites have been deployed to establish a space-based, composite measurement of solar irradiance referred to as the *Total Solar Irradiance* (TSI). These satellites orbit around Lagrangian points to provide consistent monitoring of solar irradiance using *active cavity radiometers*. TSI is what is formerly known, yet still commonly referred to, as the *Solar Constant* (1367 W/m^2). The term TSI is typically preferred in fields such as astronomy, climate, and atmospheric sciences, as it incorporates variability in the solar output (Gueymard & Myers, 2008a). However, for terrestrial solar energy applications the solar constant tends to be sufficient, as much more variation occurs to irradiance once it enters Earth's atmosphere.

From the pursuit of TSI, we now better understand the type and intensity of irradiance reaching Earth. Solar radiation spans wavelengths from high-energy shorter wavelength X-rays, to low-energy longer wavelength radio waves. Most (97%) solar radiation falls within the spectral range of 290 nm to 3,000 nm, which is commonly referred to as *broadband* solar radiation (Sengupta et al., 2015). Long-term monitoring shows TSI varies about ±1 Wm^2 around the solar constant in an 11-year sun cycle, and about ±4W/m^2 due to shorter-term and less predictable solar events such as CMEs, flares, prominences, and faculae (Gueymard & Myers, 2008a). It is important to note that the TSI is normalized to one astronomical unit (AU) – the average Earth-Sun distance. This is done to remove the effects of Earth's orbital parameters about the Sun, which vary the distance and orientation between the two objects, thus the irradiance that is exchanged.

Sun-Earth Geometry

The last (major) exogenic influence on solar radiation reaching the top of Earth's atmosphere – referred to as the *Top of Atmosphere* (TOA) irradiance – is the astronomical relationship between the Sun and Earth. Gravitational interactions since the evolutionary genesis of our solar system have led to variations in the eccentricity, axial tilt, and precession of Earth's orbit about the Sun, resulting in cyclic differences in the solar radiation reaching Earth. There are other nuanced, more complex, orbital variations, but these three are the most impactful. Known today as the *Milankovich Cycles*, their combined effects have compounded over time, imparting significant influence over Earth's climate.

Milutin Milanković dedicated his career as a professor (1909 - 1958) in Mathematics at the University of Belgrade to developing a theory relating Sun-Earth geometry and long-term climate change. In 1941, and springboarding from the work of Joseph Adhemar and James Croll, Milanković formulated a mathematical model of latitudinal differences in insolation for the 600,000 years prior to 1800. His work went largely ignored until 1976, when deep-sea sediment cores (that capture unperturbed long-term climate records) were analyzed and found to support his theory that Ice Ages were correlated with Summer insolation regimes driven by Earth's orbital variations about the Sun (Hays, Imbrie, & Shackleton, 1976). The *Milankovich Cycles*, as they have come to be known, are still regarded as "the most thoroughly examined mechanism of climatic change on time scales of tens of thousands of years and are by far the clearest case of a direct effect of changing insolation on the lower atmosphere of Earth" (National Research Council, 1982).

Eccentricity

Eccentricity refers to the shape of Earth's orbit around the sun (Figure 2). Eccentricity varies primarily as a result of the gravitational influence of Saturn and Jupiter. It varies between more elliptical (its *highest* eccentricity = 0.0576) and near circular (its *lowest* eccentricity = 0.0023) over ~413,000-year major, and ~100,000-year minor, cycles.

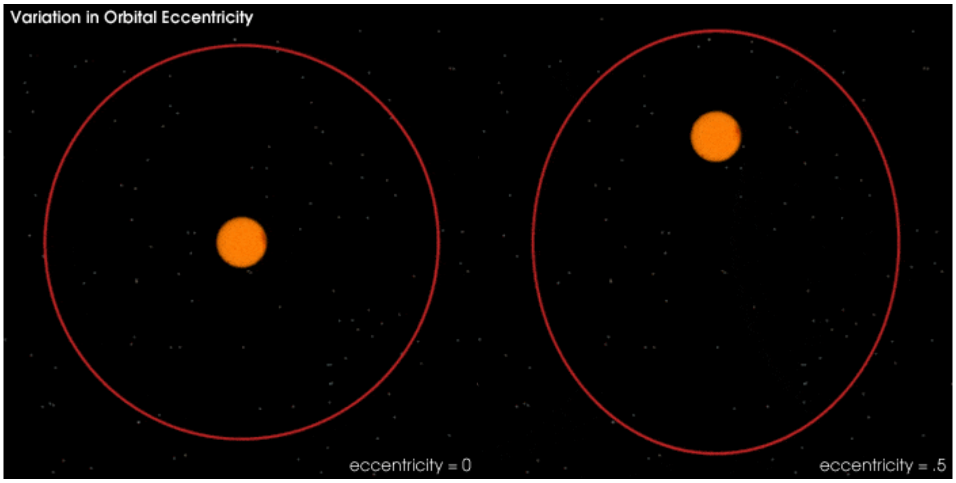

Figure 2 - Eccentricity of Earth's orbit. "Variation in Orbital Eccentricity" NASA, Mysid [Public domain]

The radiation exchanged between two objects is a function of the distance between them, as described by the inverse square law which states that the propagation of electromagnetic radiation in the vacuum of space is inversely proportional to the square of the distance from the source, or:

Equation 2 - Inverse Square Law

$$I = \frac{1}{d^2}$$

> Where I = intensity of energy received by an object; d = distance the object is away from the emission source.

This law dictates how small variations in the Earth-Sun distance can have proportionally larger effect on TOA irradiance. Today, the eccentricity of Earth’s orbit is about 0.0167: Earth’s closest approach to the Sun (or perihelion = ~147,100,000 km, resulting in a TOA of 1412 W/m^2) occurs on January 3 and is furthest (or aphelion = ~152,100,000 km and 1321 W/m^2) on July 6, resulting in a ~3% difference in distance and ~7% in TOA irradiance (Paulescu, Paulescu, Gravila, & Badescu, 2013). At Earth’s minimum eccentricity there is a difference of ~1% in TOA irradiance between the perihelion and aphelion of an annual cycle, and at maximum eccentricity the difference is ~17% (Giesen, 2018).

Obliquity

Obliquity refers to the tilt of Earth's axis relative to its orbit (or plane of ecliptic) about the Sun. It is responsible for Earth’s seasons. As obliquity increases, so does the seasonal contrast on Earth, and its effectiveness increases polewards – winters are colder and summers are hotter with more pronounced effects with higher tilt and latitude.

It is postulated that primordial Earth’s obliquity (~70°) was acquired “from the Moon-producing single giant impact at ~ 4500 Ma (approach velocity ≈ 5-20 km/s, impactor/Earth mass-ratio ≈ 0.08 – 0.14)”, and has dissipated to 23.5° over time due to the gravitational moderation of the Moon and Earth’s tidal forces (G. E. Williams, 1993). Today, it varies between 22.1° and 24.5° over a 41,000-year cycle (Figure 3).

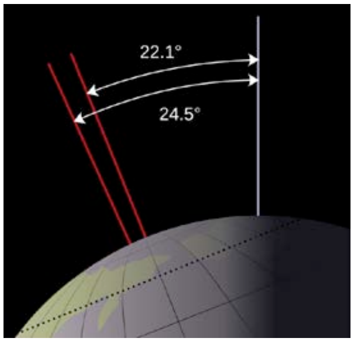

Figure 3 – Obliquity, or Earth's axial tilt. “Earth obliquity range” NASA, Mysid [Public domain]

In terms of insolation, a decrease in obliquity increases mean annual insolation at low latitudes and a decrease at high latitudes. Obliquity does not influence the total amount of insolation received, but does however control its distribution across time and space on Earth (G. E. Williams, 1993).

Precession

Precession refers to the circular revolution (or ‘wobble’) of Earth’s axial tilt of rotation (Figure 4), and to a lesser extent refers to the apsidal precession of the orbital ellipse itself. Precession varies as a result of the gravitational pull exerted by the Sun and Moon on Earth’s equatorial bulge and oceans. It occurs on a period of ~25,700 years, is modulated by eccentricity, and determines where on the ecliptic orbit about the Sun seasons occur. In other words, axial precession alters the dates of perihelion and aphelion, increasing the seasonal contrast in one hemisphere while decreasing it in the other (Zachos et al., 2017).

Presently, the northern hemisphere is tilted toward the Sun when Earth is furthest from it (aphelion), experiencing its summer solstice (June 21), and is tilted away from the Sun when Earth is closest to it (perihelion), experiencing its winter solstice (December 21). At the opposing end of the precession cycle (~13,000 years) this configuration is reversed, and summer solstice in northern hemisphere moves to perihelion while the winter solstice moves to aphelion – increasing the seasonal contrast.

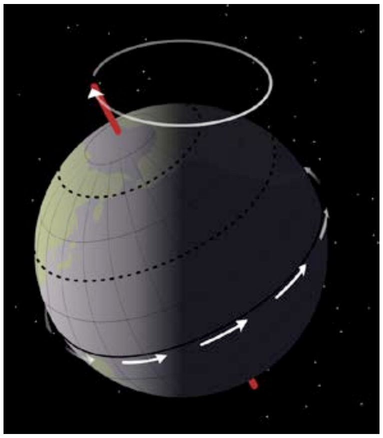

Figure 4 - Precession or "axial wobble". "Earth precession" NASA, Mysid [Public domain]

Combined Effects

The combined effects of eccentricity, obliquity, and precession (the Milankovich cycles) are periodic and quasi-periodic oscillations in the latitudinal distribution of TOA available to Earth. In general, insolation received at the TOA of low-latitudes "is principally affected by variations in eccentricity and precession of the equinoxes. By contrast, higher latitudes are mainly affected by changes in axial tilt (obliquity)" (Hancock, 2000). Eccentricity is the only orbital parameter that can alter Earth's annual insolation, while obliquity and precession vary the hemispherical seasonal contrast over time. Better understanding perturbations in Earth's orbital parameters was crucial to developing perspective on how insolation varies across time and space on Earth.

As the Earth orbits the Sun, spinning about its ecliptic and axial planes, the daily peak solar altitude (*solar noon*) occurs at slightly different points in the sky throughout a year. If from a surface of the Earth a point were placed on the celestial sphere where daily solar noon occurs everyday for an entire year, a figure eight (or infinity) symbol known as an *analemma* would be observed. This image is useful for visualizing how Earth's orbital nuances manifest in annual changes to the sun’s position across the sky, as viewed from the same place on the surface.

Characterizing Extraterrestrial Irradiance

While the Milankovich and solar cycles are important for astronomy and climatology, their explicit use in terrestrial solar resource assessments are impractical, thus rare. Instead, models often assume a static TSI (the solar constant) value ranging between 1361 and 1366 W/m^2 and information regarding geographic position and time of interest (Gueymard & Myers, 2008a). TOA is calculated using well-established trigonometric relationships relating Earth-Sun geometry to a specific time and place on Earth’s surface (Iqbal, 1983). Variations within the TSI and TOA parameters, however, are relatively small compared to larger factors dictating solar radiation’s cascade towards a surface on Earth.

Solar Cascade

As irradiance begins the solar cascade (TOA to a surface on Earth) it interacts with the atmosphere, as well as other surfaces, and becomes modified along the way through absorption and scattering processes. While comprehensive descriptions of these processes and their models are beyond the scope of this thesis, any methodology for quantifying the type and intensity of terrestrial solar radiation, directly or indirectly, accounts for these interactions. Furthermore, describing the solar cascade provides an opportunity to introduce key concepts and terminology.

Concepts and Terminology

As the solar beam cascades through the atmosphere, photons interact with atmospheric constituents and “decompose” (become scattered, absorbed, or transmitted) depending on wavelength:

- Scattered photons are either reflected back to space or continue to cascade producing diffuse sky radiation. Rayleigh (1871), Mie (1908), and Young (1981) provide theories for the mechanics of atmospheric scattering, and collectively explain how photons are scattered as a function of wavelength and the size of atmospheric gases, matter, and water. They explain why sky radiation appears blue, and while light emitted from the solar disk appears yellow, trending towards red as it nears the horizon or encounters particles. Scattering occurs mostly in the shorter wavelengths of the broadband spectrum. Generally, two forms of scattering are responsible for this: *Rayleigh* (where particle size < wavelength) and *Mie* (where particle size ≅ wavelength), with Rayleigh preferentially "scattering out" the shorter wavelength blues and longer wavelength reds, while Mie scattering leads to the whites, greys, and haze associated with pollutants, smoke, and other spherical (or spheroid) particulate matter.

- Absorbed photons increase the internal energy of absorbing molecules, leading to thermal gains. Absorbed photons are not often explicitly accounted for in solar resource assessments, and remain the primary interest of radiative transfer models assessing solar forcing (e.g.: the (re)construction of (paelo)climatologies).

- Transmitted photons are those remaining unabsorbed and unscattered, and make up the still-nearly-collimated beam of light that casts shadows when occluded and contains the majority of radiant flux intensity incident to a surface, also known as direct or beam radiation.

The complex interactions between photons, the atmosphere, and surfaces result in three distinct components of broadband radiation of interest to solar energy technologies:

- *Direct Normal Irradiance* (DNI): The amount of solar radiation received directly from the path of the solar disk. Also called direct, or just “beam” irradiance. This component tends to increase with clear and dry sky conditions. Usually, DNI comprises the majority of the total irradiance reaching a surface. Direct beam irradiance mostly impacts in the 1000-2800 nm region of broadband spectrum (Gueymard & Myers, 2008a). Most solar energy technologies that rely on DNI concentrate the beam using tracking or parabolic troughs, so information on the normal incidence angle is preferred.

- *Diffuse Horizontal Irradiance* (DHI): The amount of solar radiation received as scattered photons from the sky dome on a horizontal surface, not including the DNI component. Also called indirect, or just “diffuse” irradiance. This component tends to increase with atmospheric turbidity, especially in cloudy and wet sky conditions. Otherwise, DHI tends to be a relatively small fraction of total irradiance compared to DNI. Diffuse sky radiation is least impactful in the 1000-2800 nm region of broadband spectrum (Gueymard & Myers, 2008a). Most solar energy technologies are not very as responsive to DHI as they are to the DNI component.

Global Horizontal **Irradiance (GHI or G_H): The total amount of solar radiation from the sum of both the direct and diffuse components received from a hemispherical “sky dome” above a horizontal surface. Also called total, or simply “global” irradiance. This component represents the entire integrated broadband solar spectrum (hence the term *global*) falling on a surface from the hemisphere above it, and also includes any other surface-reflected irradiance (**

- Equation 3); however, practically GHI is said to be the sum of only the direct and diffuse components.

Equation 3 – Global horizontal irradiance available on a horizontal surface.

$$GHI = DNI\cos(\theta_z) + DHI + SR$$

> Where GHI is the global horizontal irradiance; DNI is the Direct Beam; θ_z is the solar zenith angle; and SR is the surface-reflected components (if applicable).

Top-of-Atmosphere (TOA)

Solar radiation reaching the TOA arrives directly from the *solar disk,* subtended to an angle of about 0.5°; thus, it can be considered a quasi-collimated beam of near-parallel irradiance. This is referred to as the *Extraterrestrial Direct Beam*, or simply *"solar beam"*. When measured on a horizontal surface tangential to a point at the TOA it is referred to as *Global Horizontal Extraterrestrial Radiation,* or simply "*Extraterrestrial Radiation"* (ETR). Effectively, ETR is the amount of irradiance an equivalent horizontal plane on Earth *would* receive if there were no atmosphere. As such, it is a commonly used reference value.

The *Solar Zenith Angle* (θ_z) is the angle between zenith and the center of the solar disk. According to Lambert's cosine law, the irradiance on a horizontal plane is proportional to the cosine of the incidence angle, thus:

Equation 4 - Lambert's Cosine Law

$$G_{0H} = G_{0D}\cos\theta_z$$

> Where G_{0H} is the global horizontal extraterrestrial radiation; G_{0D} is the Extraterrestrial Direct Beam; and θ_z is the solar zenith angle.

The compliment of the solar zenith angle is called the *solar altitude*, and is the angle between the horizon and the centre of the solar disk from a reference surface. The Sun's position in the sky determines the amount of atmosphere that ETR must travel on its path towards a surface on Earth.

Atmosphere

Generally, a greater depth of atmosphere results in more scattering and absorption of solar radiation. The distance travelled by the solar beam from TOA to surface is referred to as the *atmospheric path length*. As solar altitude and azimuth continually change, so too does the path length and incidence angle of the incoming solar beam, and consequently, the type and intensity of irradiance reaching a reference surface.

Atmospheric Depth

A proxy measure for the effective depth of atmosphere is called the *optical air mass* (AM). AM is a ratio used to approximate atmospheric extinction (or *attenuation*) the solar beam encounters relative to its shortest path length at zenith (termed *AM1*). Disregarding the curvature of the Earth, AM is easily calculated (Equation 5). A standard value used as a first order approximation of the performance of solar technologies under "standardized conditions" is AM1.5, and assumes a receiving surface tilt of 37° towards the equator, a solar zenith angle of ~48.2°, and specific ozone, spectral, and water vapour properties (Paulescu et al., 2013).

Equation 5 - Optical Airmass on a Flat Earth

$$AM \approx \frac{1}{\cos \theta_z}$$

Where AM is the optical air mass; and θ_z is the solar zenith angle.

Atmospheric Components

Features of Earth's atmosphere decompose the solar beam in different ways. Though detailing the intricacies of transmittance, absorption, and scattering of solar radiation in the atmosphere are not the intent of this research, any methodology quantifying terrestrial solar potential will need to account for, *directly or indirectly*, the following atmospheric components:

1. Gases

   Atmospheric gases – namely H_2O, CO_2, O_3, and O_2 – scatter and absorb solar radiation (Figure 5). Due to gases alone, even a cloudless "clear sky" can attenuate the solar beam to ~75% of ETR (~ 1000 W/m^2) before it reaches a surface. To account for molecular gases, the concept of a *Rayleigh optical depth* (or a clean, dry, so-called *Rayleigh* atmosphere) can be calculated for a given AM using Beer's law to estimate atmospheric extinction from gases (Kasten & Young, 1989; Young, 1980). Aside from water vapour, these constituents are fairly consistent across space and time and readily estimated to a good level of accuracy.

2. Aerosols

   Liquid and solid particles in the Earth's atmosphere are called *aerosols* (e.g.: SO_2, HCl, pollen, soot, smoke, ash, and dust) and cause atmospheric turbidity that selectively scatters and absorbs solar radiation, as well as changes the physical and radiative properties of clouds. They can be from naturally occurring or anthropogenic sources. Aerosols are thought to be comparable in magnitude, but opposite in sign, to the radiative forcing of GHGs (Power, 2003).

   To account for extinction of the solar beam due to aerosols the concepts of a *Linke turbidity factor* (Linke, 1922) for broadband, or the Ångström / Schüepp's (Ångström, 1924; Schüepp, 1949) coefficients for spectral-specific, turbidity can be calculated and compared to a dry and clean (or *Rayleigh*) atmosphere (Kasten, 1996; Remund, Wald, Lefevre, & Ranchin, 2003; Gueymard, 2012). Direct measurement of aerosols can be achieved using ground, air, or space-borne remote sensing techniques, with NASA's MODerate resolution Imaging Spectrometer (MODIS) sensor being one of the more popular means as it provides longterm, globally contiguous datasets of aerosol properties that tend to correlate well with ground-based observations (Kumar, Singh, Anshumali, & Solanki, 2018).

3. Clouds

Clouds are liquid or crystalline water aloft that selectively scatters and absorbs photons as a function of their droplet size: reflecting ~20% of solar beam back to space when comprised of relatively smaller droplets or selectively absorbing ~20% (mostly in the longer, infrared wavelengths) if comprised of larger droplets (Gurtuna & Prevot, 2011; Hammer et al., 2003). Clouds are very dynamic, forming at the interplay of complex physical and radiative feedbacks in the Earth-Ocean-Atmosphere system, primarily driven by solar radiation (Quante, 2009). Cloud formation is accelerated by aerosol concentrations, which can act as seeds (or *cloud condensation nuclei*) for water vapour to condense and accumulate on. When present, clouds are the dominant atmospheric attenuate of irradiance and most variable across both space and time.

Gauging cloudiness has historically been achieved using sky observations of *total cloud cover* (the fraction amount – tenths or oktas – of cloud covering the sky dome). However, many more variables factor into the effective attenuation of irradiance by clouds (e.g.: elevation, droplet size, aerosol concentration, layering, and optical properties). Today, space-borne remote sensing is the most popular tool for estimating cloud characteristics, with efforts such as the International Satellite Cloud Climatology Project (ISCCP), CloudSat, and the Cloud-Aerosol LiDAR and Infrared Pathfinder Satellite Observations (or *CALIPSO*) providing spatiotemporally contiguous datasets that characterize not only cloud coverage, but also the physical, optical, and radiative properties of the entire vertical profile of Earth's atmosphere since 1982 (Rossow & Schiffer, 1999; Stephens et al., 2002). Even with such data, determining the atmospheric attenuation of irradiance due to clouds poses a significant challenge for solar resource assessments due to their complexity and extreme variability across time and space.

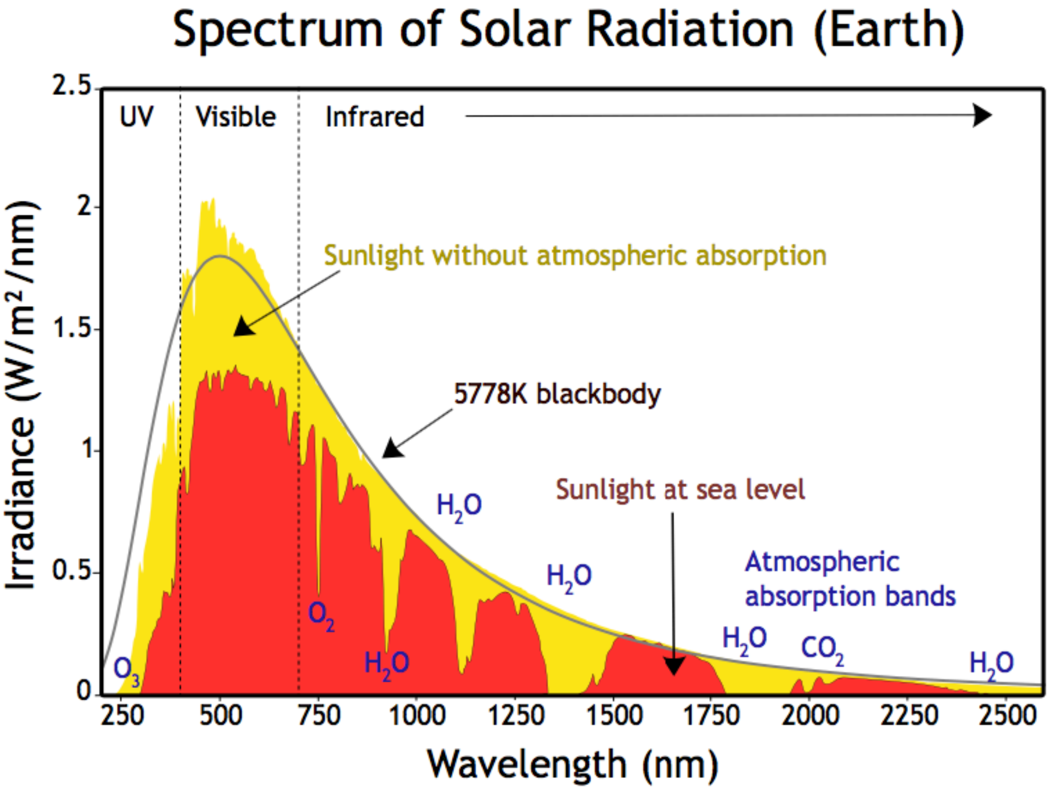

Figure 5 – The solar spectrum as a blackbody (black line), as at the TOA (yellow), and at the Earth's surface (red) after being attenuated by the various atmospheric constituents. "Solar spectrum en" Nick84 [CC BY-SA 3.0 (https://creativecommons.org/licenses/by-sa/3.0)], from Wikimedia Commons

Characterizing the Atmosphere

Quantifying atmospheric constituents and their effective attenuation of the solar beam as it transits the atmosphere is a challenge typically assumed by only those interested in modelling physical radiative transfer properties. For solar potential mapping purposes, directly accounting for the stochastic nature of water vapour, aerosols, and clouds is not only extremely difficult, but also spurious, as the goal is to shed light on the type and intensity of solar flux reaching a reference surface, and not focus on the processes by which it arrived, *per se*. Instead, the atmosphere is characterized more generally using indices to account for the wholesale attenuation of the solar beam on its cascade towards a surface.

Atmospheric Clearness

A convenient means of generalizing the atmospheric attenuation of solar beam is using the *Atmospheric Clearness Index* (Kt), or simply *"clearness index"*. The clearness index is an empirical value. It is defined as the ratio of global horizontal irradiance over global extraterrestrial horizontal irradiance (Equation 6). Using this approach, the effective attenuation from all atmospheric constituents are integrated within one index value, which should theoretically fall between 0 – 1 (0 least clear and 1 being most clear). This approach is simple, feasible, and appropriate for solar resource assessments, as it is easy to calculate, GHI is a readily available parameter from most weather stations, and provides a priori information of atmospheric attenuation without the complexities of a posteriori observation. Short-term Kt is known to express bimodal behaviour, especially in minutely or hourly intervals, where clear or cloudy states dominate measurements with the passing of clouds; to a lesser extent, bimodal behaviour is said to be observed partly for daily clearness index (Woyte, Belmans, & Nijs, 2007).

Equation 6 – Atmospheric Clearness Index

$$K_t = \frac{G_H}{G_{0H}}$$

Where G_H = global horizontal irradiance (W/m2) and G_{0H} = global extraterrestrial horizontal irradiance (tangential to the top-of-atmosphere).

Diffuse Fraction

Where the atmospheric clearness index provides an idea of transmissivity (thus intensity of irradiance), *Diffuse Fraction* (Kd) provides a characterization of type (specifically the diffuse component). Since GHI is the sum of diffuse and direct irradiance, to know diffuse fraction is also to know the direct component (neglecting reflected). Diffuse fraction is typically a derived value. It is defined as the fraction of GHI reaching a surface via scattering processes. To measure diffuse fraction, a pyranometer with a shadowband or a pyrheliometer in conjunction with a global radiation measurement from the same location are used. If derived, it is either a product of a parametric approach using meteorological data inputs (cloudiness, air mass, turbidity, etc.), or more commonly, the result of a decomposition model that uses Kt as input to calculate Kd, based on diffuse-global correlations between the two empirical parameters.

Liu and Jordan (1960) wrote the seminal work for universally deriving Kd from Kt. Since then, some have attempted to improve the approach by incorporating other predictor variables. Reindl, Beckman, and Duffle (1990) demonstrated a 14% reduction in residual sum of squares error when temperature, relative humidity, and solar altitude were factored alongside Kt. However, 86% accuracy using only Kt, as well as the convenience and efficiency gains requiring only one dataset, are reasons why the majority of diffuse-to-global models focus on Kt as the sole input. Today, there exist many diffuse-to-global solar radiation models for hourly, daily, and monthly correlations.

Jacovides, Tymvios, Assimakopoulos, & Kaltsounides (2006) conducted a broad review of the literature and distilled what they propose to be 10 “standard models” for calculating Kd from Kt. They tested their hourly model against the ten and concluded that all the standard models yield Kd with statistically significant accuracy. Moreover, they propose the standard models are location-independent, and that the major disparity between correlations can be attributed to how each model accounts for solar altitude around sunrise-sunset hours (Jacovides et al., 2006). That said, Stan Tuller reminds us that, “no single form of [an] equation is applicable to all atmospheric environments” (1976). Thus, it is considered best practice to test a variety of models in one location (or one model in a variety of locations) to assess their suitability even if location-independence (or *universality*) is claimed.

Surfaces

Urban Canopy

Surfaces of Earth itself represent the last major determinant of irradiance in the solar cascade, and in many cases represent the main factor determining the distribution of irradiance throughout a city (Hofierka & Suri, 2002; Tooke, Coops, Christen, Gurtuna, & Prévot, 2012). The elevation of a surface determines the thickness of atmosphere above it, while its inclination and azimuth determine the incidence angle and aspect of incoming solar radiation, respectively. In the absence of an atmosphere and other surfaces, well-established trigonometric relationships readily predict the irradiance incident on a surface. *An introduction to Solar Radiation* by Muhammad Iqbal provides a comprehensive set of related calculations (1983).

In urban environments, however, surrounding topography (i.e.: other surfaces) – natural or built – can absorb (and shade) or scatter incoming solar radiation, modifying the type and intensity ultimately incident on a surface of interest. Given the diurnal and annual cycles of the sun's transit across a local sky, incoming solar radiation relative to a surface of interest can pass through a kaleidoscope of urban surfaces, depending on the time of day and year. The assemblage of a city's built and natural features – buildings, terrain, trees, infrastructure, and space composing a "town" – form what is known as the *urban canopy* (American Meterological Society, 2019).

Built Environment

The built environment of cities, or its *urban form*, is extremely complex, multi-faceted, heterogeneous, and constantly changing. Characteristics of the urban form such as building height, density, street canyon geometry, orientation, and materials can vary greatly, and all factor in to the irradiance ultimately received on a surface of interest (Landsberg, 1981; Oke, Johnson, Steyn, & Watson, 1991). The surface *albedo* (a measure of reflection) of glazing, fenestration, alloys, and light-coloured material, for example, can scatter irradiance throughout the urban canopy in complex ways, making it very difficult to directly account for. Consequently, this *reflected* component is generally neglected in solar resource assessments or assumed to be a relatively small fraction of the broadband radiation (Ratti, Baker, & Steemers, 2005).

Natural Environment

The natural environment of cities (e.g.: gardens, street trees, parks, and natural areas), or its *vegetation canopy*, can be quite complex and varied in distribution, type, and ephemerality. In Vancouver, it was shown that the vegetation canopy can be a significant factor in determining urban solar potential by reducing the irradiance reaching residences by an average of 38% (Tooke, Coops, Voogt, & Meitner, 2011). Such influences have a seasonal component, as inter-annual differences in solar altitude and phenological cycles can greatly alter the role that vegetation canopy plays in determining irradiance throughput to roofs.

Surfaces: Broader Energy Implications for Urban Climatology

From an urban climatology perspective, surfaces are critically important to understand and account for as they are the “principal sources and sinks of heat, mass, and momentum” (Voogt & Oke, 1997). As such, cities around the world are operationalizing urban climatology focused on using built and natural surfaces as climate action strategies (Webb, 2017).

The climatological influence of the urban form extends beyond its affect on solar radiation received on a surface of interest. Characteristics such as surface roughness, albedo, aspect, moisture availability, and morphology modify the urban *energy* balance, affecting the whole boundary layer driving local-scale temperature, precipitation, wind, and air quality regimes (Christen & Vogt, 2004; Voogt & Oke, 1997; Wilby, 2008). These surface characteristics represent the levers which planners, policy makers, and engineers can toggle to adjust surface energy balances, and by extension, the air temperature of cities. A non-exhaustive set of approaches that use surfaces to reduce the air temperature of urban environments include:

- Focus on block density and canyon morphology (Lindberg & Grimmond, 2011; Radhi, Sharples, & Assem, 2015; Ratti et al., 2005; Robinson & Stone, 2004; Santamouris, 2018);
- Implementation of high-albedo and retro-reflective materials (Krayenhoff & Voogt, 2010; Manni et al., 2018; Sailor, 2010).
- Use of phase change material as a means of storing latent heat (Cui, Xie, Liu, Wang, & Chen, 2017).
- Availability of surface and bio-entrained water sources for evapotranspirative benefits (Zölch et al., 2016).

The climatological influence of the vegetation canopy, particularly as a climate action strategy, is becoming increasingly understood by cities around the world (Bonan, 2016). Many are leveraging this understanding towards a well-planned urban ecosystem to help mitigate UHI effects and adapt to climate change (H Akbari, 2002; Hashem Akbari & Konopacki, 2004; Shashua-Bar & Hoffman, 2003). Some approaches include:

- Increasing green infrastructure and green roofs (Yang et al., 2018);
- Planting vegetation better suited to forecasted shifts in climate (National Research Council, 2013);
- Strategic placement of shade trees for passive cooling of buildings (McPherson & Simpson, 2003; Simpson, 2002; Tooke et al., 2011; Zölch et al., 2016); and
- The densification of urban forests to help retain moisture, cool through evapotranspiration, and alter aerodynamic energy in the urban canyon (Heisler, 1986; Oke, Crowther, McNaughton, Monteith, & Gardiner, 1989).

Thus, both built and natural surfaces shape the urban climate, creating microclimates that vary temperature, winds, precipitation, and radiation fluxes from their synoptic contexts (Givoni, 1989; Lindberg & Grimmond, 2011). In an era of increased urbanization and climate literacy/urgency, cities are paying closer attention to, and taking action on, how the urban canopy affects more than its skyline (Webb, 2017).

Surfaces vis-à-vis Solar Mapping

For solar resource assessments, it is the *surface geometries* of the urban canopy that are of most significance, as they represent both a potential source of shade to other surfaces, as well as the ultimate reference surface of interest. In this sense, the urban canopy acts as both a dependent and independent variable, and makes accounting for its morphological details paramount to rendering high-resolution solar potential maps with any precision or accuracy.

Characterizing Surfaces

Given the structural complexities of the urban canopy, the need for high-resolution morphological details, as well as the large-scale areas involved in citywide solar assessments, remote sensing technologies are particularly well suited to characterizing surfaces at the city scale. There are two general types of remote sensing technologies: active (emit energy) and passive (detect energy) sensors. Though passive sensors (e.g.: satellite optical imagery and airphotos) are increasingly capable (Ouma, 2016) of rendering 2.5D urban environments such as Google Earth with impressive precision (Wen et al., 2019), their spatial resolution and ability to characterize occluded, textural, and angular nuances are outperformed by light detection and ranging (LiDAR), an active sensor technology (Sadr, 2016).

LiDAR is like radar, but instead of acoustical (radio) energy the sensor emits a short pulse of high-resolution light energy (lasers) and measures its return time to the sensor in order to “echo-locate”, or *range*, an object. Most airborne LiDAR sensors these days can provide horizontal and vertical accuracy within a couple centimeters (Liu, 2008). The result is a 3D *point-cloud* that represents every discreet interaction of a laser pulse with *something* at *some* x/y/z location in *some* geo-referenced Euclidean space; though that is all that is known. Nonetheless, a single, discreet laser pulse can penetrate small enough gaps in surfaces such that it provides multiple returns from a single pulse. This can be exploited to infer further information to help distinguish between impermeable surfaces, ground, and vegetation properties (Hung, James, & Hodgson, 2018), as well as vegetation heights, densities, and even extinction coefficients (Tooke et al., 2012). Using the return intensity of LiDAR data, it is possible to infer deciduousness, and even some species, of vegetation (Brandtberg, 2007; Höfle, Hollaus, & Hagenauer, 2012; Kim, Schreuder, McGaughey, & Andersen, 2008; Korpela, Tokola, Orka, & Koskinen, 2009; Liang, Hyyppä, & Matikainen, 2007; Reitberger, Krzystek, & Stilla, 2008).

Coupled with imagery or other spectral information, even richer identification of vegetation is possible. Information on surface reflectance (optical or multi/hyperspectral imagery) integrated with surface geometries can help distinguish vegetation types and phenological states (Rottensteiner, Trinder, Clode, & Kubik, 2007; Secord & Zakhor, 2007; K. Wang, Wang, & Liu, 2018), allowing for more accurate solar models by identifying trees and periods where foliage is not always present to attenuate irradiance from reaching a surface below. However, these value-added approaches increase complexity and costs associated with further analysis and the need for more data to corroborate and/or ground-truth phenology and/or species inferences (Jones, Coops, & Sharma, 2010). For solar mapping purposes, a typical approach is to use LiDAR flown during leaf-on conditions and assume all vegetation is evergreen and opaque; this is both economical and convenient, as well as shown to only underestimate total irradiance by an average of 4.3% in “areas selected to represent the general range of North American urban form types” (Tooke et al., 2012).

The process of characterizing discreet points in a point cloud as part of distinct, topologically related features (e.g.: buildings, trees, roads, power lines, etc.) is known as *LiDAR classification* (or feature extraction). Various algorithmic and human-interpreted methods exist to classify LiDAR (Goodwin, Coops, Tooke, Christen, & Voogt, 2009; Höfle et al., 2012; Hung et al., 2018; Jochem, Höfle, Wichmann, Rutzinger, & Zipf, 2012; Mallet, Soergel, & Bretar, 2008; Rutzinger, Höfle, Hollaus, & Pfeifer, 2008). Distinguishing points as features by classifying LiDAR allows for their explicit inclusion (or exclusion) in methods of representing surfaces of the urban canopy.

A common method of representing surfaces is to interpolate points to form a 2.5D[2] raster layer known as a digital elevation model (DEM). A DEM is a topographical surface where each x, y (location) corresponds to a z (elevation). A digital surface model (DSM) is a DEM of the top-most points in a scene. Thus, an urban DSM, representing the highest points of the built and natural environments, is effectively a surface representation of the urban canopy. When ground returns are aggregated to form a contiguous surface representing the ground (or terrain), the resulting DEM is referred to as a digital terrain model (DTM). Using classified LiDAR, distinct DEMs can be generated for specific classes allowing for their control as variables in the modelling space. This can provide insights into their effects such as that of urban vegetation on surface irradiance, for example (Tooke, 2009). For solar resource assessments of rooftops, the DSM is of primary interest.

Solar Energy Modelling

As knowing the type and intensity of solar radiation data reaching the Earth's surface is of interest to a wide variety of fields (e.g.: meteorology, climatology, engineering, agriculture, and ecology), there exists an equally diverse range of spatial, temporal, and spectral scales sought from a solar energy model. Rooftop solar potential of the urban environment requires an idea of high-quality GHI and/or DNI data, preferably at high spatiotemporal resolution (at least daily insolation per m^2). This "requires sophisticated modeling tools and spatial data representing the complexity of the urban environment", as well as an idea of rapidly changing local atmospheric conditions (Hofierka & Kaňuk, 2009). These tools and data have not always been available, and due to complexity of urban form, spatial coverage needed for city-wide assessments, general lack of input data (radiometric or climatological), and technological limitations in sensors and processing power, modelling rooftop solar potential to a high spatiotemporal resolution is still challenging (Sengupta et al., 2015).

---

[2] Technically, these surface models are only 2.5D, as they exist in 3D space but are limited in representing certain 3D shapes, such as overhangs or alcoves, where their inner fidelity evaded the airborne sensor (Jochem et al., 2009).

Approaches

Ground observations of irradiance provide “ the most accurate method for characterising the solar resource of a given site. However, despite the availability of ground databases is growing up through different measuring networks, its spatial density is usually far too low” (Zarzalejo, 2008). As a result, solar modelling approaches evolved to use indirect or calculated measurements of ground data, which tend to rely on advancements in technology to facilitate spatial, temporal, and/or radiometric improvements (Badescu, 2008b). Approaches can be categorized into the following general approaches:

Modelled and Interpolated Data Sets

Modelled datasets incorporating long-term, ground-observed irradiance measurements can be used to construct a *solar climatology* of radiations fields across space and time (Kafka & Miller, 2019). Forecasted values of irradiance based on a solar climatology are not expected to be identical to the historical time series, but it is reasonable to assume that their properties be statistically similar (Tovar-pescador, 2008; Wilks, 2011). Underlying this notion is the concept of *stationarity* (i.e.: *weak stationarity*), which implies that the mean and autocorrelation functions do not change over time. For example, on an infinitely long time axis, insolation is a *stationary ergodic process* comprised of both stochastic (intermittent atmospheric variables such as aerosols, clouds, and water vapour) and deterministic (geometric and astronomical variables such as eccentricity, and slope/aspect of receiving surface) phenomenon. However, the shorter the time interval, the more likely that stochastic process signals will dominate, and the interval will exhibit non-stationarity (Tomson, Russak, & Kallis, 2008). One solution to account for this is to stratify the data. When comparing equivalent time intervals binned into subsets short enough to be considered nearly stationary, such as monthly or even daily subsets of insolation, stationarity is inherently accounted for by being comparable within each strata (Gordon & Reddy, 1988; Wilks, 2006). Solar climatologies, however, are rare as the spatiotemporal density to construct them is typically not available.

In the absence of dense measurements, sparse irradiance data can be used as points to inform various interpolation methods (spline, weighted average, or more typically – kriging) for creating a continuous field to GHI from (Alsamamra, Ruiz-Arias, Pozo-Vázquez, & Tovar-Pescador, 2009; Hans Georg Beyer, Czeplak, Terzenbach, & Wald, 1997; Hay, 1986; Şen & Şahin, 2001; Zelenka et al., 1992; Zelenka, Perez, Seals, & Renné, 1999). Historically, the Campbell Stokes sunshine duration recorder was a popular instrument that concentrated beam irradiance to burn a heliograph and used in the interpolation of monthly mean GHI for large areas (Badescu, 2008a). Today, increases in the accuracy, precision, and proliferation of pyranometers has allowed for higher quality surface irradiance datasets, such as “the National Solar Radiation Database (NSRDB), the Swiss Meteotest METEONORM data set, the European Solar Radiation Atlas (ESRA), the National Aeronautics and Space Administration (NASA) surface meteorology and solar energy (SSE), and the European Commission’s solar data (SODA) data sets” (Sengupta et al., 2015, p.16).

In Canada, Natural Resources Canada provides a suite of solar resource maps and software (e.g.: RETScreen and CAN-QUEST) for the calculation of PV potential, as well as other clean energy project analysis tools. In British Columbia, Dr. John Hay conducted the first (and only) comprehensive solar energy resource assessment of the entire province using interpolated data and slope radiation models. His findings facilitated an exhaustive report on the economic, social, and policy drivers of solar uptake prepared for the BC Ministry of Energy, Mines, and Petroleum Resources (Acres Consulting Services Ltd., Solar Applications and Research Ltd., & Hay, 1980).

Nevertheless, most interpolated and modelled datasets are spatially coarse (~10km^2, at best), and though appropriate for citywide or landscape-scale assessments, they are unable to provide meaningful building-scale solar resource assessments on their own, without any consideration given to the impacts of local shading or micro-climate (Nguyen & Pearce, 2010).

Meteorological Indicators

In the absence of ground-based irradiance measurements, meteorological parameters (e.g.: cloud cover, air temperature, rainfall, water vapour, and visibility) can act as a proxy (Paulescu, 2008; Paulescu et al., 2013). Meteorological parameters are used in standalone, or to supplement hybrid, models based on correlations between the parameters and atmospheric extinction during clear and cloudy-sky conditions. They tend to predict monthly averages, though efforts to downscale assessments to daily and hourly time intervals have been made (Moradi, Mueller, & Perez, 2013; Wong & Chow, 2001).

Another set of meteorological parameters used to base solar energy resource assessments is called a *Typical Meteorological Year* (or TMY). These datasets provide, among other meteorological elements, insolation predictions for a typical year based on 30-year averages re-sampled every 10 years (i.e.: climate normals). The first TMY was determined by Marion & Wilcox (1994) and provided monthly and annual averages for the 1961-1990 NSRDB based on 229 stations of data. Today, the TMY3 dataset predicts hourly insolation averages from the 1976-2005 period based on data from 1020 locations. These datasets underpin many commercial software packages designed to simulate the solar resource potential of PV installations over a typical one-year period, such as PV*SOL, PVSyst, and the popular PVWatts package (Sengupta et al., 2015). Though meteorological models and TMY datasets coupled with information on PV panel tilt and orientation can provide an estimate of rooftop insolation, they do not account for sky-view obstructions that dominate attenuation at the local building-scale (Hofierka & Kaňuk, 2009; Jakubiec & Reinhart, 2012).

Satellite-based

Spaceborne radiometric data is sensed from polar-orbiting (e.g.: NASA’s Aqua and Terra) and geostationary (e.g.: Geostationary Operational Environmental Satellite or GOES) satellites for use in empirical, physical, or semi-empirical models that estimate surface irradiance based on space-observed reflectance. Geostationary satellites provide ~1km^2 spatial resolution and near continuous temporal coverage (~ 15 min) as they orbit congruently with Earth, while Polar-orbiting satellites are in a lower pole-oriented orbit which gains them spatial resolution (~250m^2), but cede temporal coverage as they pass over the same site roughly once per day (Zarzalejo, 2008).

Empirical models predict GHI irradiance using regression relationships established between instantaneously sampled satellite and ground-based measurements. Based on location-dependent coefficients of the regression model, empirical methods require ongoing training with surface measurements to be accurate. Heliosat 1 is an example of a pure empirical model and was originally proposed by Cano, Monget, Albuisson, & Guillard (1986). It provides estimations of GHI at a spatial resolution of 1km.

Physical models employ first principles from radiative transfer theories to estimate surface GHI and DNI from satellite observations (broadband or spectral-specific) related to cloudiness. Physical models remain computationally intensive, though rapid processing improvements are helping mitigate this. Compared to other approaches, physical models have the advantage of being able to leverage additional data channels from new satellites / sensors, constantly refining their accuracy as new sources of input data come online (Sengupta et al., 2015).

Semi-empirical models use a hybrid empirical-physical approach, where cloud-cover indices are derived using TOA and space-observed reflectance, which is then used to modify a clear-sky model (Gurtuna & Prevot, 2011; Ineichen & Perez, 2002; Kasten, 1996; Kasten & Young, 1989) according to the cloud scene for an estimate of insolation at the Earth's surface. Heliosat 2 and 3 are examples of semi-empirical models that evolved from the work of Cano et al. (1986) to incorporate physical atmospheric parameters such as the Linke turbidity factor (Ineichen & Perez, 2002; Rigollier, Lefèvre, & Wald, 2004), aerosols (Hammer et al., 2003), and radiative transfer modelling schemes such as SOLIS (Mueller et al., 2004). As satellite sensor technology and computational methods improve, so too does the accuracy of satellite-based models for deriving solar radiation. As a result, “the former distinction between purely empirical or physical models has been diluted towards a more hybrid character. Nowadays most of the currently used models for deriving solar radiation from satellite images contain both empirical and physical information”, facilitated by the availability of higher-resolution radiometric data and computational methods (Zarzalejo, 2008).

Though satellite-based methods are valuable at providing solar data across large tracts of space and time, especially when ground-based are not available, they have significant limitations in terms of being able to predict high-resolution irradiance on urban rooftops:

- Do not account for local or landscape-scale sky-view obstructions;
- Do not provide the spatial resolution needed to adequately assess surface geometries;
- Even in clear skies, satellite-based observations are always impacted by atmospheric attenuation, hindering the fidelity of “ground” reflectance they observe; and
- Require technical information and specialized skillsets for the processing, computation, and analysis required to provide meaningful results.

As Hofierka and Kaňuk (2009) point out, “the assessment of solar energy resource in urban areas at local scales requires a combination of a general/regional solar resource database and analysis of local conditions that modify the actual availability of solar energy” (Hofierka & Kauk, 2009, p.1). It is in the analysis of fine-scale local conditions that satellite-based methods generally find fail to quantify with the precision and accuracy required. However, satellite-based data can be used to support the derivation of a regional solar resource database that is then incorporated in more detailed local-scale analyses.

GIS

GIS technology provides a powerful modelling space for the complex processing and analysis needed to account for the spatiotemporal variations in urban irradiance (Hofierka & Kaňuk, 2009). GIS has been leveraged in a variety of different ways over the years, each with its own level of complexity, data requirements, integration with other models, and resolution capabilities. GIS functions can be coupled with existing models to simply provide the geospatial analysis (latitude, slope, aspect, and shading) of what is otherwise run using numerical (e.g.: MATLAB) or scientific (e.g.: FORTRAN) computing approaches. However, these approaches are computationally complex and take significant resources/time/skill to perform. Instead, Nguyen and Pearce propose, “[s]olar radiation models integrated within GIS have been found to eliminate the complexity of programming GIS functions into mathematical models (p.833).

Standalone GIS-based models began to appear in the mid-1990s (e.g.: SolarFlux and Solei), and typically used simple empirical formulas to compute landscape-scale solar resource assessments (Ŝúri & Hofierka, 2004). Other simplified approaches used readily available cadastral, land use, and demographic data with stratified statistical sampling methods to estimate the distribution of available roof area suitable for large-scale solar energy projects (Izquierdo, Rodrigues, & Fueyo, 2008). Wiginton, Nguyen, and Pearce (2010) use airphotos and feature extraction, specifically the ArcGIS Feature Analyst extension, to batch identify and extrapolate roof area-population relationships for quantifying large-scale rooftop PV potential of a region in south eastern Ontario.

Ŝúri and Hofierka (2004) developed a solar radiation model called *r.sun*, which is fully integrated in the open-source GRASS GIS environment, and is the basis for the web-based PV estimation package known as PVGIS. The model is based on equations set out by the European Solar Radiation Atlas project, and “reflect European climate conditions” (Ŝúri & Hofierka, 2004, p.178). The authors note how the calculation of the beam component (DNI) is straightforward among various models in the literature, but the diffuse component (DHI) is handled quite differently. They emphasize how DHI depends on local climate and regional terrain and how this component is often the largest source of estimation error, highlighting the importance of taking care when calculating the diffuse fraction (Ŝúri & Hofierka, 2004).

Fu and Rich (1999) developed what is still widely regarded as the most popular GIS-integrated solar radiation model – *Solar Analyst* (Gueymard, 2012; Jakubiec & Reinhart, 2012). The tool evolved from the work of Rich, Dubayah, Hetrick, and Saving (1994), which focused on the derivation of an algorithm that was first implemented in software called SolarFlux, and used Esri's Arc Macro Language. The purpose of their algorithm was to better understand landscape patterns of solar radiation for ecological and biological applications (Fu & Rich, 2000, 2003; Paul M Rich & Fu, 2000).

In 1999, the algorithm was re-designed using C++ and ported over to Esri's ArcGIS (then ArcView), implemented as a Spatial Analyst extension called Solar Analyst. This is when the tool began its rise in popularity for use in citywide solar energy assessments. Some consider Solar Analyst a suitable tool for the needs of such fine-scale radiation mapping (Batlles et al., 2008; Brito, Gomes, Santos, & Tenedório, 2012; Hofierka & Suri, 2002), while others critique it (Gueymard, 2012; Jakubiec & Reinhart, 2012; Nguyen & Pearce, 2010). Regardless, the popularity of ArcGIS (and by extension, Solar Analyst) has likely led to its prominence as the go-to tool for mapping the solar potential of cities, and that is difficult to contest (Jakubiec & Reinhart, 2013). Being the most prolific tool for urban solar resource assessments, the Solar Analyst model will be described in greater detail.

Solar Analyst Details

The Solar Analyst tool is a semi-empirical deterministic model (Gueymard, 2012) that is largely driven by the upward-looking hemispherical viewshed algorithm designed by Rich et al. (1994). Viewsheds are computed for every pixel of an input DEM and represent the sky obstruction as "viewed" by each cell. Using standard astronomical equations, the position of the sun relative to each cell is determined based on latitude, elevation, slope/aspect, day of year, and time of day (Fu & Rich, 2000).

The quantity of beam irradiance "originating from each sky direction is represented by creating a *sunmap* in the same hemispherical projection as for the viewshed. The [sunmap] specifies suntracks, the apparent position of the sun as it varies through time. In particular, suntracks are represented by discrete sky sectors, defined by sun position at intervals through the day and season" (Fu & Rich, 1999, p.7). Unlike direct beam, diffuse irradiance can originate from any sky direction. To account for this, the tool employs a *skymap* concept that divides the hemispherical sky into zenith and azimuth divisions called sky sectors. Fu and Rich (1999) note, "[s]ky sectors must be small enough that the centroid zenith and azimuth angles reasonably represent the direction of the sky sector in subsequent calculations" (p.8), and that "[s]kymaps of 18 zenith divisions (5-degree intervals) and 16 azimuth divisions (22.5-degree intervals) are commonly employed for detailed studies" (p.28).

The model allows for different input parameters of time intervals, viewshed calculation directions, sunmap divisions, and sky sectors; however, with gains in accuracy come tradeoffs in calculation speed. Fu and Rich (1999) perform a sensitivity analysis using different input parameters and suggest viewshed calculation and sky resolution are the most computationally intensive; furthermore, that 32 directions and a 200 x 200 sky size, respectively, are more than sufficient for most purposes.

According to input parameters, the model pre-processes viewsheds, sunmaps, and skymaps for each pixel in the DEM and overlays them to provide a masked viewshed representing obstructions from surrounding cells. Thus, Solar Analyst's ability to account for occlusion rests largely upon the precision and accuracy of the input DEM, just as its skill at estimating the type and intensity of irradiance originating from each sky sector is a function of an appropriate sky resolution, as well as the atmospheric parameters by which it models attenuation. Solar Analyst uses two atmospheric parameters to represent attenuation: atmospheric clearness and diffuse fraction. These parameters are fixed for each model run, so it is crucial they accurately represent the local atmospheric characteristics of the time interval.

Direct and diffuse components are calculated using geographical information, as well as sky access, sky divisions/sectors, and attenuation parameters. Direct insolation is calculated for each sunmap sector and the receiving slope/aspect of each cell, as derived from the DEM. The direct component is calculated for each cell of the DEM using a simple transmission model that accounts for the solar constant, atmospheric transmissivity, and AM corrected for elevation.

Direct insolation is calculated for each unobstructed sunmap sector in accordance with the solar vector and the receiving slope/aspect of each cell, as derived from the DEM. A simple transmission model is used to quantify the direct component for each cell in the DEM using the solar constant, atmospheric transmissivity, and AM corrected for elevation (Equation 7). The final direct beam insolation layer is the integrated set of all individually calculated direct normal insolation values across a given time interval.

Equation 7 – Direct normal insolation

$$DNI_{\theta,\alpha} = SC * {k_t}^{AM(\theta)} * SunDur_{\theta,\alpha} * SunGap_{\theta,\alpha} * cos(SunInc_{\theta,\alpha})$$

> Where DNI is the direct normal insolation, as from a sunmap sector with a centroid at zenith angle θ and azimuth angle α; SC is the solar constant; k_t is the atmospheric transmissivity; AM is the relative optical path length (or air mass corrected for elevation); $SunDur$ is the time duration of the sky sector; $SunGap$ is the gap fraction (proportion of visible sky) for the sunmap sector; and $SunInc$ is the angle of incidence between the centroid of the sky sector and axis normal to the surface.

Diffuse insolation is calculated in much the same way as direct, but typically employs a *uniform overcast sky* model that considers incoming diffuse to be isotropic (i.e.: the same from all sky directions), so the sum of all unobstructed sky sectors equals the total incoming diffuse component (Equation 8). An anisotropic (or *standard overcast*) model is also available, though less readily implemented or suitable.

Equation 8 – Diffuse insolation

$$Dif_{\theta,\alpha} = GNI * k_d * Dur * SkyGap_{\theta,\alpha} * Cos(SunInc_{\theta,\alpha})$$

> Where Dif is the diffuse normal insolation, as from a sky sector with a centroid at zenith angle θ and azimuth angle α and considered a uniform sky; GNI is the global normal insolation, k_d is the diffuse fraction; Dur is the duration of the time interval; $SkyGap$ is the gap fraction (proportion of visible sky) for the skymap sector; and $SunInc$ is the angle of incidence between the centroid of the sky sector and the intercepting reference surface.

Solar Analyst was designed to be a fast and effective model for the accurate calculation of topographic and atmospheric influences on insolation received at the local and landscape-scales. Fu and Rich advocate that the tool "promises to be useful in engineering and design fields, for such applications such as site assessment, building design, solar collector design, and topographic radiometric correction for remote sensing" (Fu & Rich, 1999, p.31). Indeed, this ArcGIS extension has long since lived up to these promises. The tool continues to drive innovative ways of modelling solar irradiance, especially in urban environments (Batlles et al., 2008; Brito et al., 2012; Chow, Fung, & Li, 2014; Tooke, 2009; Yu, Liu, Wu, & Lin, 2009), limited mainly by the accuracy and precision of input data and processing power and aptitude.

Characterizing Solar Models

Given the various methods for modelling solar irradiance at the Earth's surface, and the equally diverse range of applications, it is helpful to be able to describe model characteristics. Generally, approaches can be described in terms of the type(s) of method(s) used in a methodology and details of the desired results and required data inputs. This is a prudent step in identifying methodological pathways of ensuring outputs meet end-user needs.

Model Typology

According to Gueymard & Myers (2008), there is no accepted typology of solar radiation models. Following their exhaustive review of over 40 years of the literature, they do, however, propose the following set of criterion for categorizing them:

1. *Type of output data*

   Ideally, solar radiation models output direct, diffuse, and global irradiance separately; though many other models do exist to derive direct or diffuse from global irradiance.

2. *Type of input data*

   Models may require meteorological, climatological, and/or irradiance variables as inputs. These can be derived from surface, air, or space-borne sensors, or the output from a lower-order radiation model (e.g., using global to derive diffuse radiation).

3. *Spatial resolution*

   Models output either point predictions or gridded products covering an areal extent; the latter being the spatial coverage typically associated with remotely-sensed inputs.

4. *Time resolution*

   A model's time (or temporal) resolution depends on its application. Solar energy generation requires higher resolution data, while lower resolution data are typically pressed into climatological service, or more specifically:

   - Minutely (or less) is *high* resolution; needed for solar concentrators.
   - Hourly is *standard* resolution; used in solar system or building energy simulations.
   - Daily is *average* resolution; also used in solar system or building energy simulations.
   - Average hourly/daily over a long-term period, such as 10-30 years, is considered a *climatological* resolution; used for constructing solar climatologies informing solar system design.

5. *Spectral resolution*

Most models tend to evaluate the solar spectrum as a single band from about 300 – 4000 nm; however, the spectral resolution desired from a model depends on the application. For example, specific applications in atmospheric, remote sensing, building, and agricultural sciences may only be interested in the distinct ultraviolet (below 400 nm), photosynthetic (~ 400 – 700 nm), or infrared (~700nm – 1mm) wavebands.

6. *Type of methodology*

Models can be either deterministic or stochastic (statistical). A deterministic algorithm predicts irradiance at a specific time; whereas, a stochastic model predicts irradiance, according to a set of statistical assumptions such as variance or cumulative frequency distribution, for a time series. Some models combine both deterministic and stochastic features.

7. *Type of algorithm*

Models can be either physical or semi-physical (based on physical principles), or empirical models (derived from measured irradiance for prediction elsewhere).

8. *Surface geometry*

Models are used to predict irradiance incident on a horizontal, tilted, or tracking surface. Most solar energy generation, building, or ecological science applications require tilted or tracking surface irradiance data.

9. *Type of sky*

Models tend to consider the effects of clouds, but some do not; depending on the application – such as building or solar concentrator design – irradiance predictions may only be required for clear-sky conditions.

Though the number of possible combinations resulting from the above set of criterion can be considerable, not all are always necessary, possible, or practical. Desired end-results are seldom directly available from the often-limited set of input data. Instead, they are typically achieved by running successive models that generate output, passed as input, to another model, and so on (Gueymard & Myers, 2008b).

A drawback to a methodology that ‘stacks’ models this way is the risk of exposing end-results to the possibility of compounding uncertainty and error between successive model iterations. Therefore, great care must be taken when employing such a methodology, and being prudent in this regard means striving for compatibility and consistency between integrated model resolutions (temporal, spatial, and radiometric), scales, and intended uses. Nonetheless, no matter how impeccably constructed a methodological approach may be, Gueymard & Myers (2008) warn that the predicted irradiance will always be imperfect. Even if it were perfect, they caution it would “be impossible to ascertain because the ‘true’ solar irradiance cannot be determined theoretically or measured experimentally with perfect certainty” (p.481). Gueymard and Myers (2008) also note how “many models are developed empirically from data measured at one or a few specific sites, and their ‘universality’ must be verified by testing them against data from a variety of other sites”. Rarely does this occur, and when it does “these studies take time, so that it is usually difficult to recommend a new or recent model for widespread application” (p.482).

Chapter 2: Methodology, Methods, and Data

Methodology

Using the criterion proposed by Gueymard and Myers (2008) as a framework, a novel methodology for modelling high-quality, high-resolution insolation across rooftops throughout a city is presented. In general, a solar climatology is created to render atmospheric parameters that are used in conjunction with a precision surface, to model insolation using GIS. Focus and care are given to the derivation of model input parameters required for such high-resolution assessments; specifically, their representativeness of local topography and climatic conditions, compatibility in terms of integrated scales and resolutions, as well as universality—in particular, that of diffuse fraction. The methodology also includes computational approaches that aid in the querying of data and execution of integrated models. To provide an overview of the methodology, a brief description of the general methods and data follow.

Overview

A flowchart of the methodology allows for a visual depiction of the stages, data, computation, and models integrated within the approach (Figure 6). At its core, the methodology is structured around using ESRI’s Solar Analyst tool as the modelling space for the generation of annual daily insolation maps for Victoria. These maps are to be of broadband global, direct, and diffuse insolation, representative of the solar energy incident (i.e.: normal or plane-of-array) to each cell, and 1m^2 spatial resolution. Ideally, this require that input data be sourced at scales and resolutions of at least the granularity desired from end-results (i.e.: not downscaled). There are two general categories of data inputs that are required: surface and atmospheric.

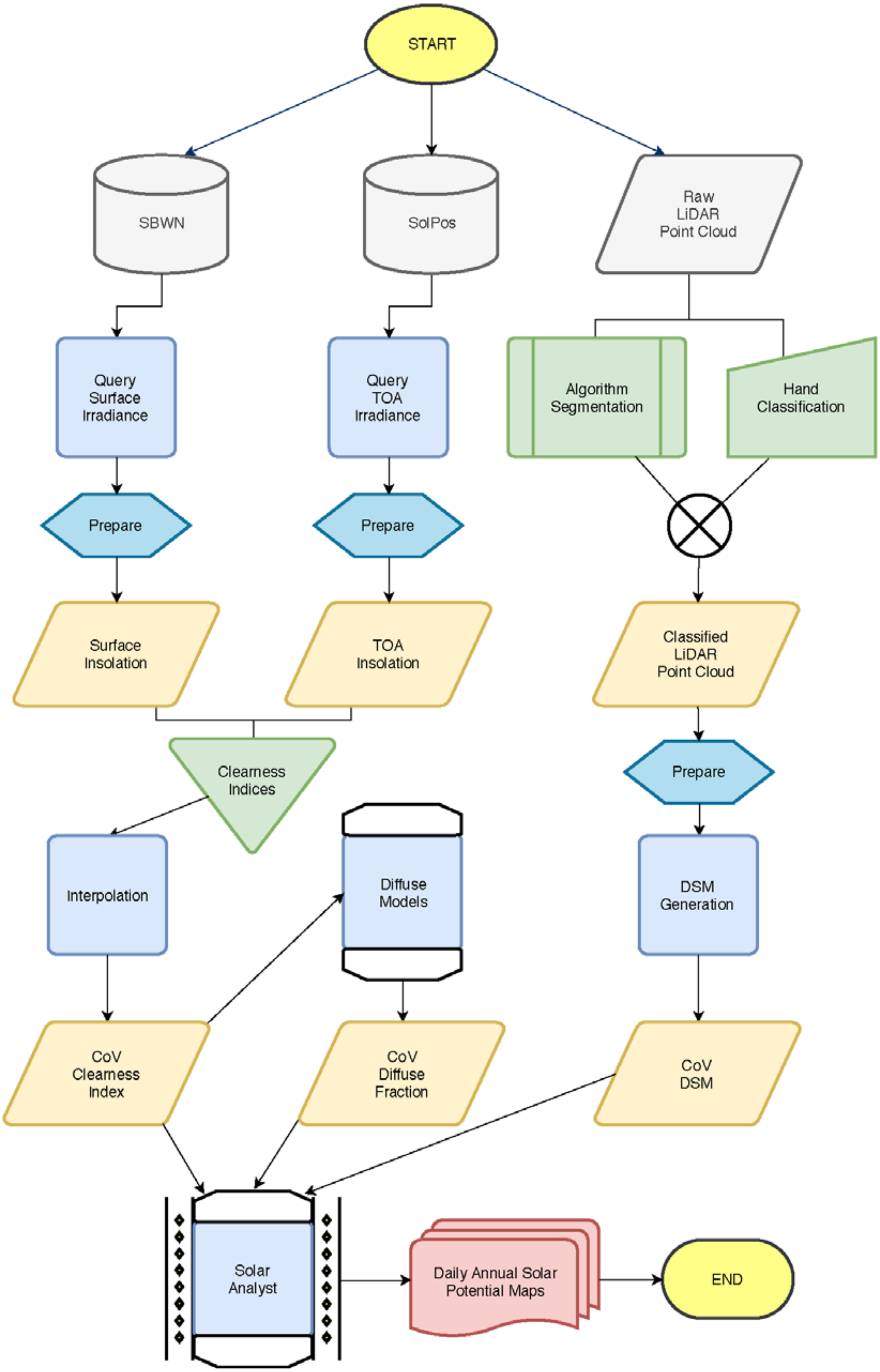
START
SBWN
SolPos
Raw
LiDAR
Point Cloud
Query
Surface
Irradiance
Query
TOA
Irradiance
Algorithm
Segmentation
Hand
Classification
Prepare
Prepare
Surface
Insolation
TOA
Insolation
Classified
LiDAR
Point Cloud
Clearness
Indices
Prepare
Interpolation
Diffuse
Models
DSM
Generation
CoV
Clearness
Index
CoV
Diffuse
Fraction
CoV
DSM
Solar
Analyst
Daily Annual Solar
Potential Maps
END

Figure 6 - Methodology flowchart depicting the integrated models and data parameters

Surface

Characterizing the input surface was approached using methods for generating a DSM from classified airborne LiDAR data. A raw LiDAR point cloud was classified using a combination of algorithm segmentation and hand classification methods. Classified LiDAR was then used to generate a high-resolution ($1m^2$) DSM representing the entire urban canopy of Victoria.

Atmospheric

As discussed, Solar Analyst requires input parameters of atmospheric clearness and diffuse fraction, and it is important these be as representative of the entire spatial extent and time horizon of the model run as possible, as they are fixed values. Thus, a regional solar climatology (or modelled data set) was constructed using ground-based measurements of minutely irradiance, made possible by drawing from a dense network of meteorological stations known as the School Based Weather Network (SBWN). Measurements were averaged to provide daily GHI values for each station and used to construct a ~10 year climatology.

To derive atmospheric clearness (Kt), a corresponding dataset of top-of-atmosphere irradiance was generated using a deterministic algorithm called Solar Position (SolPos), developed by the U.S. National Renewable Energy Laboratory (NREL, 2017). These two datasets were then combined to calculate (Equation 6) an annual set of daily clearness (Kt) indices. To provide just one value for each day of the year representing Victoria, an interpolation method was employed. From the set of single atmospheric clearness indices representing Victoria, a decomposition model was employed to calculate the corresponding daily diffuse fraction as measured diffuse was not available. As discussed, the diffuse fraction is cited as a large source of error for solar energy modelling and is highly dependent on local climate. Thus, to ensure the universality of the decomposition model used, as well as to assess the model for any extreme value or seasonal biases, a comparative analysis with “standard models” was completed.

Methods and Data

Empirical Measurements

Three sets of irradiance measurements were taken between April 3 2014 (day 93) and February 22 2015 (day 53) at two locations in the city, resulting in a total of 325 days of insolation data. These measurements were taken with pyranometers to compare with modelled values. Two pyranometers were installed on two levels of a residential rooftop referred to as Study Site #1, and one pyranometer was installed on the rooftop of City Hall in downtown Victoria. All pyranometers were calibrated to radiometric ISO standards at Campbell Scientific Canada (in Edmonton, Alberta) prior to deployment. They were programmed to provide minutely measurements, and recorded data using Campbell Scientific Canada CR10X dataloggers.

Study Site #1 (Figure 7)

Two Kipp and Zonen SP Lite2 sensors were installed on two different levels of a residential rooftop in the Oaklands neighbourhood, and oriented in a plane-of-array inclination of ~ 23° and aspect of ~ 218° SW:

- “Upper” - located on the second story roof located at ~ 123.3393° W and 48.4417° N Decimal Degrees, and;
- “Lower” - located on the first story roof located at ~ 123.3392°W and 48.4416° N Decimal Degrees (Figure 8).

These sensors have a spectral range of 400 to 1100 nm, which covers the spectrum of interest to solar energy technologies. They use silicon photodiodes with a diffuser as a sensor. There are 3 large coniferous trees just south of the residence, which shade the Lower sensor in the morning hours of while they do not impact the Upper sensor. This provided for desired differences in the direct and diffuse regimes between the two, as well as for measurements that could be used to compare against the model's skill in predicting occlusions.

Figure 7 – Study site #1: Upper sensor indicated by red dot; Lower sensor indicated by yellow, and; large coniferous trees indicated by green arrow

Figure 8 – Lower sensor location indicated by yellow arrow. Sensor sat on top of roof vent.

Study Site #2

One Kipp and Zonen CMP 11 was installed on a pedestal built atop Victoria's City Hall in downtown Victoria, and mounted in a levelled, horizontal orientation (Figure 9).

- "City Hall" – located on the roof of the roughly 4th floor at ~ 123.364889° W and 48.428202° N Decimal Degrees.

The sensor is what is considered "research grade", as it has a spectral range of 285 to 2800 nm, which covers more of the solar spectrum than can be made use of by solar energy technologies, but is integral spectral information for research regarding irradiance. It is a thermopile sensor, with double glass domes to ensure atmospheric moisture does not confound measurements. The panoramic view from atop city hall is relatively clear (Figure 10), with a clock tower that extends above the viewshed surface to the ENE, and some buildings that increase horizon obstructions by a few (~5 - 10) degrees and a smoke exhaust system WSW on the rooftop that intermittently emits boiler steam during winter.

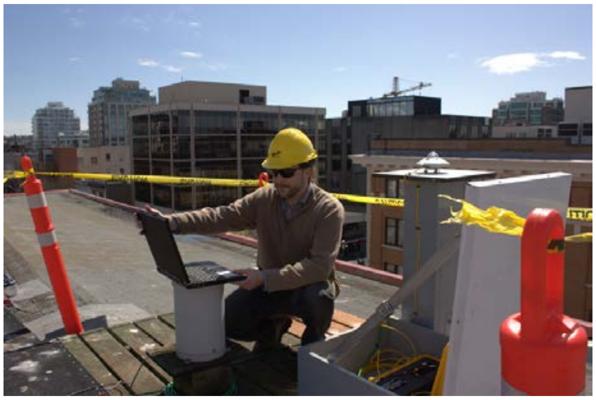

Figure 9 - Pedestal, pyranometer, and datalogger being programmed on city hall's rooftop.

Figure 10 – Panoramic (360°) view atop city hall, with the pyranometer in view on the right.

Surface

Lidar

Airborne LiDAR was flown April 26, 2013 with an ALS 70 sensor. Flight lines were flown at an average height of ~1300m AGL (m), with a flight speed of ~220 knots, resulting in a feature point density of ~10.1 points/m^2 and ground point density of ~1.5/m^2. A total of 206,445,656 points were collected, ranging between 127.48mASL and -3.23mASL. These points were outputted in NAD83CSRS, and the vertical datum was CGVD28, based on the HTv2.0 hybrid geoid model. There was a data gap in coverage (CRD_475000E_5366000N_NBE), which resulted in part of a local mall (Hillside) missing.

Classification

Classification of the raw point cloud was completed using a combination of automated and human-interpreted methods, working in concert with the University of Victoria Hyperspectral Lidar Research Group. As per the lead researcher of this group, Dr. Olaf Niemann, in-house classification methods used are similar to those employed by TerraScan, and he points the reader to L. Wang & Zhang (2016) for details. More specifics are not within scope of this study or available, being in-house (proprietary). Instead, a reader interested in reviewing the latest research challenges and segmentation methods for extracting building rooftops from airborne LiDAR are referred to Gilani, Awrangjeb, and Lu (2018).

Regardless, the majority of classification and quality checking was accomplished by human analysis (~40 person weeks), using Microstation and TerraSolid software, as well as 10cm orthophotos (2013) for reference. In all, 37 .las v1.2 files (raw point cloud format) were classified using the predefined classification codes of the American Society for Photogrammetry and Remote Sensing (ASPRS) (Table 2).

Table 2 – Categories for classified LiDAR points, based on ASPRS codes

Class	*# Points*	*Description*
1	1,114,985	Miscellaneous
2	28,820,090	Ground
3	74,973,261	Low vegetation
5	54,301,963	High vegetation
6	46,806,282	Building
9	7,010	Water
13	422,065	Power Lines/Poles

Class 1 refers to any transient objects (e.g.: cars, buses, etc.), outliers, and non-building stationary objects (e.g.: billboards, stop signs, trampolines, etc.). Class 3 encompasses all low vegetation and objects between ground and 2m above ground. Power lines and power poles were classed within class 13 when possible, and Class 1 where these structures were more challenging to define. Class 6 refers to buildings, defined as structures with four walls and accessible by a standing person. Building identification was enhanced through using a polygon file defining building footprints.

Distinguishing points for classification can be more challenging in certain areas of the urban canopy than others (Gilani et al., 2018). Typically, ground filtering of the point cloud is relatively straightforward, as the last returns of multi-return pulses almost exclusively represent ground (Hung et al., 2018). However, classifying points in the remainder of the urban scene is much more complex, especially at the interface of the natural and built environments (Jochem, Höfle, Rutzinger, & Pfeifer, 2009; L. Wang & Zhang, 2016). Considerable areas of Victoria are covered by dense urban forests (City of Victoria, 2013). This presented unique challenges in terms of classifying rooflines where vegetation overhangs, and powerlines/powerpoles that pass near vegetation. Challenges not related to vegetation included macros classifying some chimneys as ‘miscellaneous’. Though this is expected (deviation from roof plane), it is undesirable as chimneys can certainly introduce shading to a rooftop, thus need to be accounted for as part of the ‘building’ class. Another challenge observed was when LiDAR returns penetrated rooftop fenestration or venting. This produced usually one lone return, relatively much lower in elevation than adjacent points higher up on the actual roof plane. These cases were more difficult to identify than chimneys classed as ‘miscellaneous’. Extra vigilance when quality-checking rooftops was required to ensure the fidelity of roof plane characterization. Continually cross-referencing a point cloud scene with corresponding orthophotos was a helpful approach to identifying skylights and vent features warranting further scrutiny. Though time-consuming, hand-classification proved to be a vital method for administering the oversight needed to ensure LiDAR were classified as accurately as possible. That being said, no matter how rigorous quality checks were, errors are inevitable given the volume of points involved in a citywide dataset.

To illustrate the effects to the solar model from erroneously classed points, consider the nature of a DSM. Being contiguous, a DSM is essentially a surface draped over the points used to generate it. In a solar model, this surface is opaque. If an errant or miscellaneous point (e.g.: bird, “air hit”, etc.) ends up in the set used to generate a DSM, then the 2.5D model could misrepresent 3D reality by erroneously spiking upwards to the elevation of the errant point, introducing shading to surfaces around it in the solar model. Similarly, any points that penetrated skylights or venting (and escaped quality-checks) would result in a sharp depression in the roof plane when one does not actually exist. Thus, errant or mis-classed points must be excluded to every extent they can be; however, as this cannot be guaranteed, methods to account for them when generating the DSM are equally as important.

DSM

To generate the DSM, an ArcGIS tool called “LAS Dataset to Raster” was used. Parameters used in this tool include: input data, output data type, value field used (elevation), interpolation type (binning), output raster data type (float), and sampling size (cellsize – 1m^2 spatial resolution). This tool requires a .lasd format as input, which was created in ArcGIS as a mosaic of all .las blocks of LiDAR using the points classified as ‘high vegetation’, ‘building’, and ‘ground’. Using only these classes allowed for the exclusion of all other points that might otherwise introduce shading to the scene when ‘draped’ as part of the DSM, such as powerlines, air hits, birds, and any other miscellaneous returns.

Typically, methods of interpolating LiDAR points to a DSM involve assigning the maximum point value in each cell as the defining elevation. However, the complexities of the urban canopy, especially at the interface of natural and built environments, challenge convention in this regard. For example, maximum values could lead to misrepresentation of roof edges where overhanging vegetation occurs, as well as amplify effects from any errant or misclassified points that escaped quality checks. Thus, experimentation with various interpolation, data type, and sampling size methods was conducted to identify a set of parameters that best represent the geometry and insolation regime received at a research site. Combinations of the following cell assignment, void fill, and spatial resolutions were used to produce corresponding DSMs of the research site:

- Triangular Irregular Network (TIN) using natural neighbours at 0.25m^2
- Maximum value and filling using linear at 0.25m^2
- Inverse distance weighted and filling using natural neighbour at 0.25 m^2

- Inverse distance weighted and filling using natural neighbour at 0.50 m^2
- Inverse distance weighted and filling using natural neighbour at 1.00 m^2

These DSMs were used as input in the Solar Analyst tool and ran to generate annual insolation using identical model parameters (Figure 11). Assessment was completed visually, comparing: roof edges, chimneys, skylights, and the general consistency across roof planes, hips, and ridges, as well as trees. Binning performed better at capturing roof edges than using TIN, as the triangulation created false points between roof edge and ground that extend beyond the footprint of buildings. Using sampling sizes less than $1m^2$ led to more precise representation in DSMs, but much more sporadic (noisy) insolation results across roof planes and vegetation, as well as significantly increased rendering times (~3.5x). Overall, results supported the use of the inverse distance weighted method, with natural neighbour void fill, using floating integers, and a sampling size of $1m^2$. This set of parameters was then used in the generation of a DSM as representative of the urban canopy of the entire city of Victoria as possible.

Tri. Nat. 0.25m Orthophoto Max. Lin. 0.25m

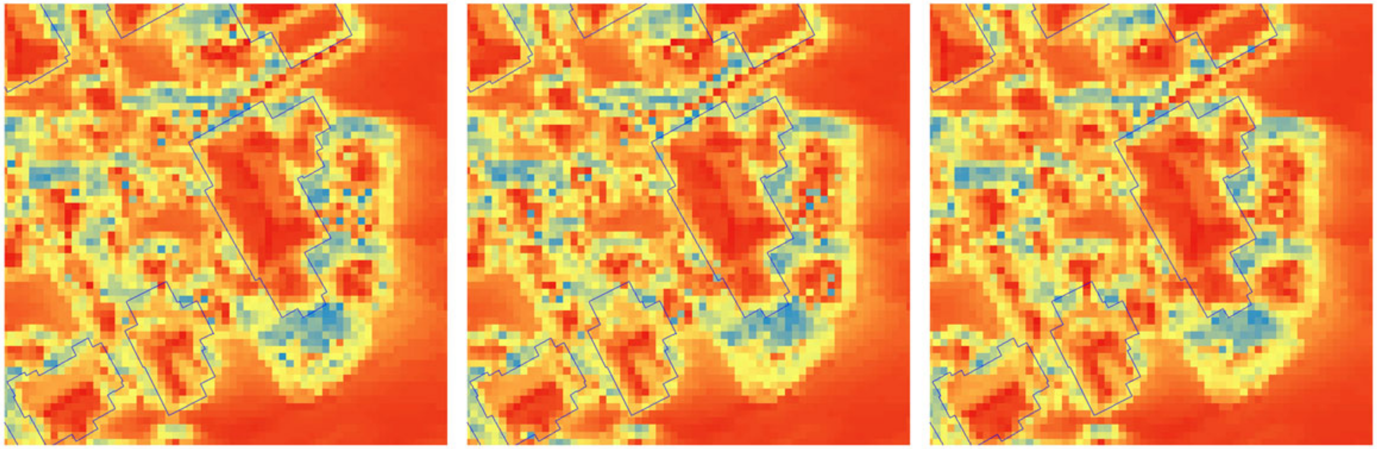

IDW Nat. 0.25m IDW Nat. 0.50m IDW Nat. 1.00m

Figure 11 – Insolation results (scale: red = most intense; blue = least intense) of DSM methods of generation: top-left – triangulation and natural neighbour at 0.25m^2; top-middle – Orthophoto of research site; top-right – Maximum value and linear at 0.25m^2; bottom-left – Inverse Distance Weighted (IDW) at 0.25m^2; bottom-middle – Inverse Distance Weighted (IDW) at 0.50m^2; bottom-right – Inverse Distance Weighted (IDW) at 1.00m^2

Atmosphere

Empirical Ground-based Irradiance

A data-driven approach to inferring atmospheric parameters was employed, as a spatially-dense network of longterm ground-based irradiance measurements was available for constructing a regional solar climatology. The School-Based Weather Network (SBWN) is a UVic initiative founded by Dr. Andrew Weaver and Ed Wiebe in 2002. Its primary purpose is to promote and facilitate meteorological and climate sciences in grade-schools by the installing weather stations on top of school facilities (Weaver & Wiebe, 2006). Though initiated and maintained for educational purposes, this network provides dense spatiotemporal coverage across Southern Vancouver Island with ~160 stations collecting various meteorological data every minute. The stations are also installed with some degree of consideration for standardizing measurements (south-facing access, clear of most occluding obstacles, chimneys, vents, etc.), though in some cases placement is not ideal, tradeoffs in accuracy are made for spatial gains. The network uses Davis Vantage Pro 2 stations, complete with silicon photodiode pyranometers that detect GHI between 300 to 1100 nanometers (Davis Intruments, 2013). This spectral coverage provides a reasonable match to the solar spectrum of interest to solar energy technologies (Sengupta et al., 2015).

The network’s database (MySQL) was extensively queried to provide daily irradiance datasets, along with respective station metadata. Scripting methods leveraged server-side processing for most dataset construction. Bash scripting set environment and SQL variables up to be executed as part of the MySQL queries (Appendix A). The schema of the database was such that data are stored in multiple monthly tables for each respective year, which necessitated an approach using nested averaging queries to render the data into monthly hourly averages (Appendix B). Thus, 12 runs the script were required to produce monthly hourly averages based on the 10 years (2005 – 2015) of data. Finally, all monthly hourly data were appended and then upscaled to daily averages using Python.

Stations within Victoria's regional catchment – the Capital Regional District – were included if they improved spatiotemporal representation and contained at least 4 years of continuous, reasonable data. Reasonability of data was determined qualitatively through discussions with the network manager (sensor/station issues: placement, maintenance, vandalism, etc.), as well as quantitatively (station uptime >95%, values within 0 – 1367 W/m^2, and no significant deviations in trends compared to others in its proximity). Some stations briefly presented irradiance near, or in slight excess (~1 – 100 w/m^2) of, the solar constant. This is likely to occur on moderately cloudy days as a consequence of the refractive enhancement, or edge effects, of passing clouds.

In total, 106 stations were used to provide the spatiotemporal coverage for a 10-year *solar climatology* of the CRD spanning 2005 – 2015, with an ~8-year station average and 99.98% uptime. Of these 106, 18 stations fell within the city of Victoria boundaries.

Top-Of-Atmosphere Irradiance

Extraterrestrial global horizontal irradiance data (TOA) were produced using the National Renewable Energy Laboratory's SOLPOS calculator (NREL, 2017). This calculator is considered to be the most accurate (publicly available) means of determining TOA, and calculates the apparent solar position and intensity at the top-of-atmosphere based on the corresponding date, time, and location on Earth. Stations within the extent of the solar climatology were considered to receive the same TOA as each other, as the subtended angular differences between each station and a shared point at the TOA are negligible. Daily data were generated to match the same span (2005 – 2015) as the surface insolation dataset to control for any astronomical differences, and then averaged to produce an annual daily dataset of extraterrestrial global horizontal insolation (G_0).

Atmospheric Clearness

Annual daily atmospheric clearness indices (K_t) were generated for each station using the surface GHI (G_h) and TOA (G_0) values, and the K_t = (G_h / G_0) ratio (Equation 6).

Interpolation

As the Solar Analyst tool requires only one atmospheric clearness and diffuse fraction parameter for each run of the model, interpolation of the solar climatology was conducted to render a single set of annual daily atmospheric clearness indices for Victoria.

The preferred method for interpolating insolation data is kriging (H.G. Beyer, Czeplak, Terzenbach, & Wald, 1997; Hay, 1986; Journée & Bertrand, 2011; Şen & Şahin, 2001; Zelenka et al., 1992). Kriging interpolates points at unsampled locations by using knowledge of the underlying spatial autocorrelation, or *spatial dependence*, within a dataset. This knowledge is provided by semivariogram analysis to determine an optimal set of weights to estimate the surface of unsampled locations. As such, the accuracy of this interpolation method depends largely on building a valid kriging model, which itself depends on the "trueness" of the one single semivariogram that is assumed to be representative of the region being interpolated. In other words, regular kriging methods do not take into account uncertainty in the semivariogram estimation that the model depends on. Furthermore, for this study a valid kriging model for each of the 365 days would be needed, posing logistical challenges. Instead, this research employed the Empirical Bayesian Kriging (EBK) interpolation method in ArcGIS, as it:

- Automates the challenging aspects of building a valid kriging model.
- Accounts for error introduced in the underlying semivariogram by deriving multiple subsets of semivariograms.
- Leads to more accurate results than other kriging methods.
- Is available as a geoprocessing tool, enabling batch scripting.

Parameters used in a geoprocessing script include: cell_size (250), transformation_type (Empirical), max_local_points (100), overlap_factor (1), number_of_semivariograms (100), search_neighborhood (standard circular, with RADIUS=78773 ANGLE=0 NBR_MAX=15 NBR_MIN=10 SECTOR_TYPE=ONE_SECTOR), output_type (prediction), threshold_type (exceed), and semivariogram_model_type (K_Bessel).

These parameters were chosen to produce the most accurate results as possible, though did come with computational costs. Specifically, “K-Bessel” semivariogram approach was used; the main advantage being the most flexible and accurate of the options, but it does take longer to calculate depending on the number of semivariograms needed (ArcGIS, 2019). The outcome was a time-enabled mosaic produced using a highly sophisticated interpolation method that was applied through an automated scripting process (Appendix C).

This allowed for the set of annual daily clearness values to be rendered for Victoria (lat 48.4284° N, lon 123.3656° W) for every day of a typical year based on the solar climatology, ensuring as much representativeness of the clearness indices as possible.

Diffuse Fraction

A global-to-diffuse decomposition model was used to compute diffuse fraction from the annual daily clearness indices, as empirical measurements were not available. A comparative analysis of different diffuse fraction models is conducted as part of this research, and the long-standing Orgill and Hollands (1977) model was used on the basis it:

- The only known model based on Canadian data (Toronto, ON)
- Was employed in similar research nearby – across the Salish Sea in North Vancouver – with good results (Tooke et al., 2012)
- Has been thoroughly reviewed over the years in many studies (Chandrasekaran & Kumar, 1994; Czekalski et al., 2012; Erbs, Klein, & Duffie, 1982; Hawlader, 1984; Hollands & Huget, 1983).
- The authors conclude it “will accurately represent radiation insolation between the latitudes of 43°N and 54°N” (Orgill & Hollands, 1977); and Victoria is located at ~48.5°N.

Granted the above, the representativeness of the Orgill and Hollands model still remains unclear until assessed for its universality for Victoria, and for any potential seasonal[3] or extreme prediction biases. Thus, a comparative analysis similar to that presented in Jacovides et al. (2006) was completed. Though some of the standard models are based on the correlation of global-diffuse hourly values, using them to produce daily averages is appropriate and inherently avoids their main sources of error related to the predictions at hours of low solar altitude.

Diffuse fraction K_d results were rendered for every day of the year, for all 10 standard models, using Python (v3.6) execution (Appendix D) and model scripts (Appendix E). Additionally, using the arithmetic daily mean of all standard models, another dataset was created called the "*standard mean*". The standard mean dataset was derived as a method of benchmarking model results against and to comment on biases.

The Standard Models

Equation 9 – Orgill and Hollands (1977)

$$\mathrm{k_d} = 1.557 - 1.84\mathrm{k_t} \qquad \{\text{for } 0.35 \leq \mathrm{k_t} \leq 0.75\};$$

$$\mathrm{k_d} = 1.0 - 0.249\mathrm{k_t} \qquad \{\text{for } \mathrm{k_t} < 0.35\}; \text{ and}$$

$$\mathrm{k_d} = 0.177 \qquad \{\text{for } \mathrm{k_t} > 0.75\}.$$

As this research employed the Orgill and Hollands model as the method for deriving diffuse fraction, closer attention is paid to and how it relates to the others, the standard mean, and any biases.

---

[3] Defined by "meteorological seasons", where Spring includes March, April, and May; Summer includes June, July, and August; Fall includes September, October, and November; and Winter includes December, January, and February

Equation 10 – Reindl et al. (1990)

$$k_d = 1.45 - 1.67k_t \qquad \{\text{for } 0.3 < k_t < 0.78\};$$
$$k_d = 1.02 - 0.248k_t \qquad \{\text{for } k_t \leq 0.3\}; \text{ and}$$
$$k_d = 0.147 \qquad \{\text{for } k_t \geq 0.78\}.$$

As discussed above, Reindl et al. investigated improvements to the Liu- and Jordan-type model by using more predictors, such as geometric and climatic terms, other than just k_t. Their models are based on data from 3 European and 2 US cities with latitudes spanning 28°4N – 55.7°N. They compare their models to Erbs et al., and by extension Orgill and Hollands, noting many similarities between the two (Reindl, Beckman, & Duffle, 1990).

Equation 11 – Boland et al. (2001)

$$k_d = \frac{1}{1 + e^{7.997(k_t - 0.586)}}$$

Boland et al. (2001) explored using other predictors (similar to Reindl et al.) to reduce error in Liu- and Jordan- type models. They concluded information regarding solar altitude is a valuable second predictor, especially if interested in predicting hourly or 15-min intervals of diffuse fraction (Boland et al., 2001). This model uses data from Geelong, Victoria, Australia (38.1°S). It is the only standard model using an exponential, not polynomial, expression in its correlation approach.

Equation 12 – Hawlader (1984)

$$k_d = 1.135 - 0.9422k_t - 0.3878k_t^2 \qquad \{\text{for } 0.225 < k_t < 0.775\};$$
$$k_d = 0.915 \qquad \{\text{for } k_t \leq 0.225\}; \text{ and}$$
$$k_d = 0.215 \qquad \{\text{for } k_t \geq 0.775\}.$$

Hawlader (1984) developed hourly (above), daily, and monthly diffuse-to-global correlations for data collected in Singapore. As this study applied the models (verbatim) put forth in Jacovides et al. (2006), the Hawlader model was unfortunately mistyped, and is supposed to be " $k_d = 1.1389 - 0.9422k_t - 0.3878k_t^2$ {for $0.225 \leq k_t \leq 0.775$}" with the next range being "{for $k_t < 0.225$}". It is unknown if Jacovides et al. employed this error in their analysis, or just mistyped the article.

Equation 13 – Miguel et al.

$$k_d = 0.724 + 2.738k_t - 8.32k_t^2 + 4.967k_t^3 \quad \{\text{for } 0.21 < k_t \leq 0.76\};$$
$$k_d = 0.995 - 0.081k_t \quad \{\text{for } k_t \leq 0.21\}; \text{ and}$$
$$k_d = 0.18 \quad \{\text{for } k_t > 0.76\}.$$

The work of Miguel, Bilbao, Aguiar, Kambezidis, & Negro (2001) focused on data compiled for the North Mediterranean Belt area. This mosaic included data from multiple countries (Greece, Portugal, France, and Spain) between the latitudes of 37.02°N and 44.08°N, ranging from 1-13 year datasets spanning 1978 - 1996. They derived correlations in three groups: daily k_d from daily k_t; hourly k_d from hourly k_t; and hourly k_d from daily sums of k_d. The above model is the hourly diffuse from global correlation.

Equation 14 – Karatasou et el.

$$k_d = 0.9995 - 0.05k_t - 2.4156k_t^2 + 1.4926k_t^3 \quad \{\text{for } 0 < k_t \leq 0.78\}; \text{ and}$$
$$k_d = 0.20 \quad \{\text{for } k_t > 0.78\}.$$

Karatasou, Santamouri, & Geros (2003) derived daily and hourly correlations for predicting k_d based on 3 years of data from Athens, Greece. They present the above third-order polynomial for hourly prediction and conclude that "the correlation is season dependent, for values of $k_t > 0.3$" (Karatasou et al., 2003).

Equation 15 – Erbs et al. (1982)

$$k_d = 0.9511 - 0.1604k_t + 4.388k_t^2 - 16.638k_t^3 + 12.336k_t^4 \quad \{\text{for } 0.22 < k_t \leq 0.80\};$$
$$k_d = 1.0 - 0.09k_t \quad \{\text{for } k_t \leq 0.22\}; \text{ and}$$
$$k_d = 0.165 \quad \{\text{for } k_t > 0.80\}.$$

Erbs, Klein, & Duffie (1982) derived monthly, daily, and hourly (above) correlations for predicting k_d based on data from 4 cities in the US between the latitudes of 31.08°N and 42.42°N, ranging from 1-3 year datasets spanning 1961 - 1976. Their fourth order polynomial "was found to be essentially the same as the relationship previously developed by Orgill and Hollands, although different data were used in each case" (Erbs et al., 1982). The authors highlight the importance of assessing seasonality in diffuse correlations quite effectively, and derive their own seasonal approach that "agrees closely" with empirical measurements (Erbs et al., 1982).

Equation 16 – Chandrasekaran and Kumar (1994)

$$k_d = 0.9686 + 0.1325k_t + 1.4183k_t^2 - 10.1862k_t^3 + 8.3733k_t^4 \quad \{\text{for } 0.24 < k_t \leq 0.80\};$$
$$k_d = 1.0086 - 0.178k_t \quad \{\text{for } k_t \leq 0.24\}; \text{ and}$$
$$k_d = 0.197 \quad \{\text{for } k_t > 0.80\}.$$

Chandrasekaran and Kumar (1994) distilled five years of hourly global and diffuse radiation data into the above fourth-order polynomial correlating the two in Madras, India (13.08°N). They compared results to those produced using Orgill and Hollands, Erbs et al., and Reindl et al. models, and applied a seasonal approach to refine correlations for the tropical seasons of "wet" and "dry" in Madras (Chandrasekaran & Kumar, 1994).

Equation 17 – Oliveira et al. (2002)

$$k_d = 0.97 + 0.8k_t - 3.0k_t^2 - 3.1k_t^3 + 5.2k_t^4 \quad \{\text{for } 0.17 < k_t < 0.75\};$$
$$k_d = 1.0 \quad \{\text{for } k_t \leq 0.17\}; \text{ and}$$
$$k_d = 0.17 \quad \{\text{for } k_t > 0.75\}.$$

Oliveira, Escobedo, Machado, & Soares (2002) derived the above fourth-order polynomial hourly model from data collected between 1994 – 1999 in the city of São Paulo, Brazil (23.55°S). They also produced daily and monthly correlations. At the time, this was the only known correlation for South America. They concluded performance will improve if seasonal biases are taken into consideration, there is a strong correlation between k_d and k_t as a predictor, and that the effects of elevation and pollution can be significant factors affecting k_d results given similar k_t contexts (Oliveira et al., 2002).

Equation 18 – Soares et al. (2004)

$$k_d = 0.90 + 1.1k_t - 4.5k_t^2 + 0.01k_t^3 + 3.14k_t^4 \qquad \{\text{for } 0.17 < k_t < 0.75\};$$
$$k_d = 1.0 \qquad \{\text{for } k_t \leq 0.17\}; \text{ and}$$
$$k_d = 0.17 \qquad \{\text{for } k_t > 0.75\}.$$

The work of Soares et al. (2004) is closely related to Oliveira et al. (2002), as it shares 3 authors and is also based on data from São Paulo, Brazil (though from 1998 – 2001). This model differs in its use of a neural network approach and its assessment of additional meteorological parameters to improve model performance. They conclude that k_t is a dominant sole predictor of k_d, and given the regional context for cloud cover, long-wave radiation is most helpful compared to other parameters, like temperature and atmospheric pressure (Soares et al., 2004).

Solar Analyst

The above surface and atmospheric parameters were derived and tested to ensure maximum representation of the urban canopy, clearness, and diffuse fraction characterizing Victoria, and used in the Solar Analyst tool with the following parameters.

Model Parameters

The Solar Analyst tool for "area solar radiation" was run using the following static set of local parameters: in_surface_raster (inRaster), latitude (48.4222), sky_size (200), time_configuraiton (TimeWithinDay (DOY, 0, 24)), day_interval = 14, hour_interval = 0.2, each_interval = "NOINTERVAL", zFactor = 1, slope_aspect_input_type = "FROM_DEM", calculation_directions = 32, zenith_directions = 18, azimuth_divisions = 16, diffuse_model_type = "UNIFORM_SKY", diffuse_proportion = diffuse, transmittivity = k_daily, outDirectRad = " ", outDiffuseRad = " ", outDirectDur = " ")

The “inRaster” variable pulled from a copy of the input DSM that was appended with the day of year (DOY) for file management purposes. Latitude of 48.4222N was chosen, as it’s the mean representative latitude of Victoria. A sky size of 200 was chosen to be in line with what Fu and Rich cite as being “ sufficient for most purposes”, and 32 sky directions, 18 zenith divisions, and 16 azimuth divisions were used to model sky maps and sky sectors in line with what they consider appropriate for detailed analyses (1999). Tests were run using sky size of 400 and calculated directions of 64, and led to ~3x more computation time with few differences in resulting Wh/m^2 values. The slope and aspects of each cell in the DSM were taken into account using the “FROM_DEM” variable, instead of having the model assume each cell to be a flat surface. Diffuse radiation was modelled to originate from a uniform sky, using the diffuse fraction and clearness indices generated from the solar climatology and Orgill and Hollands model in a list referred to as “k_daily”. The k_daily file is also where the DOY variable was scrubbed for use in the model. In the interest of time, only GHI outputs were generated, not diffuse or direct layers.

Script Execution

Related to the interests of time, the Solar Analyst tool was executed using a geoprocessing script written in ArcGIS’ extensible language of Python (v2.7). Using a script (Appendix F) allowed for the parsing of the k_daily file (containing the DOY, atmospheric clearness, and diffuse fraction), the generation of the folders/rasters/filenames for each run, as well as the execution of the Solar Analyst model itself, all passed as functions in the one script. Generation of temporary directories was required for each in/output raster as the script would result in an error if the same folder was used (even with overwrite toggled), so pre-setting up directories for each of the 365 model runs was required (Appendix G).

Tests were performed prior to batching the process. The model run using default parameters took ~ 12.5 hours, and with the slightly higher resolution set of parameters took ~ 16.7 hours. Considering the logistics of iterating the model for each of the 365 runs, as well as inputting the corresponding clearness and diffuse fractions for each one, a scripting approach was taken and left less room for operator error in data entry as well. Nevertheless, even being run on a server-grade workstation (32GB DDR3-1600 ECC RAM, Intel Xeon E5-2630 6-core V2 processor, with NVIDIA Quadro K4200 graphics card) the annual set of daily models would have taken ~254 days to complete.

Parallel Processing

To expedite the execution of the solar models, parallel processing was employed to leverage the 6 cores (12 threads) available from the central processing unit. Using the Python *multiprocessing* library, job pools proportional to the threads wanting to be used (12) were created and mapped to the model function running the above geoprocessing script. Each run of the model occurs when a thread becomes available to the pool.

Solar Analyst (modelled) Vs. Measured (Study Sites)

Daily insolation (kWh) totals were computed for the cells in the Solar Analyst results that match the empirical measurement locations at each of the study sites using ArcGIS's model builder and zonal statistics. The modelled versus measured values were compared using Python (v3.6) to calculate the Pearson product-moment correlation coefficients:

Equation 19 - Pearson product moment correlation coefficient

$$\rho_{(x,y)} = \frac{\sum(x - \bar{x})(y - \bar{y})}{\sqrt{\sum(x - \bar{x})^2 \sum(y - \bar{y})^2}}$$

Where ρ is the Pearson product moment correlation coefficient, $\bar{x}$ is the mean of x, and $\bar{y}$ is the mean of y.

Chapter 3: Results

Surface

DSM

A high-resolution ($1m^2$) DSM of Victoria’s urban canopy was created for use as input to Solar Analyst. This surface model ranges in elevation from - 3m ASL to 127m ASL, and covers the spatial extent of the city of ~20 km^2. An oblique perspective of study site #1 displays good results of roof plane consistency, chimney representation, roof edge alignment with building footprints, and overall characterization of surface features (Figure 12).

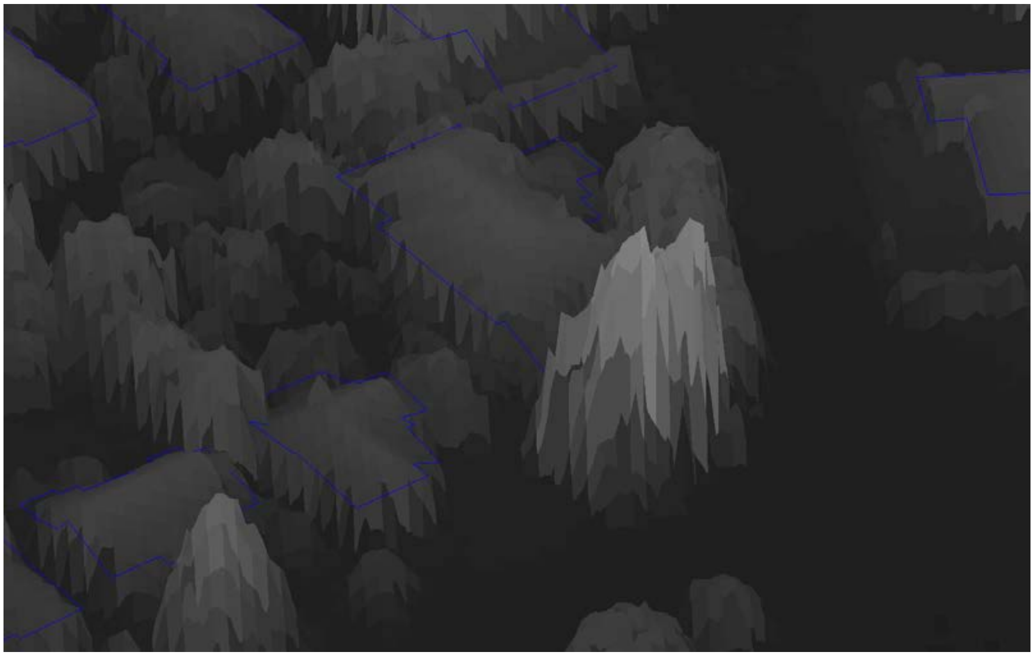

Figure 12 – The resulting DSM at study site #1, oriented at an oblique angle and in a northwards (~ 18°) direction.

Atmosphere

Annual Daily Clearness

Annual daily atmospheric clearness (K_t) indices were derived from the regional solar climatology and TOA insolation for 2005 – 2015. Interpolated surfaces (samples in Figure 14 & Figure 15) were produced to render one set of annual daily values representative of Victoria for input to Solar Analyst. The distribution of annual daily K_t for Victoria ranges from 0.226 to 0.680, and has a mean of 0.462 and standard deviation of 0.114. To provide a smoothed and continual visual of the distribution, a histogram of the data is overlaid with a kernel density estimate (KDE) (Figure 13). The KDE is helpful in determining shape of the distribution, which exhibits negative skewness with a density of relatively higher frequency counts occurring between ~ 0.5 – 0.7.

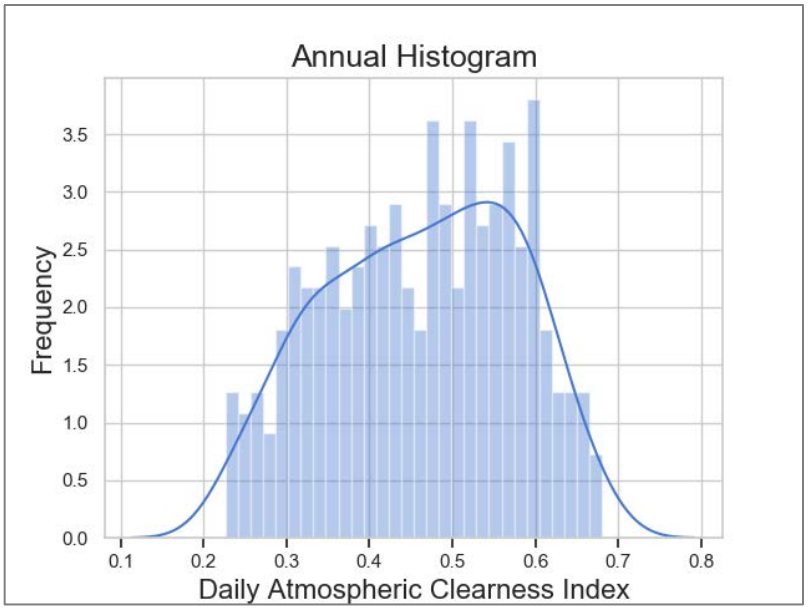

Figure 13 - Histogram of Annual Daily Atmospheric Clearness indices derived for Victoria

Annual daily K_t values expressed as a function of day exhibit a quasi-sinusoidal pattern throughout the year, and a moving average helps provide a smoother sense of this periodicity (Figure 16). Clearness tends to increase consistently from January 1 to where it peaks ~ day 200 (latter July), then clearness degrades relatively more rapidly from ~ day 250 (or beginning of Sept) through until ~ day 355 (winter solstice).

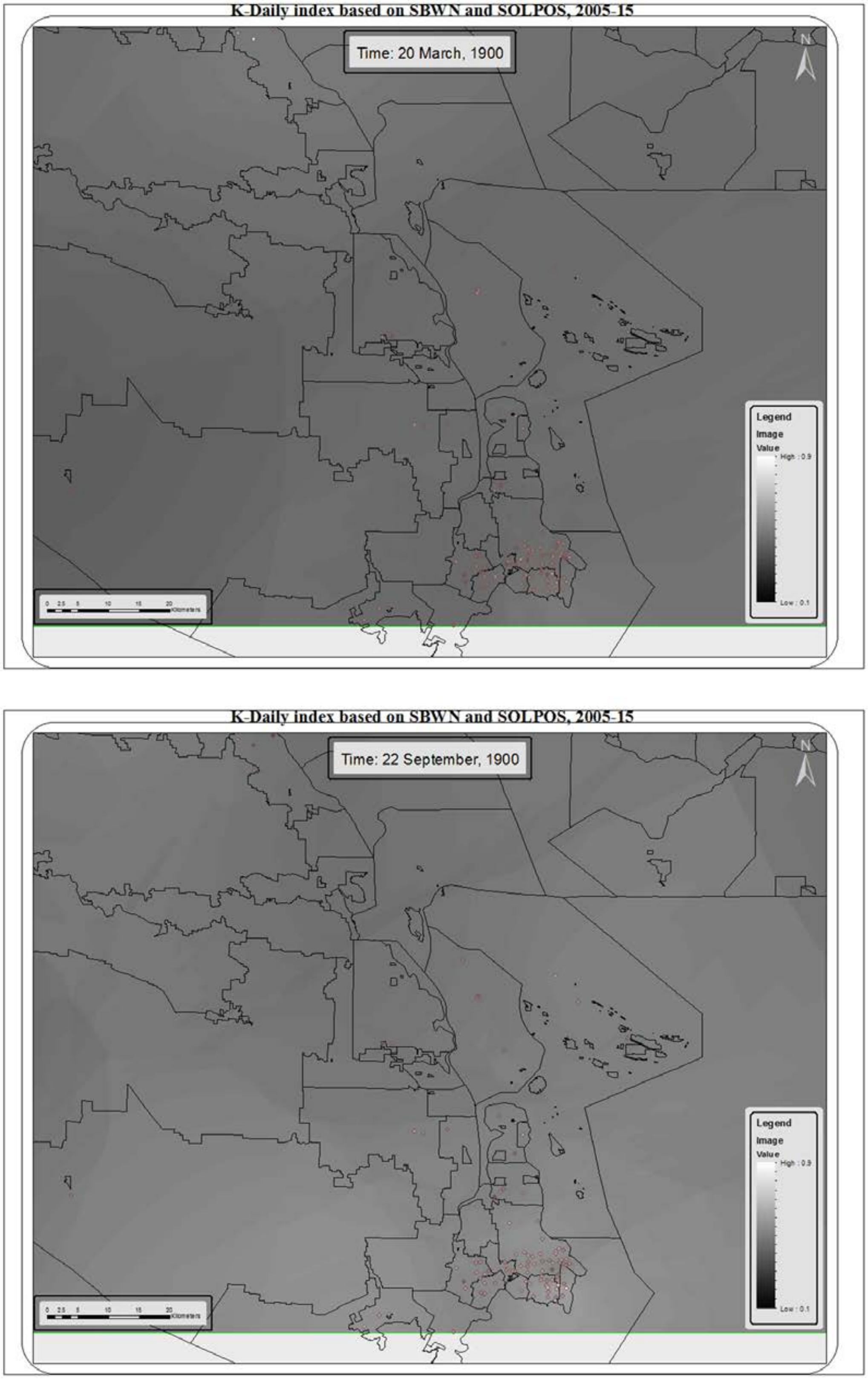

Figure 14 – Regional interpolated surfaces for daily atmospheric clearness on the equinoxes.

Figure 15 - Regional interpolated surfaces for daily atmospheric clearness on the solstices.

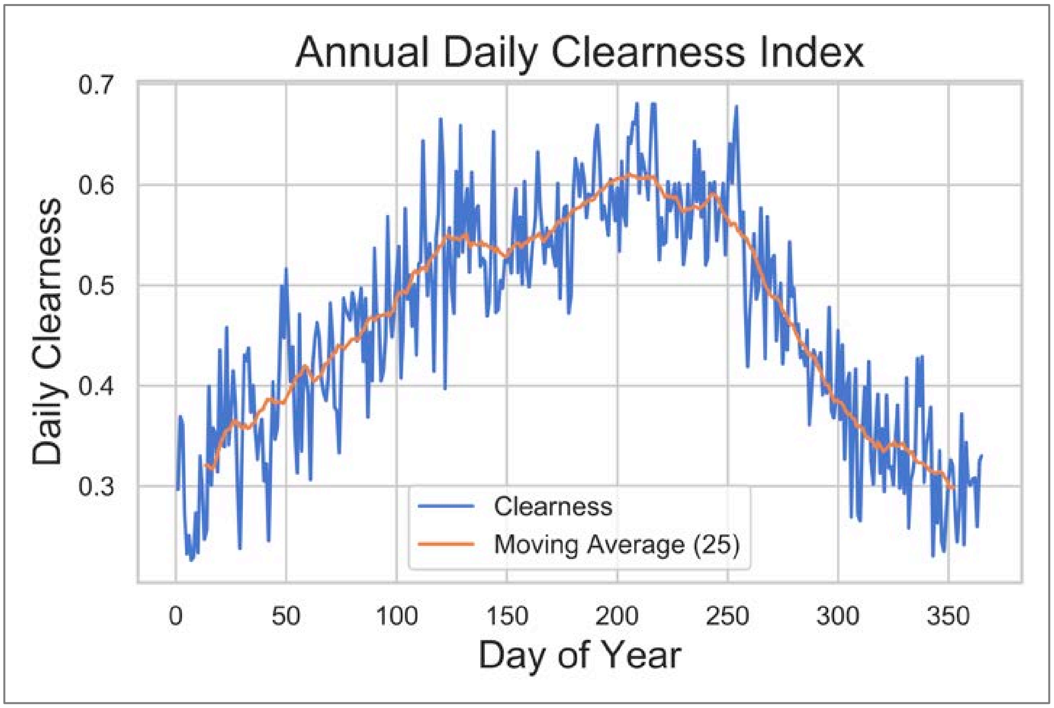

Figure 16 – Annual daily atmospheric Clearness overlaid with a moving average of 25 bins for smoothness and offset by 12.5 to be center-aligned.

Seasonal Daily Clearness

Plotted seasonal daily K_t values are useful for visualizing seasonal variability and trends throughout a year (Figure 17). Tabulated seasonal K_t values (Table 3) show winter experiences the least clearness (mean = 0.339), summer is the most clear (mean = 0.580), and spring and fall seasons are periods of transition, with rapidly changing clearness trends indicated by them having the highest standard deviations, at 0.072 and 0.100 respectively. The maximum K_t values for spring (0.665), summer (0.680), and fall (0.678) differ by only 0.015, whereas winter's maximum (0.516) is significantly lower than the rest.

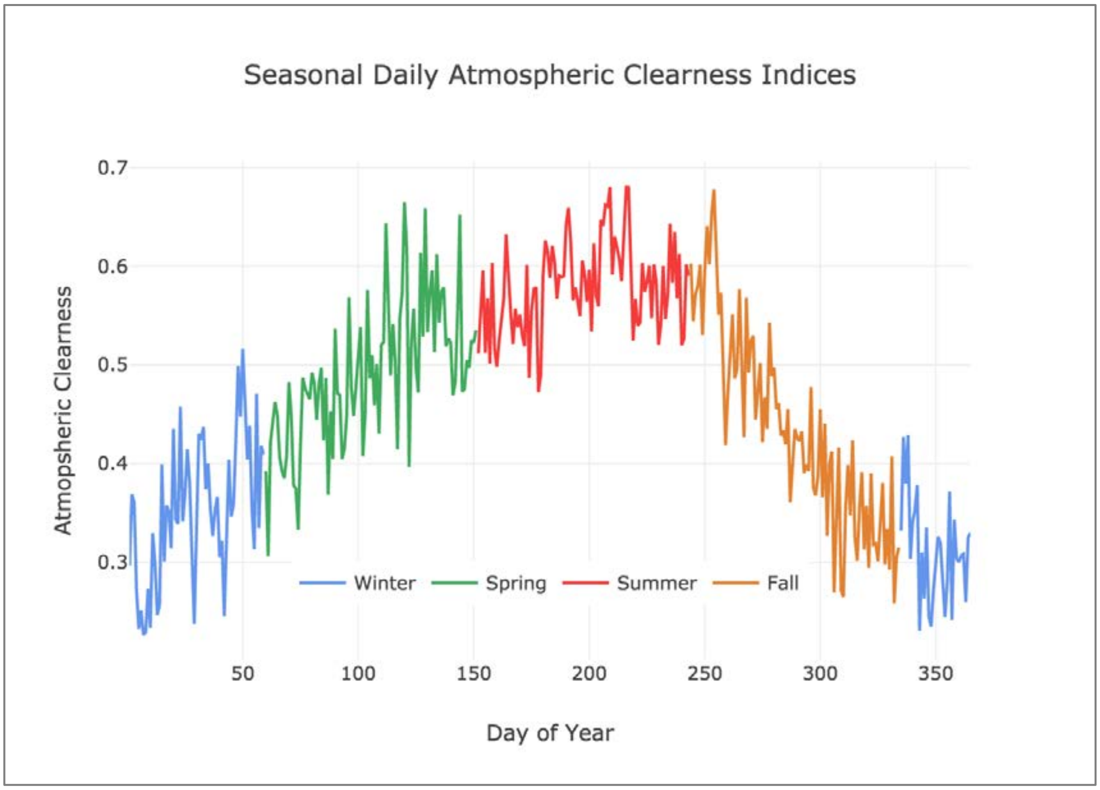

Figure 17 - Annual daily atmospheric clearness highlighting the days by season

Table 3 – Seasonal average daily atmospheric clearness index statistics

Season	*count*	*mean*	*std*	*min*	*50%*	*max*
Fall	91	0.436	0.100	0.258	0.426	0.678
Spring	92	0.491	0.072	0.306	0.487	0.665
Summer	92	0.580	0.046	0.472	0.581	0.680
Winter	90	0.339	0.069	0.226	0.334	0.516

Seasonal KDE plots of K_t help visually compare seasonality of clearness (Figure 18). Spring and winter kernel densities are relatively similar in shape and spread, though offset by ~ 0.1 on either side. The fall season experiences the largest range of clearness, spanning almost the entire range of all other seasons, which is reflected by it having the largest standard deviation of 0.100. Summer clearness is concentrated about its mean of 0.580, spanning the least range of values compared to other seasons, as reflected by it having the smallest standard deviation of 0.046.

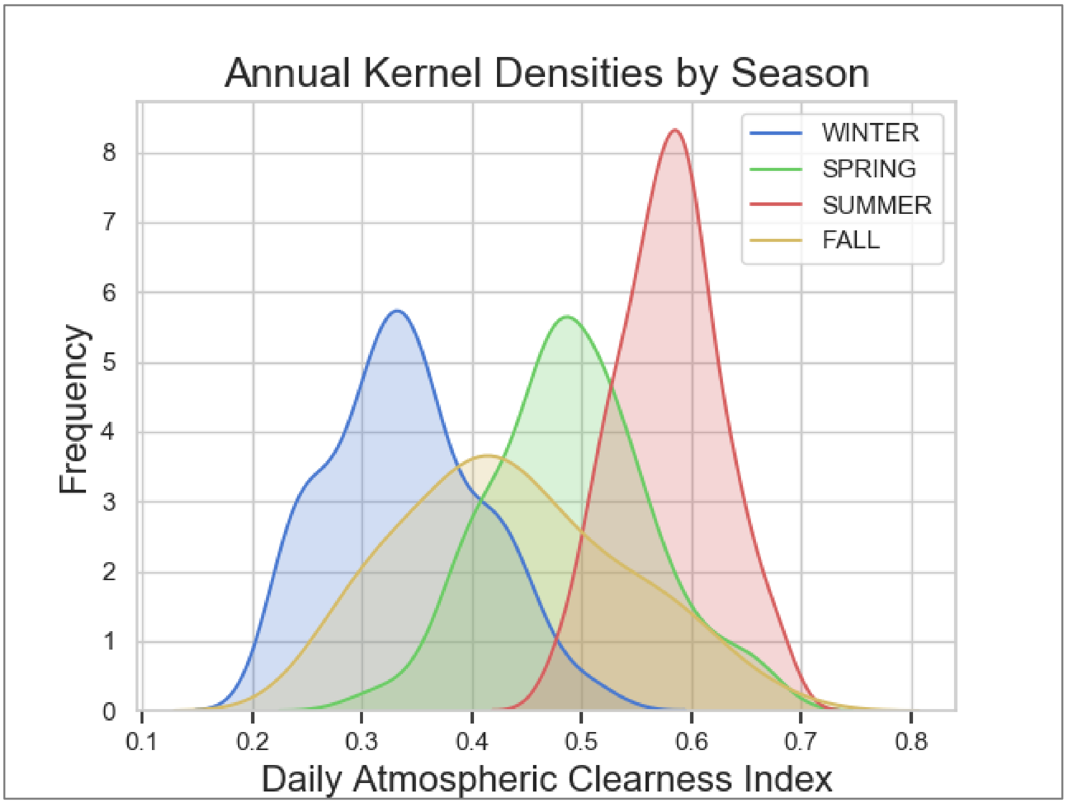

Figure 18 - Kernel densities of annual daily clearness indices grouped by season

Annual Daily Diffuse Fraction – Standard Models

In an effort to comment on the universality and any biases in the Orgill and Hollands model, the same set of annual daily K_t values generated for Victoria was used to compute diffuse fraction from the standard models, as per Jacovides et al. (2006). Additionally, a "standard mean" dataset was created as the arithmetic mean of all standard models for each daily value, and used as a benchmark to gauge model bias from. A set of 4 scatterplots compare annual daily K_t values to the derived K_d results from the standard models and standard mean dataset: Figure 19 shows all of the models; Figure 20 shows the 3 lowest mean models; Figure 21 shows the 4 middle mean models, and Figure 22 shows the 3 highest mean models.

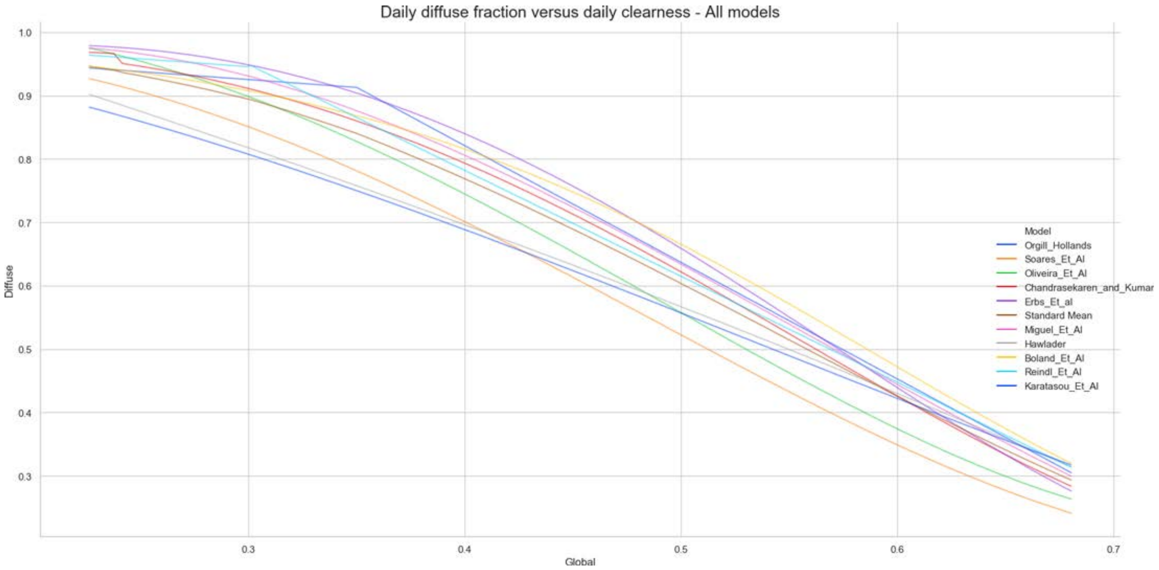

Figure 19 - Annual daily diffuse fraction versus clearness, for all models and standard mean

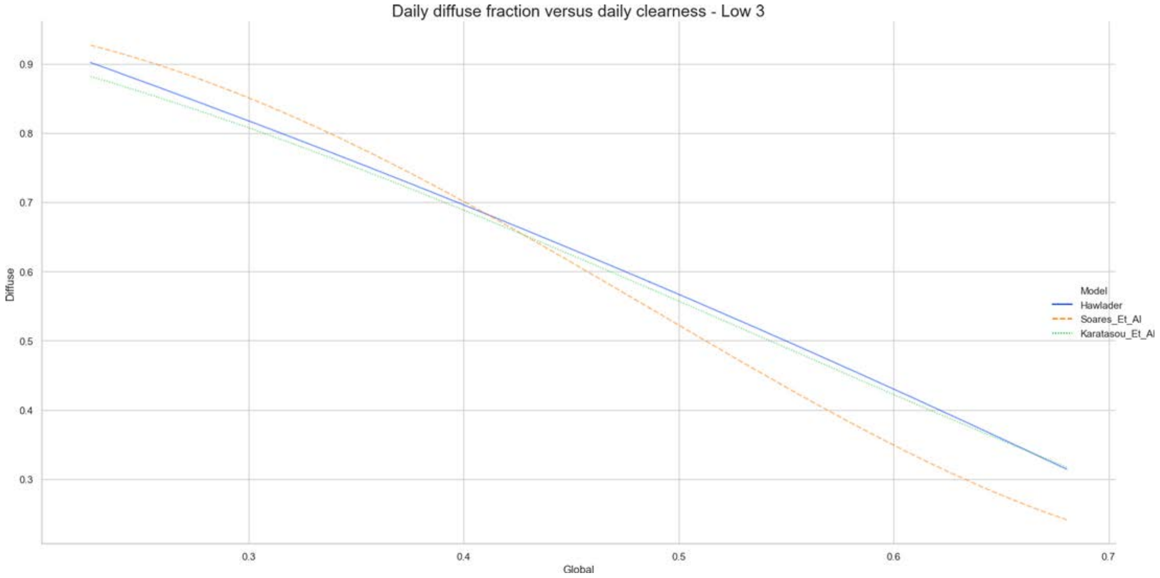

Figure 20 - Annual daily diffuse fraction versus clearness, for the lowest 3 models (by mean)

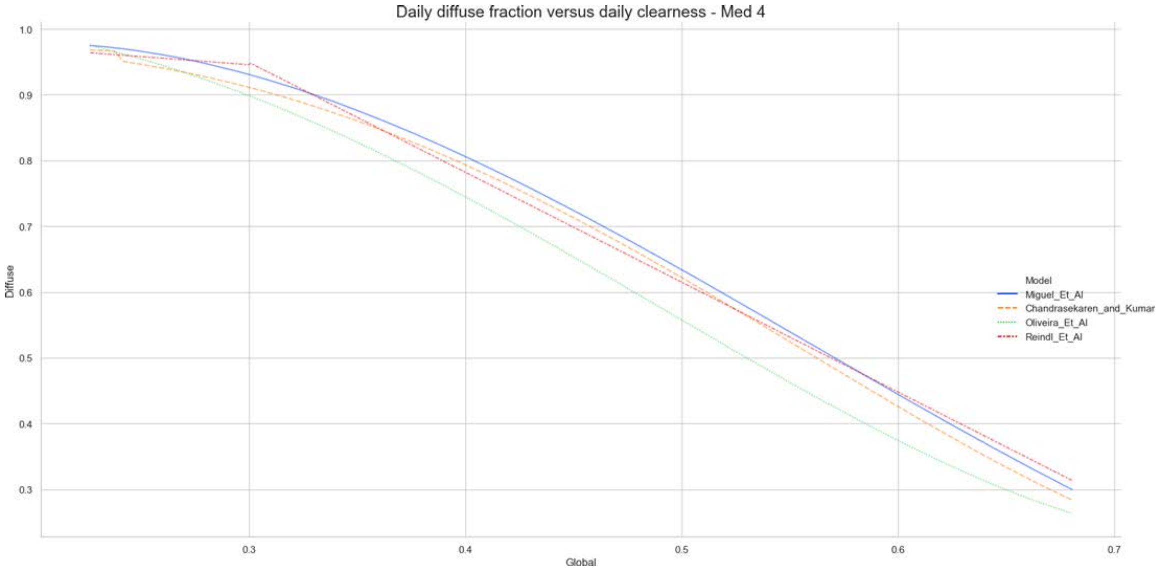

Figure 21 - Annual daily diffuse fraction versus clearness, for the mid 4 models (by mean)

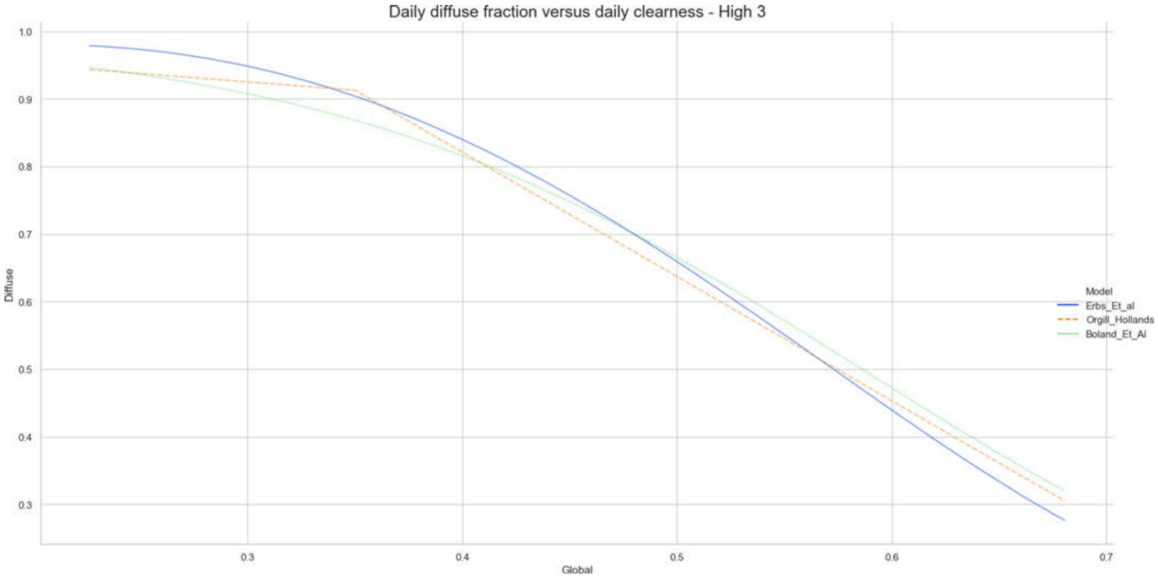

Figure 22- Annual daily diffuse fraction versus clearness, for the high 3 models (by mean)

Though figure 19 is crowded, it does allow for comparison of the model results, especially their shapes and biases. For example, Karatasou et al. (Equation 14) is relatively conservative with its estimates, as its slope is shallower than the rest of the models across all clearness indices, with lower K_d predictions in lower K_t conditions and higher K_d predictions in higher K_t conditions, than the rest. The models of Orgill and Hollands (Equation 9), Reindl et al. (Equation 10), and Chandrasekaran and Kumar (Equation 16), have a distinct break in their curves as the K_t values descend below their lower thresholds and the rest of the curve continues at steeper slopes. The figure of the lower mean models (Figure 20) shows how Hawlader (Equation 12) and Karatasou et al. (Equation 14) are almost identical, while Soares et al. (Equation 18) is noticeably steeper in slope such that lower K_t conditions render higher K_d results and higher K_t indices result in high K_d values than the other two. The models closest to the annual daily mean (Figure 21) all share similar correlation and curve shapes, except for Oliveira (Equation 17), which results in noticeably lower K_d values than the other three. Also in this figure, and as already mentioned, Reindl et al. (Equation 10) and Chandrasekaran and Kumar (Equation 16) deviate in shape from the other correlations once K_t values extend lower than their lower thresholds (0.3 and 0.24, respectively. The models with the highest mean annual daily diffuse results (Figure 22) include Orgill and Hollands (Equation 9), Boland et al. (Equation 11), and Erbs et al. (Equation 15). Both Boland et al. (Equation 11) and Orgill and Hollands (Equation 9) commence and finish roughly with the same values, separated only when model Orgill and Hollands (Equation 9) approaches its lower K_t threshold (0.35) and results in higher K_d values than both of the others. The Erbs et al. (Equation 15) model results in a slightly steeper correlation than the other two, leading to higher K_d values in lower K_t conditions and lower K_d values with higher K_t conditions than the other two. To compare the distributions of model results, gauging them for biases, their variability, and any outliers, boxplots were created for each model and standard mean dataset, arranged by mean, and overlaid with individual observations (Figure 23). Models Hawlader (Equation 12) and Karatasou et al. (Equation 14) display the lowest range of K_d values, corroborated by their standard deviations of 0.148 and 0.146 respectively (Table 6). The remaining models share similar ranges that span between ~ 0.169 and 0.198, but this changes with seasonal analysis.

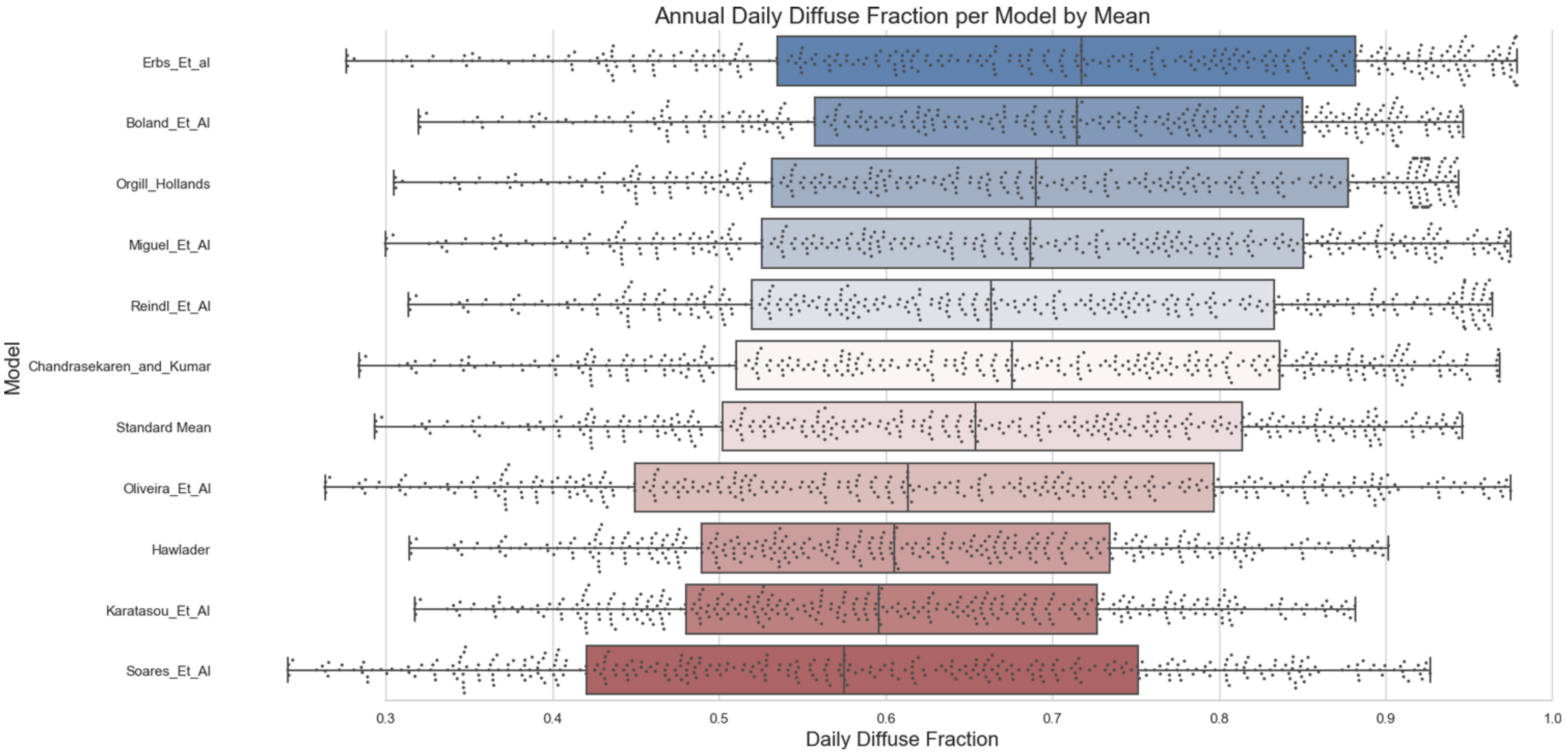

Figure 23 - Boxplots of annual daily diffuse fraction results derived from all models, including the standard mean, and overlaid with unique calculations.

Table 4 - Annual diffuse fraction statistics for all models, including the standard mean set

Model	*mean*	*std*	*min*	*50%*	*max*
Boland_Et_Al	0.697	0.169	0.320	0.715	0.947
Chandra._and_Kumar	0.668	0.186	0.284	0.676	0.968
Erbs_Et_al	0.700	0.196	0.276	0.717	0.979
Hawlader	0.612	0.148	0.314	0.605	0.902
Karatasou_Et_Al	0.603	0.146	0.317	0.596	0.882
Miguel_Et_Al	0.683	0.185	0.300	0.687	0.975
Oliveira_Et_Al	0.622	0.198	0.263	0.613	0.975
Orgill_Hollands	0.690	0.185	0.305	0.690	0.944
Reindl_Et_Al	0.673	0.182	0.314	0.663	0.964
Soares_Et_Al	0.585	0.189	0.241	0.575	0.927
Standard Mean	0.653	0.178	0.293	0.654	0.946

Annual Daily Diffuse Fraction – Seasonal / Model-Specific

Though Jacovides et al. (2006) state that seasonal dependencies in the standard models are expected to be more pronounced in hourly diffuse fraction than daily results; this study identifies some clear seasonal trends in the daily values generated.

Seasonal Diffuse Fraction – General

Using the seasonal statistics of the standard mean dataset, general observations on seasonality of all standard models can be made (Table 4). The lowest average K_d value occurs in summer (0.463) and the highest in winter (0.839), which are also the seasons where the lowest average minimum (0.293) and highest average maximum (0.946) occur, respectively. The range of K_d values, as gauged by standard deviations, vary much more widely in the fall (0.157) than in the spring (0.121); moreover, both fall and spring vary considerably more than K_d values in summer (0.081) and winter (0.084).

Table 5- Seasonal daily diffuse fraction averages for all models combined

Season	*mean*	*std*	*min*	*max*
Fall	0.699	0.157	0.298	0.926
Spring	0.616	0.121	0.317	0.888
Summer	0.463	0.081	0.293	0.651
Winter	0.839	0.084	0.575	0.946

Seasonal Diffuse Fraction – Model-Specific

Model-specific seasonal statistics are tabulated (Table 6) and plotted as KDEs for visual comparison (Figure 24). In general, seasonal kernel densities for each model exhibit similar distributions in terms of shape, range, and frequencies, with some exceptions in winter.

Spring

All models exhibit symmetrical, unimodal shapes in their kernel density estimates, and are the second lowest $K_d$values compared to other seasons. Mean K_d value for all models in spring is 0.616, and the highest mean (0.671) is Boland et al. (Equation 11) while the lowest mean (0.540) is Soares et al. (Equation 18). Spring's highest max K_d value (0.944) is Erbs et al. (Equation 15) while the lowest minimum (0.258) is Soares et al. (Equation 18). Erbs et al. (Equation 15) is also the model with the largest standard deviation (0.141), while Karatasou et al. (Equation 14) and Hawlader (Equation 12) vary the least at 0.095 and 0.096, respectively.

Summer

All models exhibit symmetrical, unimodal shapes in their kernel density estimates, and are the lowest K_d values compared to other seasons. Mean K_d value for all models in summer is 0.463, and the highest mean (0.512) is Boland et al. (Equation 11) while the lowest mean (0.386) is Soares et al. (Equation 18). Summer's highest max K_d value (0.715) is Erbs et al. (Equation 15), with Boland et al. (Equation 11) a close second (0.713), while the lowest minimum (0.241) is Soares et al. (Equation 18). The widest range in values (0.100) is Erbs et al. (Equation 15), with Boland et al. (Equation 11) a close second (0.090), while Karatasou et al. (Equation 14) and Hawlader (Equation 12) vary the least with 0.062 and 0.064, respectively.

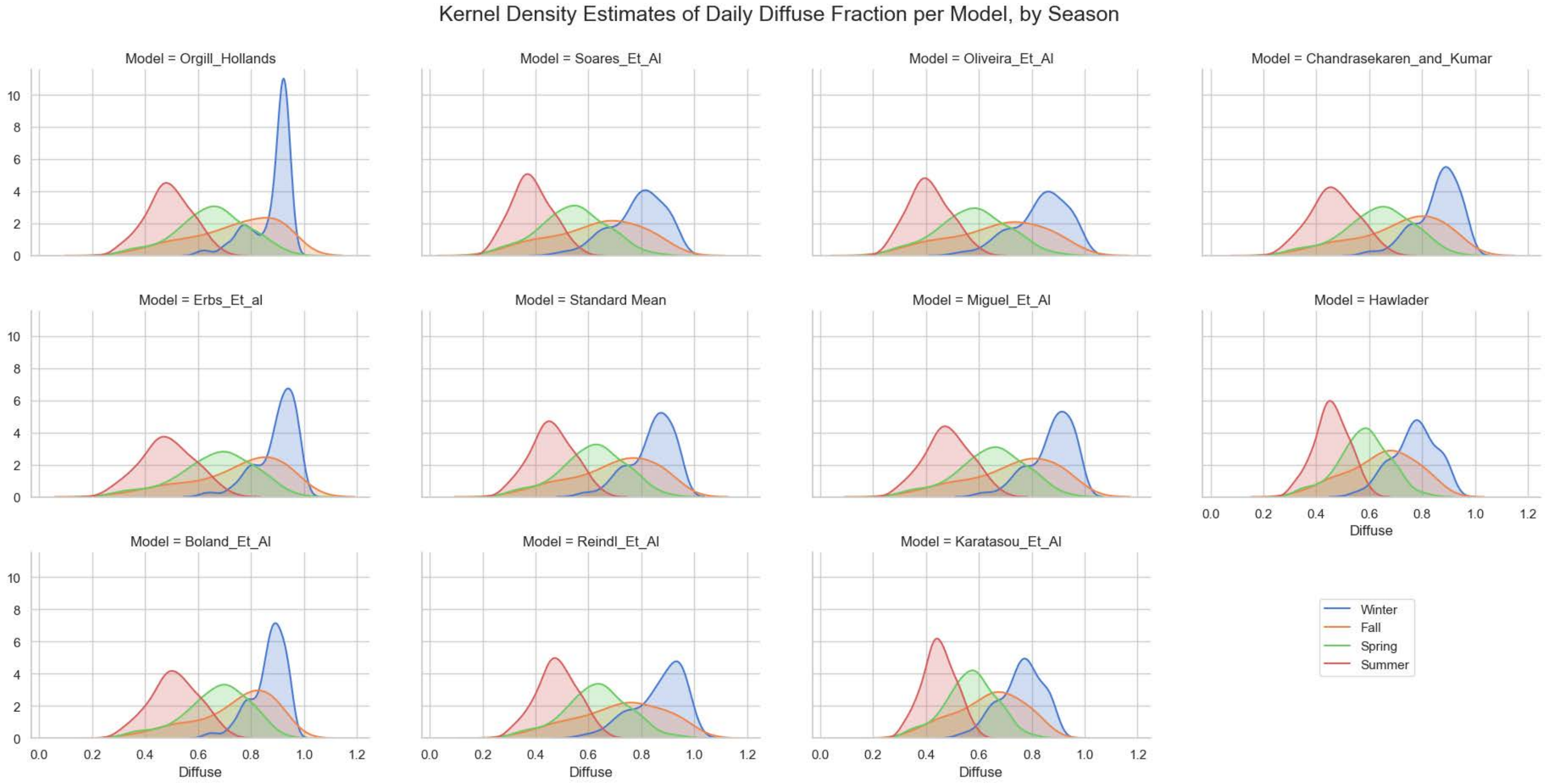

Figure 24 - Seasonal kernel density estimates of daily diffuse fraction results for all standard models

Fall

All models exhibit slight negative skewness and a unimodal shape in their kernel density estimates, and are by far the highest ranging (0.157) K_d values compared to other seasons. Mean K_d values for all models in fall is 0.699, with the highest mean (0.753) being Erbs et al. (Equation 15) and the lowest mean (0.631) being Soares et el. (Equation 18). Fall's highest max K_d value (0.970) is Erbs et al. (Equation 15) and lowest minimum (0.244) is Soares et al. (Equation 18). Oliveira et al. (Equation 17) is the most varied (0.175), with Erbs et al. (Equation 15) coming a close second (0.172), while Karatasou et al. (Equation 14) and Hawlader (Equation 12) vary the least, both with 0.129.

Winter

All models exhibit negative skewness and a slight bimodal shape in their kernel density estimates, and contribute to the season having the highest mean (0.839) values compared to others. Orgill and Hollands (Equation 9), Erbs et al. (Equation 15), and Boland et al. (Equation 11) have more pronounced densities around higher K_d values. Orgill and Hollands (Equation 9) has a particularly dense mode of 36 K_d values between 0.915 – 0.925, which coincide with values around its lower K_t threshold of 0.35. That said, highest mean K_d value for winter (0.898) belongs to Erbs et al. (Equation 15). The lowest value (0.759) belongs to Karatasou et al. (Equation 14), though Hawlader (Equation 12) is a close second lowest (0.769). The highest max K_d value (0.979) belongs to Erbs et al. (Equation 15), with Miguel et al. (Equation 13) and Oliveria et al. (Equation 17) tied for a close second (0.975). Winter's lowest minimum (0.493) belongs to Soares et al. (Equation 18). The widest range in values belongs to Oliveira et al. (Equation 17) and Soares et al. (Equation 18), with 0.103 and 0.100, respectively, while the least range (0.066) is Boland et al. (Equation 11), with Orgill and Hollands (Equation 9) the second lowest (0.076).

Table 6 - Seasonal diffuse fraction statistics for each model and standard mean

Model	*season*	*mean*	*std*	*min*	*50%*	*max*
Boland_Et_Al	**Fall**	0.742	0.148	0.324	0.782	0.932
	Spring	0.671	0.121	0.347	0.689	0.904
	Summer	0.512	0.09	0.320	0.509	0.713
	Winter	0.866	0.066	0.636	0.882	0.947
Chand._and_Kumar	**Fall**	0.716	0.163	0.288	0.752	0.942
	Spring	0.633	0.129	0.308	0.647	0.906
	Summer	0.467	0.088	0.284	0.462	0.673
	Winter	0.860	0.082	0.591	0.878	0.968
Erbs_Et_al	**Fall**	0.753	0.172	0.281	0.798	0.970
	Spring	0.668	0.141	0.304	0.687	0.944
	Summer	0.485	0.100	0.276	0.481	0.715
	Winter	0.898	0.077	0.625	0.920	0.979
Hawlader	**Fall**	0.646	0.129	0.318	0.663	0.866
	Spring	0.577	0.096	0.337	0.585	0.810
	Summer	0.458	0.064	0.314	0.456	0.603
	Winter	0.769	0.083	0.545	0.776	0.902
Karatasou_Et_Al	**Fall**	0.638	0.129	0.321	0.655	0.851
	Spring	0.569	0.095	0.337	0.575	0.800
	Summer	0.450	0.062	0.317	0.447	0.594
	Winter	0.759	0.081	0.535	0.768	0.882
Miguel_Et_Al	**Fall**	0.731	0.163	0.304	0.764	0.962
	Spring	0.646	0.128	0.326	0.659	0.925
	Summer	0.484	0.086	0.300	0.480	0.684
	Winter	0.875	0.084	0.604	0.895	0.975
Oliveira_Et_Al	**Fall**	0.671	0.175	0.266	0.697	0.946
	Spring	0.576	0.131	0.280	0.583	0.890
	Summer	0.414	0.079	0.263	0.406	0.611
	Winter	0.833	0.103	0.526	0.851	0.975
Orgill_Hollands	**Fall**	0.740	0.164	0.310	0.772	0.936
	Spring	0.653	0.130	0.333	0.662	0.924
	Summer	0.490	0.085	0.305	0.487	0.688
	Winter	0.880	0.076	0.607	0.917	0.944
Reindl_Et_Al	**Fall**	0.719	0.163	0.318	0.738	0.956
	Spring	0.631	0.120	0.339	0.638	0.938
	Summer	0.482	0.077	0.314	0.479	0.661
	Winter	0.866	0.093	0.588	0.892	0.964
Soares_Et_Al	**Fall**	0.631	0.167	0.244	0.656	0.898
	Spring	0.540	0.124	0.258	0.547	0.843
	Summer	0.386	0.075	0.241	0.379	0.573
	Winter	0.788	0.100	0.493	0.804	0.927

Seasonal Model-Specific Deeper Dive

To explore the Orgill and Hollands (Equation 9) model further, especially its seasonal nuances, it is visually compared to the standard mean dataset in terms of seasonal daily diffuse fraction histograms and kernel density plots (Figure 25). Compared to the standard mean, Orgill and Hollands (Equation 9) predicts higher K_d values in all seasons. Their shape, mode, and skewness are roughly similar in spring, summer, and fall, though slightly more negatively skewed in Orgill and Hollands (Equation 9). In winter, Orgill and Hollands (Equation 9) deviates more dramatically from the standard mean, especially in K_d values higher than ~0.8. This is the result of the aforementioned concentration about its mode at ~0.92, attributed to its lower threshold, leading to it being noticeably denser than the standard mean around this K_d value.

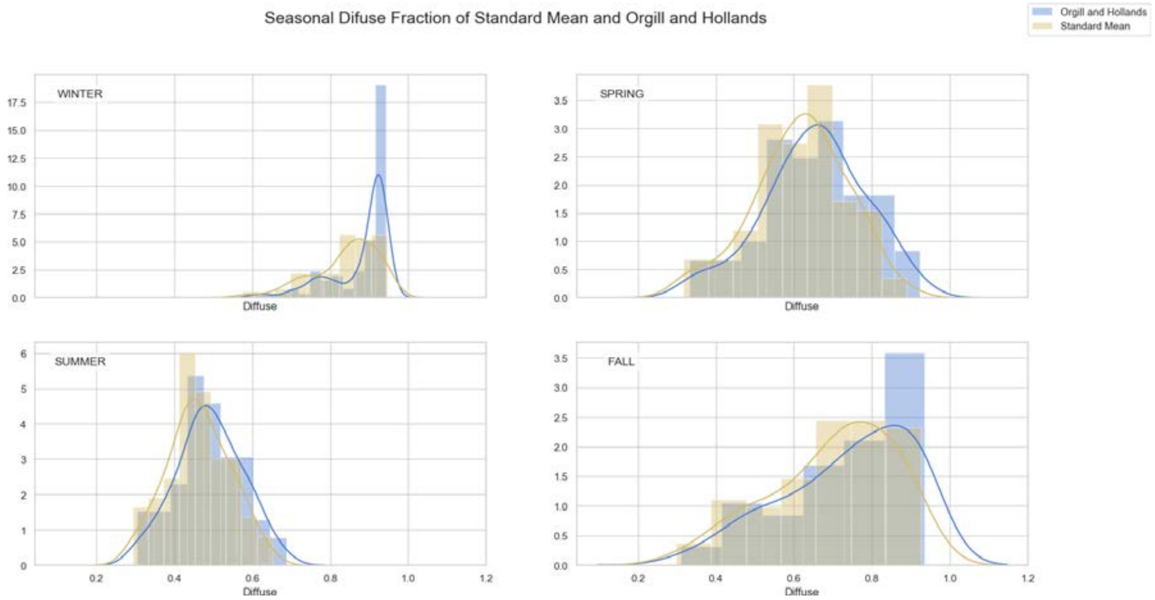

Figure 25 - Seasonal histograms & overlaid KDEs for Standard Mean / Orgill & Hollands

To better understand any biases towards extreme K_d value predictions, seasonal occurrences of models that render the highest daily diffuse fraction were assessed (Figure 26). It is interesting to note that only 3 models predict the maximum daily diffuse fraction value for any day of the year: 153 of the maximum values are predicted by Erbs et al. (Equation 15) during lower K_t days (winter); 153 occurrences are predicted by Boland et al. (Equation 11) during higher K_t days (summer); and 19 are maximums predicted by the Orgill and Hollands (Equation 9) model, with instances occurring in both winter and fall.

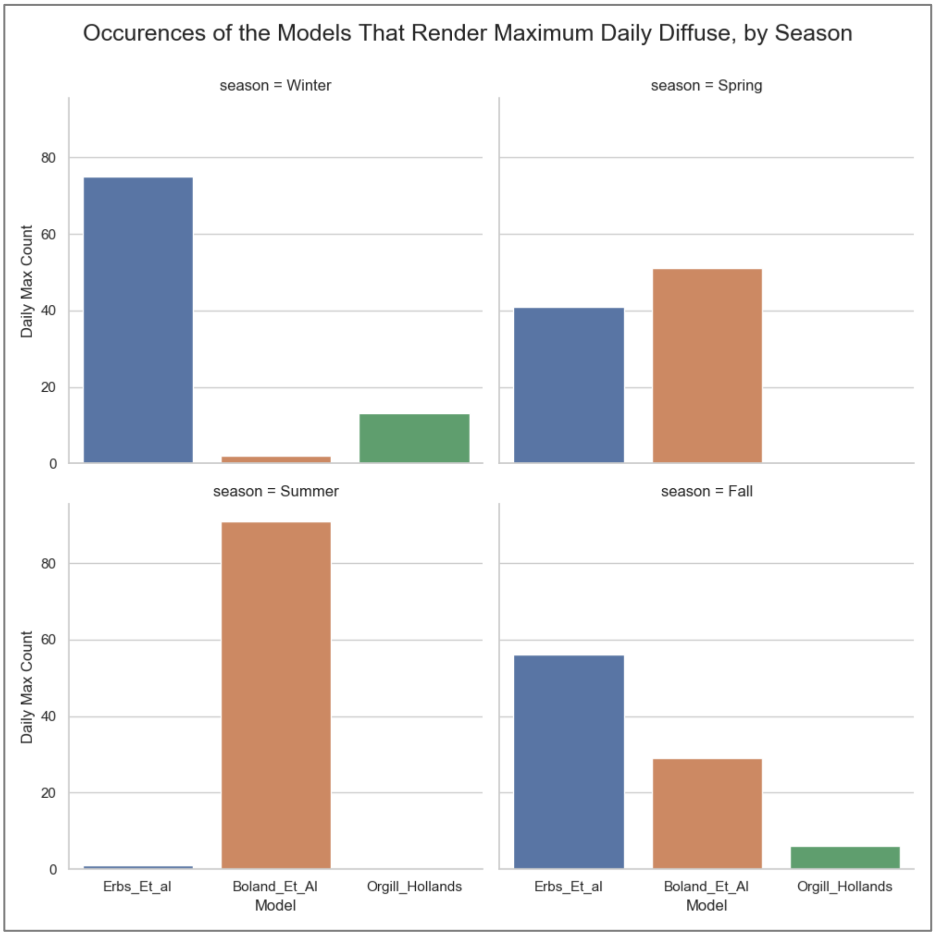

Figure 26 - Frequency of models that render the maximum daily diffuse fraction, by season

Based on this set of K_t values, the Orgill and Hollands (Equation 9) model predicts the maximum $K_d$value 5.2% of the time compared to the other standard models. To assess how the model compares to the standard mean, its difference over the course of a year was calculated (Figure 27). Results show there is a lull in variance between the two datasets that starts around May 1st and continues to around October 1st, where the difference is on average ~ 0.025, compared to larger differences during the rest of the year averaging ~ 0.045. Thus, using this K_t dataset the Orgill and Hollands (Equation 9) model predicts K_d values closer in line with what other standard models predict during 5 months between late-spring and early-fall (typically clearer days), and then varies more throughout the other 7 (typically less clear) months.

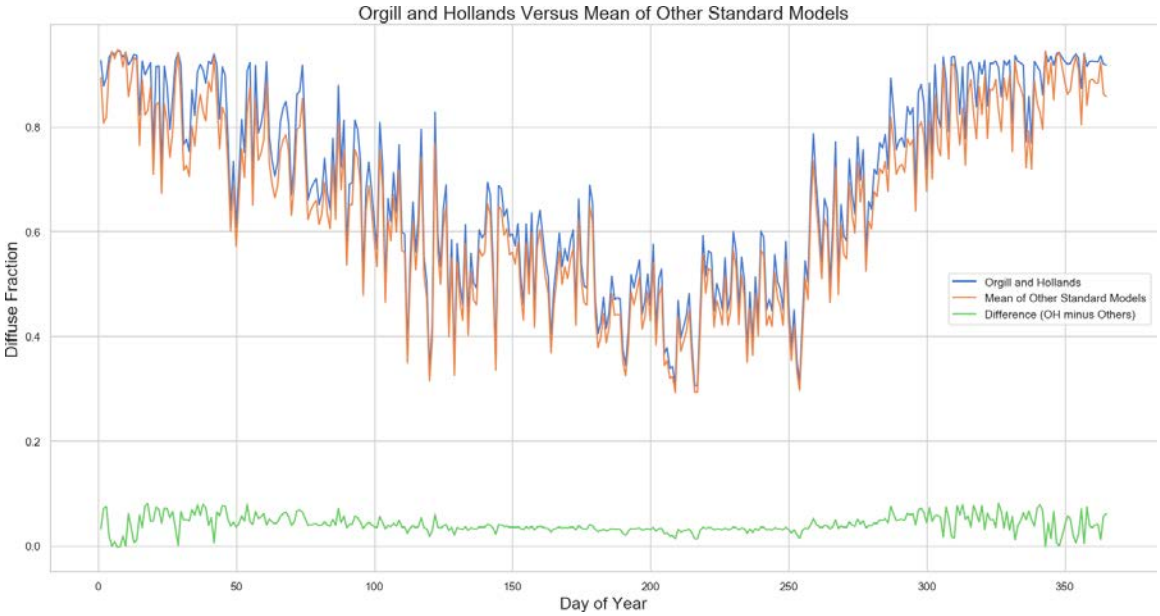

Figure 27 – Annual daily diffuse fraction of the standard mean versus Orgill and Hollands, with difference in values plotted as reference.

Solar Model

Solar Analyst

Daily GHI insolation maps were generated for an entire year using the DSM and atmospheric parameters derived to be as representative of Victoria as possible. Each resulting layer comprises 28,148,120 (5320 columns and 5291 rows) 1m^2 cells with a unique insolation value that covers the ~20km^2 area of the city. Each layer has a file size of 107.38MB, and the total annual dataset is ~39 GB. Of the 365 days modelled, 6 days (88, 101, 153, 271, 333, and 334) resulted in no insolation layer being generated. Default atmospheric parameters (0.5 for transmittivity and 0.3 for diffuse fraction) were used in re-run attempts, and 4 of the days processed, but 2 days (88 and 333) did not. The days that still did not process were then re-run with slight tweaks to the atmospheric parameters (i.e.: 0.49 and 0.29, instead of 0.5 and 0.3 for transmittivity and diffuse fraction, respectively), and still failed to generate output. These two days were then re-run using diffuse fraction output from the other standard global-to-diffuse models and neither of them completed. The K_t value for day 88 was 0.4532, and for day 333 was 0.3048. For simplicity and completeness, the Solar Analyst tool was re-engaged to generate monthly and annual insolation maps using the custom DSM, sky map/sector settings, and default atmospheric parameters. This resulted in a complete set of monthly and annual insolation (Figure 28) values for Victoria, which was preferred over daily sets for use in the City of Victoria's climate action initiatives. The annual statistics for the cells where empirical measurements were taken are presented (Table 7).

Table 7 – Annual insolation (kWh) statistics for study site cells using annual model results

Research Site	*Min*	*Max*	*Range*	*Mean*	*Standard Deviation*
#1 - Upper	1001	1012	11	1007	4
#1 - Lower	868	901	33	881	13
#2 – City Hall	1034	1050	16	1044	6

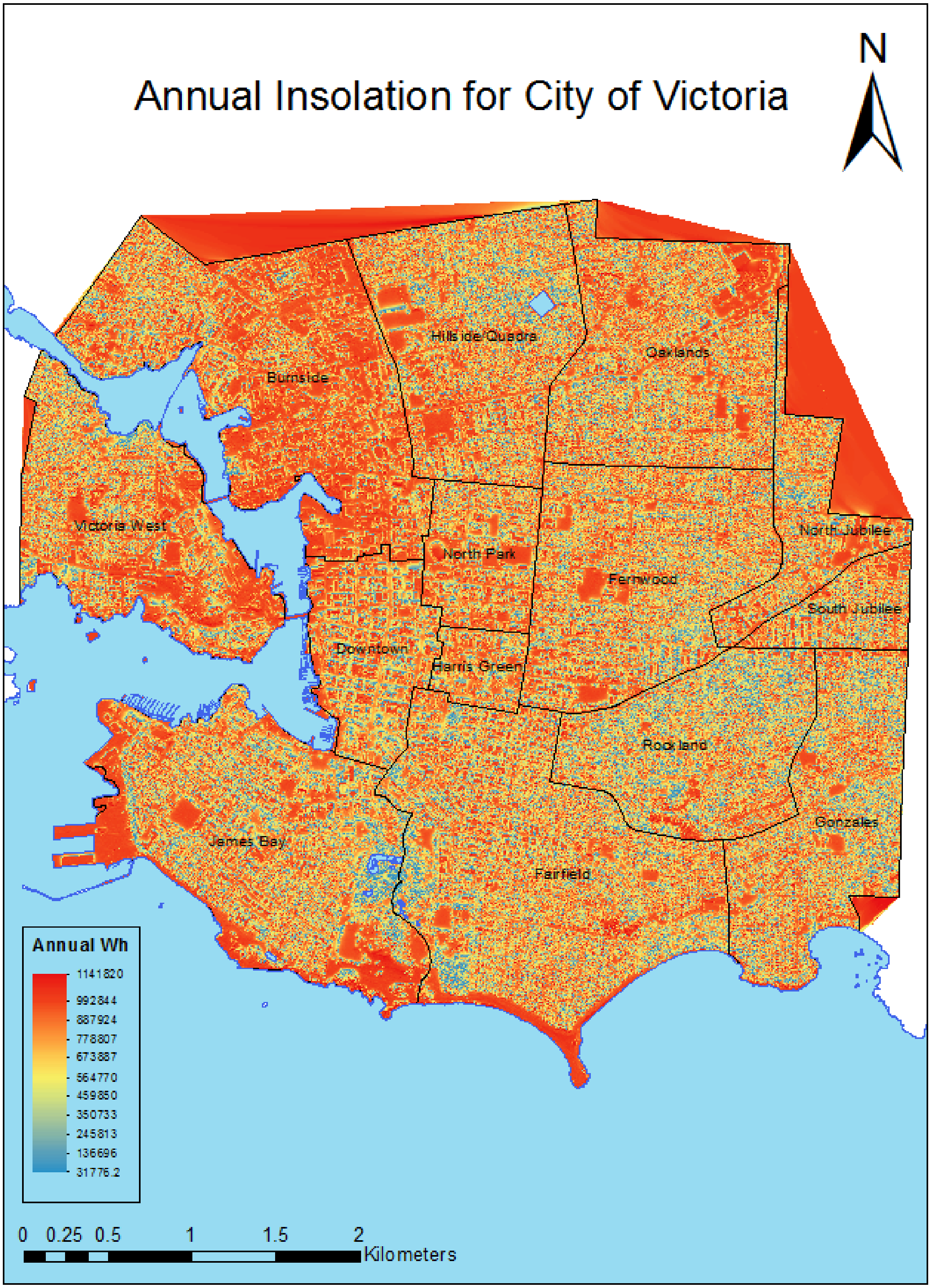

Figure 28 – Continuous surface map of annual insolation (in Wh) for the city of Victoria.

Solar Analyst (modelled) Vs. Measured (Study Sites)

Daily insolation (kWh) totals were compared between modelled and measured points (Figure 29). All three locations at the two study sites exhibit large positive correlations, with each being >0.8 and City Hall being closer to 0.9 (Table 8). The biggest difference in correlation occurs between the modelled and measured values at study site #1, with a difference in correlation values of 0.034. The distributions of all modelled and measured daily insolation datasets exhibit clear bimodality, and tend to correlate stronger towards those modes ~ 1 and 8 kWh.

Table 8 – Correlation of measured and modelled daily insolation values at each study site

Study Site	*Pearson product-moment correlation coefficient*
#1 - Upper	0.819
#1 - Lower	0.853
#2 – City Hall	0.859

As a function of day, modelled insolation assumes a quasi-parabolic shape throughout the year, with little variance aside from some off-trend values between ~ day 95 – 180 and a couple ~ day 270 – 285 (Figure 30). The empirical sets at all 3 locations vary much more throughout the year than the modelled, though a similar curve signal is discernible through the noise. Empirical measurements vary most between day ~95 – 300, and tend to vary less from the modelled through the late fall and winter periods. The empirical values for the Lower roof group closer between ~ day 125 – 225, following a clear upper limit in a parabolic trend, though gradually more offset from the modelled closer to the peak ~ day 172.

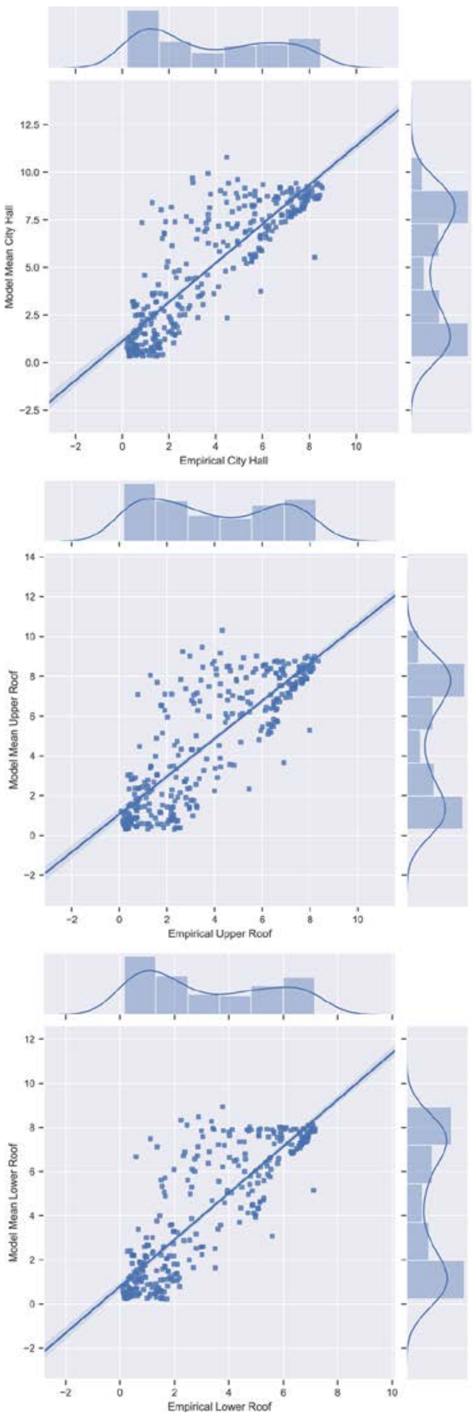

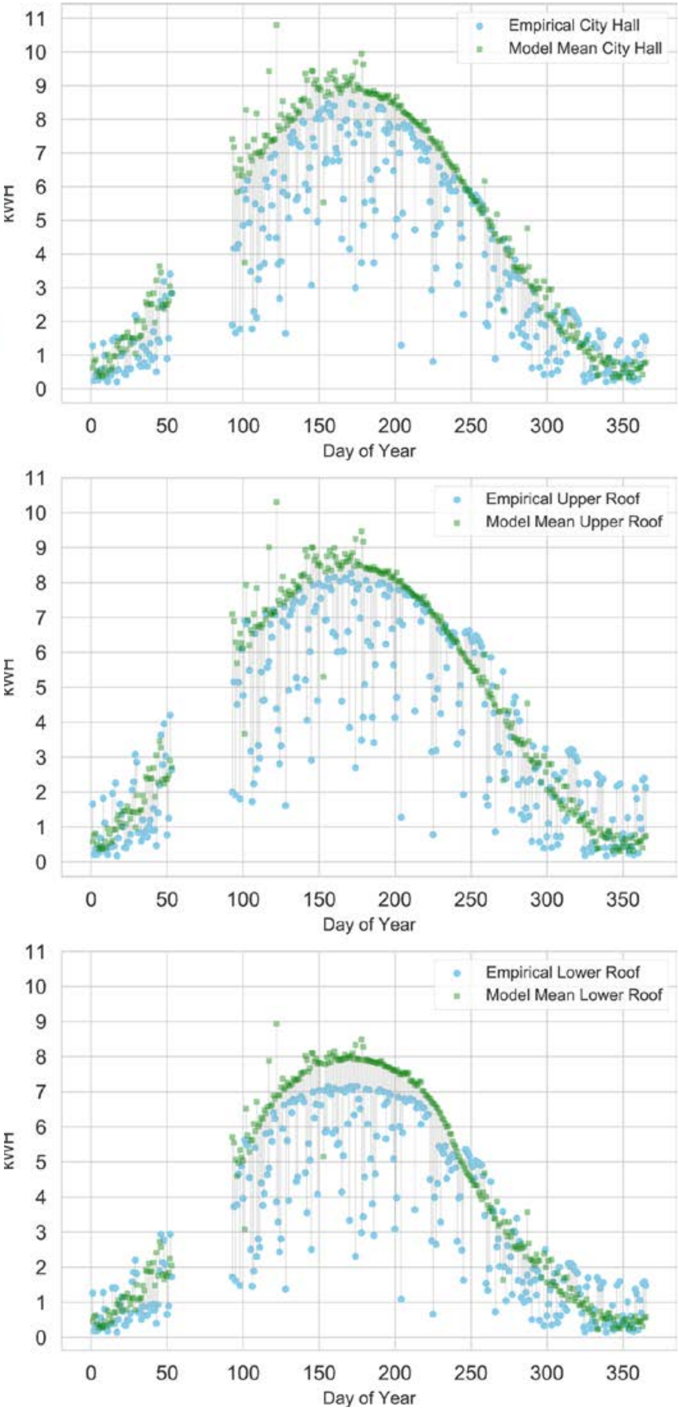

Figure 29 - Marginal plots comparing empirical and modelled annual kWh between all study sites.

Figure 3030 - Lollipop plots comparing empirical and modelled annual kWh between all study sites as a function of day of year.

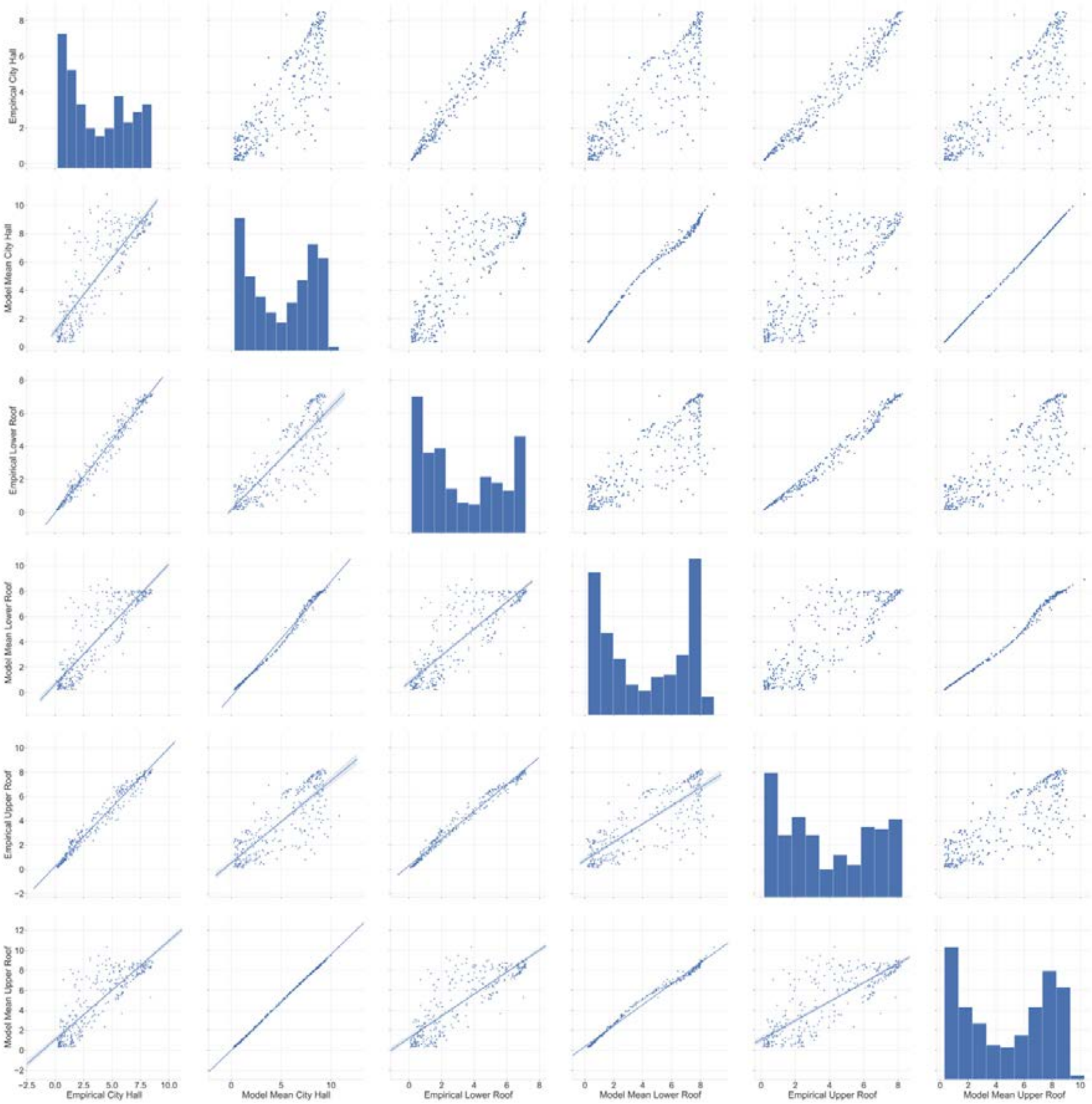

Figure 31 – Pairwise plot of annual relationships between all empirical and modelled datasets at all sites.

Chapter 4: Discussion

LiDAR

Characterizing the LiDAR used to generate the input DSM for the solar model employed a combination of in-house macros and hand classification. Particular challenges presented themselves while classifying points at the interface of the built and natural environments. Macros were sufficiently accurate at identifying roof planes and edges in the absence of vegetation overhanging them, though certainly not reliant enough when vegetation *was* present. A significant threat to the representativeness of the classified points was errant or mis-classified data. Though extremely laborious, the hand classification approach provided the oversight necessary to ensure such errors were not incorporated in the generation of the DSM representing the urban canopy layer. As discussed, the ramifications of any such data being used in the creation of the DSM can significantly mis-represent the generated surface. In the context of providing high-quality, high-resolution solar mapping assessments in areas of complex urban morphology, introducing non-existent occluding surfaces can be detrimental to the overall goal. Thus, methods for generating the DSM are an important backstop for safeguarding final results from succumbing to such errors.

DSM

Methods employed in this research for generating the DSM were qualitative, and could have benefitted from a more robust approach. That said, the results in the test insolation layers generated with the different DSM interpolation methods suggest that the chosen inverse distance weighted and nearest neighbour method did provide the most representative outcome when considering roof edge, chimney, and sunroof cases amongst them. Nonetheless, it was important to realize that the typical approach of using the maximum point value to represent a raster cell is not appropriate when using the generated surface for urban solar modelling.

Atmospheric Clearness

This research employed a data-driven approach to deriving atmospheric parameters used in the solar model. Not every city will have such an opportunity to draw from a uniquely dense network, as this research was able to. Regardless, whether ground-based, satellite-based, or meteorological, a long-term nearby source of surface radiation measurements is key to ensuring representativeness of derived atmospheric clearness indices. Long-term is key, and in this case the solar climatology that informed the annual daily K_t values was a best-case scenario. The importance of a long-term dataset is illustrated in the stationarity of the modelled insolation results versus the empirical insolation measurements (Figure 30) where stochastic processes dominated consistency throughout the year. When assessing the annual daily clearness indices derived from the solar climatology a stationary signal is more defined (Figure 16), and would theoretically improve if the climatology were closer to a typical 30-year set.

Diffuse Fraction

The applicability of the standard models presented in Jacovides et al. (2006) to deriving daily diffuse fraction for Victoria was tested, with particular focus on seasonal and model-specific analysis. It was found that clear seasonal trends exist between the models, and that the models similarly predict daily diffuse with some minor exceptions regarding seasonal model bias and extreme value generation. Specifically, Erbs et al. (Equation 15) and Boland et al. (Equation 11) were shown to disproportionally predict extreme K_d values compared to the means of the standard models, with Erbs et al. (Equation 15) overestimating in the seasons with lower K_t values (fall/winter) and Boland et al. (Equation 11) underestimating in the seasons with higher K_t values (spring/summer).

Given the latitude of Victoria compared to the diverse set of locations where the empirical data for the standard models was derived, it is reasonable to conclude that the standard models are indeed, as Jacovides et al. (2006) claim, location-independent, and that their use should consider seasonality as models are shown to have seasonal dependencies that can lead to biased K_d results. That said, the Orgill and Hollands

(Equation 9) model that was employed in the Solar Analyst tool does not exhibit any extreme value bias compared to the others, and the noted slight (~ 5.2%) overestimation of K_d values compared to the other standard models will ensure conservativeness in the prediction of rooftop solar potential throughout Victoria. Future work regarding the diffuse fraction could include deriving a model from the standard mean dataset to ensure computed results are based on the mean of what is considered to be the standard models. This could allow for more average, thus less extreme bias, in derived K_d results. Ultimately, having a diffuse fraction dataset to compare models results to would be ideal.

Solar Analyst

The crux of this study was employing the Solar Analyst model with the representatively-derived input DSM and atmospheric parameters to provide high-spatiotemporal resolution solar resource maps for the city of Victoria. The model was executed 365 times to produce daily insolation maps and returned 359 sets instead. Tests using different atmospheric parameters resulted in some runs (days 101, 153, 271, and 334) successfully executing, but in the end two days (88 and 333) were unable to complete no matter what default, slightly altered, or standard model generated K_d value was used. Because some of the above changes did lead to the model successfully executing after the first failed attempt, it is possible that atmospheric parameters play an integral role in the Solar Analyst tool's ability to render insolation results. If the case were that the K_t or K_d values first used were outside the acceptable parameters for the model's calculations to complete, then the second set used should not have worked, and five did. However, being that two days simply could not complete, even using the default parameters, it could be the case that the only other input layer (the DSM), in combination with the atmospheric parameters (and other model parameters), was prohibiting Solar Analyst from completing the run. This is not able to be determined for certain, however, until all other possible combinations of K_t and $K_d$values were attempted. These issues could also be due to the limits of the Solar Analyst model being pushed beyond their intended use. Though the authors (Fu and Rich) have declared the tool suitable for building scale analyses, they've also suggested its intended use is strictly for landscape-scale solar radiation assessments.

Regardless, Solar Analyst is commonly used for such large-scale, high-resolution solar resource assessments, so exploring its functional boundaries is useful and may provide others valuable information in their own exploration of the tool's limits. Without unpacking the inner workings of the model to assess whether or not a divide by zero error, for example, is occurring in this high-resolution application of it, one can only theorize.

Processing

In order to expedite computation of the model, multiprocessing of the geoprocessing script was employed. Reductions in processing time were not linearly related to the # of threads used in each pool, but were close. On average, a set of 12 model runs took ~ 21 hours to complete, rendering total processing time for all runs to ~ 27 days, and not the ~ 254 days it would have taken without a parallel processing approach. At the time of this study, and to the knowledge of the author, this approach is a novel application of parallel processing to the execution of the Solar Analyst tool.

Results

Overall, the integrated methods and corresponding data of the methodology were derived and applied in such a way as to ensure maximum accuracy and precision as possible between them. All data were upscaled, not downscaled, to be as representative of either the surface or atmospheric characteristics of the area. Data were transformed to be the same scale as one another, so as to minimize any uncertainty or error compounding when integrated within the model. Results between modelled and empirical data show large, positive correlations. As discussed, the stationarity of modelled daily insolation through the year manifests in a relatively clear parabolic trend, while the empirical curve exhibits dominance from stochastic variables throughout the year. Presumably, most of the variance within the empirical set is largely due to clouds, though some attenuation could also be attributed to 2014 being the 3rd highest amount of hectares burned in wildfires in the province's history (Province of British Columbia, 2014). Regardless, the non-stationarity is apparent; though underscored by a resolvable parabolic trend akin to the modelled dataset. Interesting that the Lower sensor of study site #1 correlated higher than the Upper, as it is in the lee of the evergreen coniferous trees south of the property, and the Upper sensor does not experience this shading. The highest correlation was City Hall, and its modelled data tended to stray less from its empirical in the winter. A seasonal correlation would be beneficial to further comment on such trends.

Climate Action

The monthly and annual insolation datasets generated from this research are providing the foundational data for translation into practical information regarding the best location to install PV on a rooftop, sizing considerations, power generation capabilities, costs/savings, and amount of GHGs abated (Figure 32). This value-added service is being provided through the City of Victoria’s website, and is currently in the beta-testing phase with a launch planned this winter.

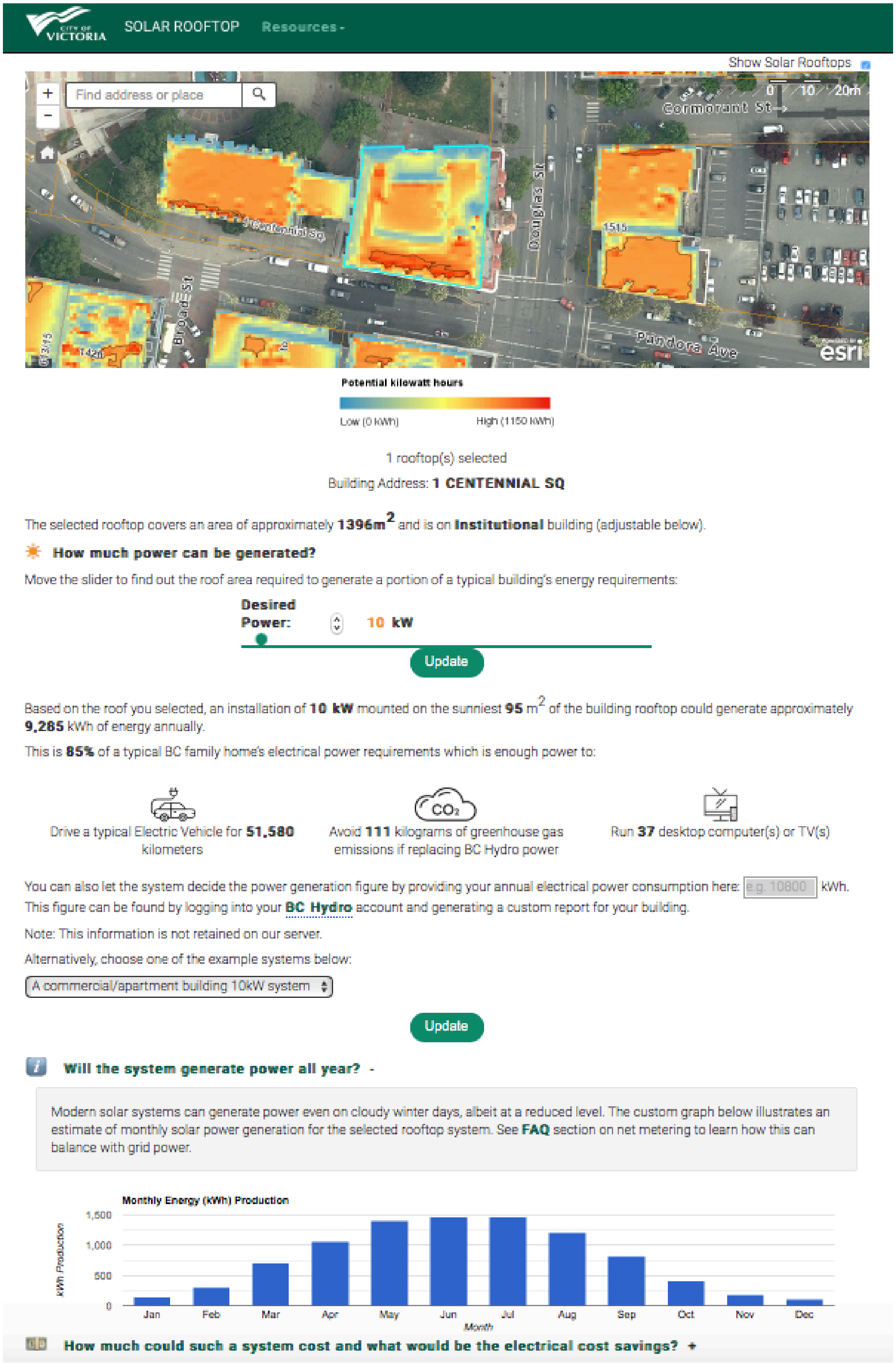

1 rooftop(s) selected

Building Address: **1 CENTENNIAL SQ**

The selected rooftop covers an area of approximately **1396m^2** and is on **Institutional** building (adjustable below).

How much power can be generated?

Move the slider to find out the roof area required to generate a portion of a typical building's energy requirements:

Based on the roof you selected, an installation of **10 kW** mounted on the sunniest **95** m^2 of the building rooftop could generate approximately **9,285** kWh of energy annually.

This is **85%** of a typical BC family home's electrical power requirements which is enough power to:

Drive a typical Electric Vehicle for **51,580** kilometers

Avoid **111** kilograms of greenhouse gas emissions if replacing BC Hydro power

Run **37** desktop computer(s) or TV(s)

You can also let the system decide the power generation figure by providing your annual electrical power consumption here: e.g. 10800 kWh.

This figure can be found by logging into your **BC Hydro** account and generating a custom report for your building.

Note: This information is not retained on our server.

Alternatively, choose one of the example systems below:

Will the system generate power all year? -

Modern solar systems can generate power even on cloudy winter days, albeit at a reduced level. The custom graph below illustrates an estimate of monthly solar power generation for the selected rooftop system. See **FAQ** section on net metering to learn how this can balance with grid power.

How much could such a system cost and what would be the electrical cost savings? +

Figure 32 – City of Victoria solar tool (beta) employing insolation data from this research.

Chapter 5: Conclusion

To facilitate climate action related to reducing GHG emissions in Victoria's building stock, the generation of high-quality, high-resolution maps of rooftop solar potential throughout the city was the primary purpose of this research. It was achieved by applying the findings from a comprehensive review of modelling solar radiation at the Earth surface to constructing a corresponding methodology, and executing its integrated models with available data in ways that ensure the representation of factors determining local insolation is with high fidelity.

In particular, special attention was paid to ensuring integrated models pass data to the next at similar scales and suitability, so as to minimize any compounding of errors and uncertainty between them. Atmospheric parameters used as input to the Solar Analyst model were derived from a ~10-year solar climatology built from a dense network of ground-based measurements, and upscaled to a set of annual daily averages. This set was used to test the biases and location / seasonal dependence of the standard models for deriving diffuse fraction, ensuring suitability of the model choice. It was shown that the global-to-diffuse model used (Orgill and Hollands - Equation 9) was appropriate for the location and exhibited a tendency to predict diffuse fractions that lead towards more conservative estimates of insolation in the fall and winter. Models were executed using scripting approaches where possible for consistency and automation purposes. The Solar Analyst model was executed using a novel multiprocessing approach that leveraged parallel processing to significantly reduce computation time from approximately 6096 to 648 hours (or 254 to 27 days). The result was a set of maps with daily insolation resolved for every 1m^2 of Victoria's ~20km^2 extent. Analysis showed these data correlate strongly with empirical measurements taken at three separate locations.

Thus, this research culminates as it intended – providing solar radiation data suitable for a high-quality, high-resolution solar mapping assessment of Victoria's rooftops, to facilitate climate action related to its built environment.

Bibliography

Abbot, C. G., Fowle, F. R., & Aldrich, L. B. (1913). The Variation of the Sun. *American Astronomical Society*, *38*, 181–186. https://doi.org/10.1360/zd-2013-43-6-1064

Acres Consulting Services Ltd., Solar Applications and Research Ltd., & Hay, J. E. (1980). *Solar energy resource assessment study for British Columbia, Volume 1: Main report*. Vancouver: BC Ministry of Energy, Mines and Petroleum Resources.

Akbari, H. (2002). Shade trees reduce building energy use and CO2 emissions from power plants. *Environmental Pollution (Barking, Essex : 1987)*, *116 Suppl*, S119-26. Retrieved from http://www.ncbi.nlm.nih.gov/pubmed/11833899

Akbari, Hashem, & Konopacki, S. (2004). Energy effects of heat-island reduction strategies in Toronto, Canada. *Energy*, Vol. 29, pp. 191–210. https://doi.org/10.1016/j.energy.2003.09.004

Alsamamra, H., Ruiz-Arias, J. A., Pozo-Vázquez, D., & Tovar-Pescador, J. (2009). A comparative study of ordinary and residual kriging techniques for mapping global solar radiation over southern Spain. *Agricultural and Forest Meteorology*, *149*(8), 1343–1357. https://doi.org/10.1016/j.agrformet.2009.03.005

American Meterological Society. (2019). Urban Canopyitle.

Ångström, A. (1924). SOLAR AND TERRESTRIAL RADIATION. *Monthly Weather Review*, *52*(8), 397. https://doi.org/10.1175/1520-0493(1924)52<397:SATR>2.0.CO;2

ArcGIS. (2019). What is Empirical Bayesian kriging? Retrieved August 8, 2019, from https://pro.arcgis.com/en/pro-app/help/analysis/geostatistical-analyst/what-is-empirical-bayesian-kriging-.htm

B.C. Climate Action Charter. , Province of British Columbia § (2007).

Badescu, V. (2008a). Ch 13 - Use of Sunshine Number for Solar Irradiance. In *Modeling Solar Radiation at the Earth's Surface: Recent Advances*. Retrieved from http://ezproxy.library.uvic.ca/login?url=http://dx.doi.org/10.1007/978-3-540-77455-6

Badescu, V. (2008b). *Modeling solar radiation at the earth's surface: recent advances*. Berlin: Springer.

Basu, S., & Antia, H. M. (2008). Helioseismology and solar abundances. *Physics Reports*, *457*(5–6), 217–283. https://doi.org/10.1016/j.physrep.2007.12.002

Batlles, F. J., Bosch, J. L., Tovar-Pescador, J., Martínez-Durbán, M., Ortega, R., & Miralles, I. (2008). Determination of atmospheric parameters to estimate global radiation in areas of complex topography: Generation of global irradiation map. *Energy Conversion and Management*, *49*(2), 336–345. https://doi.org/10.1016/j.enconman.2007.06.012

Beyer, H.G., Czeplak, G., Terzenbach, U., & Wald, L. (1997). Assessement of the method used to construct clearness index maps for the new European Solar Radiation Atlas ESRA. *Solar Energy*, *6*(61), 389–397. Retrieved from http://onlinelibrary.wiley.com/doi/10.1002/cbdv.200490137/abstract

Beyer, Hans Georg, Czeplak, G., Terzenbach, U., & Wald, L. (1997). Assessment of the method used to construct clearness index maps for the new European Solar Radiation Atlas (ESRA). *Solar Energy*, *61*(6), 389–397. https://doi.org/http://dx.doi.org/10.1016/S0038-092X(97)00084-4

Boland, J., Scott, L., & Luther, M. (2001). Modelling the diffuse fraction of global solar radiation on a horizontal surface. *Environmetrics*, *12*(2), 103–116. https://doi.org/10.1002/1099-095X(200103)12:2<103::AID-ENV447>3.0.CO;2-2

Bonan, G. B. (2016). *Ecological climatology: concepts and applications* (Third). Third. Retrieved from http://uvic.summon.serialssolutions.com/2.0.0/link/0/eLvHCXMwdV3BDoIwDG0UPXhTkaio4QcwwAZjVw3EgxcT74QxlpgYPfv3djiiEj2uh2ZrmrV9Xd8ASLQN_M6dwNFtkpLHLJSsxDK7FIGgdYJFtCIi5PJ7mgxaVoguc6IZPPnfnyGUUUxg-pgoBfqBHzkd34hLzHUbr_kuCB2dEsZSQ_rUroMP7k8TYvIxWHrsYAK9-jaF4e

Bonanno, A., Schlattl, H., & Paterno, L. (2002). *The age of the Sun and the relativistic corrections in the EOS*. (0), 3–6. https://doi.org/10.1051/0004-6361:20020749

Brandtberg, T. (2007). Classifying individual tree species under leaf-off and leaf-on conditions using airborne lidar. *ISPRS Journal of Photogrammetry and Remote Sensing*, *61*(5), 325–340.

Brito, M. C., Gomes, N., Santos, T., & Tenedório, J. A. (2012). Photovoltaic potential in a Lisbon suburb using LiDAR data. *Solar Energy*, *86*(1), 283–288.

Cano, D., Monget, J., Albuisson, M., & Guillard, H. (1986). A method for the determination of the global solar radiation from meteorological satellite data. *Solar Energy*, *37*(1), 31–39. Retrieved from http://www.sciencedirect.com/science/article/pii/0038092X86901040

Chandrasekaran, J., & Kumar, S. (1994). Hourly diffuse fraction correlation at a tropical location. *Solar Energy*, *53*(6), 505–510. https://doi.org/10.1016/0038-092X(94)90130-T

Chow, A., Fung, A., & Li, S. (2014). GIS Modeling of Solar Neighborhood Potential at a Fine Spatiotemporal Resolution. *Buildings*, *4*(2), 195–206. https://doi.org/10.3390/buildings4020195

Christen, A., & Vogt, R. (2004). Energy and radiation balance of a central European city. *International Journal of Climatology*, *24*(11), 1395–1421. https://doi.org/10.1002/joc.1074

City of Victoria. (2013). City of Victoria Urban Forest Master Plan. *Journal of Forestry*, (February), 1–98.

City of Victoria. (2018). Climate Leadership Plan. In *Victoria*.

Climate Change Accountability Act. , Pub. L. No. c 42, SBC (2007).

Cui, Y., Xie, J., Liu, J., Wang, J., & Chen, S. (2017). A review on phase change material application in building. *Advances in Mechanical Engineering*, *9*(6), 168781401770082. https://doi.org/10.1177/1687814017700828

Czekalski, D., Chochowski, a., Obstawski, P., Liu, B. Y. H., Jordan, R. C., Rao, C. R. N., … Mora, C. (2012). Ch 8 - Models of Diffuse Solar Fraction. *Solar Energy*, *4*(5), 2492–2504. https://doi.org/10.1016/0038-092X(60)90062-1

Davis Intruments. (2013). *Solar radiation sensor; Vantage Pro2 Accessories*.

Eddington, A. S. (1926). *The internal constitution of the stars*. Cambridge University Press.

Environment and Climate Change Canada. (2016). *Pan-Canadian Framework on Clean Growth and Climate Change : Canada's plan to address climate change and grow the economy*. Environment and Climate Change Canada.

Erbs, D. G., Klein, S. A., & Duffie, J. A. (1982). Estimation of the diffuse radiation fraction for hourly, daily and monthly-average global radiation. *Solar Energy*, *28*(4), 293–302. https://doi.org/10.1016/0038-092X(82)90302-4

Fu, P., & Rich, P. M. (1999). Design and Implementation of the Solar Analyst: an ArcView Extension for Modeling Solar Radiation at Landscape Scales. *19th Annual ESRI User Conference*, (February), 1–24.

Fu, P., & Rich, P. M. (2000). *The Solar Analyst 1 .0 User Manual*.

Fu, P., & Rich, P. M. (2003). A geometric solar radiation model with applications in agriculture and forestry. *Computers and Electronics in Agriculture*, *37*(1–3), 25–35. https://doi.org/10.1016/S0168-1699(02)00115-1

Giesen, J. (2018). Eccentricity of the orbit of the Earth from 1,000,000 BC to 1,000,000 AD. Retrieved February 17, 2019, from http://www.jgiesen.de/kepler/eccentricity1.html

Gilani, S. A. N., Awrangjeb, M., & Lu, G. (2018). Segmentation of airborne point cloud data for automatic building roof extraction. *GIScience and Remote Sensing*, *55*(1), 63–89. https://doi.org/10.1080/15481603.2017.1361509

Givoni, B. (1989). *Urban Design in Different Climates*. Retrieved from https://books.google.ca/books?id=aAPcOwAACAAJ

Goodwin, N. R., Coops, N. C., Tooke, T. R., Christen, A., & Voogt, J. A. (2009). Characterizing urban surface cover and structure with airborne lidar technology. *Canadian Journal of Remote Sensing, 35*(3), 297–309. Retrieved from http://dx.doi.org/10.5589/m09-015

Gordon, J. M., & Reddy, T. A. (1988). Time series analysis of hourly global horizontal solar radiation. *Solar Energy*, *41*(5), 423–429. https://doi.org/10.1016/0038-092X(88)90016-3

Gueymard, C. A. (2004). The sun’s total and spectral irradiance for solar energy applications and solar radiation models. *Solar Energy*, *76*(4), 423–453.

Gueymard, C. A. (2012). Clear-sky irradiance predictions for solar resource mapping and large-scale applications: Improved validation methodology and detailed performance analysis of 18 broadband radiative models. *Solar Energy*, *86*(8), 2145–2169. https://doi.org/10.1016/j.solener.2011.11.011

Gueymard, C. A., & Myers, D. R. (2008a). Ch 1 - Solar Radiation Measurement : Progress in Radiometry for Improved Modeling. In *Modeling Solar Radiation at the*

Earth's Surface: Recent Advances (pp. 1–27).

Gueymard, C. A., & Myers, D. R. (2008b). Ch 20 - Validation and Ranking Methodologies for Solar Radiation Models. In *Modeling Solar Radiation at the Earth's Surface: Recent Advances*.

Gurtuna, O., & Prevot, A. (2011). An overview of solar resource assessment using meteorological satellite data. *Proceedings of 5th International Conference on Recent Advances in Space Technologies - RAST2011*, 209–212. https://doi.org/10.1109/RAST.2011.5966825

Hammer, A., Heinemann, D., Hoyer, C., Kuhlemann, R., Lorenz, E., Müller, R., & Beyer, H. G. (2003). Solar energy assessment using remote sensing technologies. *Remote Sensing of Environment*, *86*(3), 423–432. https://doi.org/10.1016/S0034-4257(03)00083-X

Hancock, P. L. (2000). The Oxford Companion to the Earth. In *Oxford companion to the earth*. Oxford University Press.

Hathaway, D. H. (2010). The Solar Cycle. *Living Reviews in Solar Physics*, *7*(1), 5–65. https://doi.org/10.1007/lrsp-2015-4

Hawlader, M. N. (1984). Diffuse, global and extra-terrestrial solar radiation for Singapore. *International Journal of Ambient Energy*, *5*(1), 31–38. https://doi.org/10.1080/01430750.1984.9675406

Hay, J. E. (1986). Errors associated with the spatial interpolation of mean solar irradiances. *Solar Energy*, *37*(2), 135–146. https://doi.org/10.1016/0038-092X(86)90071-X

Hays, J. D., Imbrie, J., & Shackleton, N. J. (1976). Variations in the Earth's Orbit : Pacemaker of the Ice Ages. *Science*, *194*(194), 1121–1132.

Heisler, G. M. (1986). Effects of individual trees on the solar radiation climate of small buildings . *Urban Ecology* , Vol. 9, pp. 337–359. https://doi.org/10.1016/0304-4009(86)90008-2

Hofierka, J., & Kaňuk, J. (2009). Assessment of photovoltaic potential in urban areas using open-source solar radiation tools. *Renewable Energy*, *34*(10), 2206–2214.

Hofierka, J., & Suri, M. (2002). The solar radiation model for open source GIS: implementation and applications. *Proceedings of the Open Source GIS - GRASS*

Users Conference 2002.

Höfle, B., Hollaus, M., & Hagenauer, J. (2012). Urban vegetation detection using radiometrically calibrated small-footprint full-waveform airborne LiDAR data. *ISPRS Journal of Photogrammetry and Remote Sensing*, *67*(0), 134–147. https://doi.org/10.1016/j.isprsjprs.2011.12.003

Hollands, K. G. T., & Huget, R. G. (1983). A probability density function for the clearness index, with applications. *Solar Energy*, *30*(3), 195–209. https://doi.org/10.1016/0038-092X(83)90149-4

Hung, C. L. J., James, L. A., & Hodgson, M. E. (2018). An automated algorithm for mapping building impervious areas from airborne LiDAR point-cloud data for flood hydrology. *GIScience and Remote Sensing*, *55*(6), 793–816. https://doi.org/10.1080/15481603.2018.1452588

Ineichen, P., & Perez, R. (2002). A new airmass independent formulation for the Linke turbidity coefficient. *Solar Energy*, *73*(3), 151–157. https://doi.org/10.1016/S0038-092X(02)00045-2

IPCC. (2019). Summary for Policymakers of IPCC Special Report on Global Warming of 1.5°C approved by governments — IPCC. Retrieved August 13, 2019, from https://www.ipcc.ch/2018/10/08/summary-for-policymakers-of-ipcc-special-report-on-global-warming-of-1-5c-approved-by-governments/

Iqbal, M. (1983). An Introduction to Solar Radiation. In *Academic Press Canada*. https://doi.org/10.1177/002248715600700402

Izquierdo, S., Rodrigues, M., & Fueyo, N. (2008). A method for estimating the geographical distribution of the available roof surface area for large-scale photovoltaic energy-potential evaluations. *Solar Energy*, *82*(10), 929–939. https://doi.org/10.1016/j.solener.2008.03.007

Jacovides, C. P., Tymvios, F. S., Assimakopoulos, V. D., & Kaltsounides, N. a. (2006). Comparative study of various correlations in estimating hourly diffuse fraction of global solar radiation. *Renewable Energy*, *31*(15), 2492–2504. https://doi.org/10.1016/j.renene.2005.11.009

Jakubiec, J. A., & Reinhart, C. F. (2012). Towards validated urban photovoltaic potential and solar radiation maps based on lidar measurements , gis data , and hourly daysim simulations. *SimBuild 2012. Fifth National Conference of IBPSA-USA Madison, Wisconsin August 1-3, 2012*, 10. https://doi.org/10.1093/intqhc/mzm043

Jakubiec, J. A., & Reinhart, C. F. (2013). A method for predicting city-wide electricity gains from photovoltaic panels based on LiDAR and GIS data combined with hourly Daysim simulations. *Solar Energy*, *93*, 127–143. https://doi.org/10.1016/j.solener.2013.03.022

Jochem, A., Höfle, B., Rutzinger, M., & Pfeifer, N. (2009). Automatic Roof Plane Detection and Analysis in Airborne Lidar Point Clouds for Solar Potential Assessment. *Sensors*, *9*(7), 5241–5262. Retrieved from http://www.mdpi.com/1424-8220/9/7/5241

Jochem, A., Höfle, B., Wichmann, V., Rutzinger, M., & Zipf, A. (2012). Area-wide roof plane segmentation in airborne LiDAR point clouds. *Computers, Environment and Urban Systems*, *36*(1), 54–64. https://doi.org/10.1016/j.compenvurbsys.2011.05.001

Jones, T. G., Coops, N. C., & Sharma, T. (2010). Assessing the utility of airborne hyperspectral and LiDAR data for species distribution mapping in the coastal Pacific Northwest, Canada. *Remote Sensing of Environment*, *114*(12), 2841–2852.

Journée, M., & Bertrand, C. (2011). Geostatistical merging of ground-based and satellite-derived data of surface solar radiation. *Advances in Science and Research*, *6*, 1–5. https://doi.org/10.5194/asr-6-1-2011

Kafka, J. L., & Miller, M. A. (2019). A climatology of solar irradiance and its controls across the United States: Implications for solar panel orientation. *Renewable Energy*, *135*, 897–907. https://doi.org/10.1016/J.RENENE.2018.12.057

Karatasou, S., Santamouri, M., & Geros, V. (2003). Analysis of experimental data on diffuse solar radiation in Athens, Greece, for building applications. *International Journal of Sustainable Energy*, *23*(1–2), 1–11. https://doi.org/10.1080/0142591031000148597

Kasten, F. (1996). The linke turbidity factor based on improved values of the integral Rayleigh optical thickness. *Solar Energy*, *56*(3), 239–244. https://doi.org/10.1016/0038-092X(95)00114-7

Kasten, F., & Young, A. T. (1989). Revised optical air mass tables and approximation formula. *Applied Optics*, *28*(22), 4735. https://doi.org/10.1364/ao.28.004735

Kim, S., Schreuder, G., McGaughey, R. J., & Andersen, H.-E. (2008, April). *Individual tree species identification using lidar intensity data*. ASPRS.

Korpela, I., Tokola, T., Orka, H. O., & Koskinen, M. (2009). Small-footprint discrete-return LIDAR in tree species recognition. *International Archives of the Photogrammetry, Remote Sensing and Spatial Information Sciences*, *XXXVIII-1-*(Hanover Workshop 2009: High-resolution Earth Imaging for Geospatial Information), October 5, 2012. Retrieved from http://isprsserv.ifp.uni-stuttgart.de/proceedings/XXXVIII-1-4-7_W5/paper/Korpela-137.pdf

Krayenhoff, E. S., & Voogt, J. A. (2010). Impacts of urban albedo increase on local air temperature at daily-annual time scales: Model results and synthesis of previous work. *Journal of Applied Meteorology and Climatology*, *49*(8), 1634–1648. https://doi.org/10.1175/2010JAMC2356.1

Kumar, A., Singh, N., Anshumali, & Solanki, R. (2018). Evaluation and utilization of MODIS and CALIPSO aerosol retrievals over a complex terrain in Himalaya. *Remote Sensing of Environment*, *206*(May 2017), 139–155. https://doi.org/10.1016/j.rse.2017.12.019

Landsberg, H. E. (1981). *The urban climate*. Retrieved from http://uvic.summon.serialssolutions.com/2.0.0/link/0/eLvHCXMwdVw9C8IwED38WNz8xG8yuSntNantLIqDDoK7JOkJgigI_n8vaSlSdMwNR77IvXvhPYAIV8Gy8iZInRAXd0JSNpChXUdGmTS2cWKkTKOKmqzk36rOiYXw5P__jBOaOCF2nWGD03OcDiXhws2GWkvpbXWQQYJzJSkceMrxl_VnUWF2bWg41UEHavTowujIUPb58o

Liang, X., Hyyppä, J., & Matikainen, L. (2007). Deciduous-coniferous tree classification using difference between first and last pulse laser signatures. *International Archives of the Photogrammetry, Remote Sensing and Spatial Information Sciences*, *XXXVI-3/W5*(ISPRS Workshop “Laser scanning 2007 and SilviLaser 2007,” in Finland), October 5, 2012.

Lindberg, F., & Grimmond, C. S. B. (2011). The influence of vegetation and building morphology on shadow patterns and mean radiant temperatures in urban areas: model development and evaluation. *Theoretical and Applied Climatology*, *105*(3–4), 311–323. https://doi.org/10.1007/s00704-010-0382-8

Linke, F. (1922). Transmissionkoeflizient und Trubungsfaktor. *Beitr. Phys. Frein Atm0s. I*, 91.

Liu, X. (2008). Airborne LiDAR for DEM generation: some critical issues. *Progress in Physical Geography*, *32*(1), 31–49. Retrieved from http://ppg.sagepub.com/content/32/1/31.abstract

Mallet, C., Soergel, U., & Bretar, F. (2008). Analysis of full-waveform lidar data for classification of urban areas. *International Archives of the Photogrammetry, Remote Sensing and Spatial Information Sciences*, *XXXVII-A*,(XXI ISPRS Congress, Commission III papers, Beijing, China), October 3, 2012.

Manni, M., Lobaccaro, G., & Goia, F. (2018). An inverse approach to identify selective angular properties of retro- re fl ective materials for urban heat island mitigation. *Solar Energy*, *176*(October), 194–210. https://doi.org/10.1016/j.solener.2018.10.003

Marion, W., & Wilcox, S. (1994). A new solar radiation data manual for flat-plate and concentrating collectors . *AIP Conference Proceedings (American Institute of Physics); (United States)* . Retrieved from http://uvic.summon.serialssolutions.com/2.0.0/link/0/eLvHCXMwtV3fS8MwEA46EXzzx0SdSvC1VJZ0SdYHH4Yo-jAQNp9Hm6UgaCez-_93l2TJpjLwwZdQstJ23x13l8t3F0IyfttNv9kEplSmcmGYUGZaZHkJXkOKqeqJXsVLpjerycI5hnHuXwUPcyB6LKT9g_DDQ2ECrkEFYAQlgPGnGvzqjQbPL2t1fa4ywN5j861hx2aDNW

Masson, V., Bonhomme, M., Salagnac, J.-L., Briottet, X., & Lemonsu, A. (2014). Solar panels reduce both global warming and urban heat island. *Frontiers in Environmental Science*, *2*. https://doi.org/10.3389/fenvs.2014.00014

McPherson, E. G., & Simpson, J. R. (2003). Potential energy savings in buildings by an urban tree planting programme in California. *Urban Forestry & Urban Greening*, *2*(2), 73–86. https://doi.org/10.1078/1618-8667-00025

Metcalfe, T. S., & van Saders, J. (2017). Magnetic Evolution and the Disappearance of Sun-Like Activity Cycles. *Solar Physics*, *292*(9), 1–12. https://doi.org/10.1007/s11207-017-1157-5

Miguel, A., Bilbao, J., Aguiar, R., Kambezidis, H., & Negro, E. (2001). Diffuse solar irradiation model evaluation in the North Mediterranean Belt area. *Solar Energy*, *70*(2), 143–153. https://doi.org/10.1016/S0038-092X(00)00135-3

Moradi, I., Mueller, R., & Perez, R. (2013). Retrieving daily global solar radiation from routine climate variables. *Theoretical and Applied Climatology*, *116*(3–4), 661–669. https://doi.org/10.1007/s00704-013-0979-9

Mueller, R. W., Dagestad, K. F., Ineichen, P., Schroedter-Homscheidt, M., Cros, S., Dumortier, D., … Heinemann, D. (2004). Rethinking satellite-based solar irradiance modelling: The SOLIS clear-sky module. *Remote Sensing of Environment*, *91*(2), 160–174. https://doi.org/10.1016/j.rse.2004.02.009

NASA, E. (2015). SOHO - Solar and Heliospheric Observatory. Retrieved February 13, 2019, from https://www.nasa.gov/mission_pages/soho/index.html

National Research Council. (1982). *Solar variability, weather, and climate*. 7. Retrieved from http://voyager.library.uvic.ca/vwebv/exportRecord.do

National Research Council. (2013). Understanding the changing planet: strategic directions for the geographical sciences. In *The National Academies Press* (Vol. 48). https://doi.org/10.5860/choice.48-2698

Nguyen, H. T., & Pearce, J. M. (2010). Estimating potential photovoltaic yield with r.sun and the open source Geographical Resources Analysis Support System. *Solar Energy*, *84*(5), 831–843. https://doi.org/10.1016/j.solener.2010.02.009

NREL. (2017). *Solar Position Algorithm SPA*. (January). Retrieved from https://www.nrel.gov/midc/spa/%0Ahttps://midcdmz.nrel.gov/solpos/spa.html

Oke, T. R., Crowther, J. M., McNaughton, K. G., Monteith, J. L., & Gardiner, B. (1989). The Micrometeorology of the Urban Forest [and Discussion] . *Philosophical Transactions of the Royal Society of London. B, Biological Sciences* , Vol. 324, pp. 335–349. https://doi.org/10.1098/rstb.1989.0051

Oke, T. R., Johnson, G. T., Steyn, D. G., & Watson, I. D. (1991). Simulation of surface urban heat islands under ‘ideal’ conditions at night part 2: Diagnosis of causation. *Boundary-Layer Meteorology*, *56*(4), 339–358. https://doi.org/10.1007/BF00119211

Oliveira, A. P., Escobedo, J. F., Machado, A. J., & Soares, J. (2002). Correlation models of diffuse solar-radiation applied to the city of São Paulo, Brazil. *Applied Energy*, *71*(1), 59–73. https://doi.org/10.1016/S0306-2619(01)00040-X

Orgill, J. F., & Hollands, K. G. T. (1977). Correlation equation for hourly diffuse radiation on a horizontal surface. *Solar Energy*, *19*(4), 357–359. https://doi.org/10.1016/0038-092X(77)90006-8

Ouma, Y. O. (2016). Advancements in medium and high resolution Earth observation for land-surface imaging: Evolutions, future trends and contributions to sustainable development. *Advances in Space Research*, *57*(1), 110–126. https://doi.org/10.1016/j.asr.2015.10.038

Paulescu, M. (2008). Ch 7 - Solar Irradiation via Air Temperature Data. In *Modeling Solar Radiation at the Earth's Surface: Recent Advances*.

Paulescu, M., Paulescu, E., Gravila, P., & Badescu, V. (2013). Weather Modeling and Forecasting of PV Systems Operation. *Green Energy and Technology*, *103*. https://doi.org/10.1007/978-1-4471-4649-0

Power, H. C. (2003). The geography and climatology of aerosols. *Progress in Physical Geography*, *27*(4), 502–547. https://doi.org/10.1191/0309133303pp393ra

Province of British Columbia. (2014). Wildfire Season Summary - Province of British Columbia. Retrieved August 14, 2019, from https://www2.gov.bc.ca/gov/content/safety/wildfire-status/about-bcws/wildfire-history/wildfire-season-summary

Quante, M. (2009). *Solar radiation and clouds –*.

Radhi, H., Sharples, S., & Assem, E. (2015). Impact of urban heat islands on the thermal comfort and cooling energy demand of artificial islands - A case study of AMWAJ Islands in Bahrain. *Sustainable Cities and Society*, *19*, 310–318. https://doi.org/10.1016/j.scs.2015.07.017

Ratti, C., Baker, N., & Steemers, K. (2005). Energy consumption and urban texture. *Energy and Buildings*, *37*(7), 762–776. https://doi.org/10.1016/j.enbuild.2004.10.010

Reindl, D. T., Beckman, W. A., & Duffle, J. A. (1990). *Diffuse fraction correlations*. (I).

Reitberger, J., Krzystek, P., & Stilla, U. (2008). Analysis of full waveform LIDAR data for the classification of deciduous and coniferous trees. *International Journal of Remote Sensing*, *29*(5), 1407–1431. Retrieved from http://dx.doi.org.ezproxy.library.uvic.ca/10.1080/01431160701736448

Remund, J., Wald, L., Lefevre, M., & Ranchin, T. (2003). Worldwide Linke turbidity information. … *of ISES Solar World …*, 16–19. Retrieved from http://hal.archives-ouvertes.fr/hal-00465791/

Rich, P. M., Dubayah, R., Hetrick, W. A., & Saving, S. C. (1994). Using Viewshed Models to Calculate Intercepted Solar Radiation: Applications in Ecology. *American Society for Photogrammetry and Remote Sensing Technical Papers*, 524–529.

Rich, Paul M, & Fu, P. (2000). Topoclimatic Habitat Models. *4th International Conference on Integrating GIS and Environmental Modeling (GIS/EM4): Problems, Prospects and Research Needs*, (96), 1–14. Retrieved from https://pdfs.semanticscholar.org/4238/e62e99a75a3fccdf215d5513a2dcba944ede.pdf

Rigollier, C., Lefèvre, M., & Wald, L. (2004). The method Heliosat-2 for deriving shortwave solar radiation from satellite images. *Solar Energy*, *77*(2), 159–169. https://doi.org/10.1016/j.solener.2004.04.017

Robinson, D., & Stone, A. (2004). Solar radiation modelling in the urban context. *Solar Energy*, *77*(3), 295–309. https://doi.org/10.1016/j.solener.2004.05.010

Rossow, W. B., & Schiffer, R. A. (1999). Advances in Understanding Clouds from ISCCP. *Bulletin of the American Meteorological Society*, *80*(11), 2261–2288. https://doi.org/10.1175/1520-0477(1999)080<2261:AIUCFI>2.0.CO;2

Rottensteiner, F., Trinder, J., Clode, S., & Kubik, K. (2007). Building detection by fusion of airborne laser scanner data and multi-spectral images: Performance evaluation and sensitivity analysis. *ISPRS Journal of Photogrammetry and Remote Sensing*, *62*(2), 135–149. https://doi.org/10.1016/j.isprsjprs.2007.03.001

Rutzinger, M., Höfle, B., Hollaus, M., & Pfeifer, N. (2008). Object-Based Point Cloud Analysis of Full-Waveform Airborne Laser Scanning Data for Urban Vegetation Classification. *Sensors*, *8*(8), 4505–4528. Retrieved from http://www.mdpi.com/1424-8220/8/8/4505

Sadr, K. (2016). A Comparison of Accuracy and Precision in Remote Sensing Stone-walled Structures with Google Earth, High Resolution Aerial Photography and LiDAR; a Case Study from the South African Iron Age. *Archaeological Prospection*, *23*(2), 95–104. https://doi.org/10.1002/arp

Sailor, D. J. (2010). Simulated Urban Climate Response to Modifications in Surface Albedo and Vegetative Cover. *Journal of Applied Meteorology*, Vol. 34, pp. 1694–

1704. https://doi.org/10.1175/1520-0450-34.7.1694

Santamouris, M. (2018). *Minimizing Energy Consumption, Energy Poverty and Global and Local Climate Change in the Built Environment: Innovating to Zero*. Elsevier.

Schüepp, W. (1949). *Die Bestimmung der Komponenten der atmosphärischen Trübung aus Aktinometermessungen.* Universität Basel.

Secord, J., & Zakhor, A. (2007). *Tree Detection in Urban Regions Using Aerial Lidar and Image Data*. *4*(2), 196–200.

Şen, Z., & Şahin, A. D. (2001). Spatial interpolation and estimation of solar irradiation by cumulative semivariograms. *Solar Energy*, *71*(1), 11–21. https://doi.org/10.1016/S0038-092X(01)00009-3

Sengupta, M., Kurtz, S., Dobos, A., Wilbert, S., Lorenz, E., Renné, D., … Perez, R. (2015). *Best Practices Handbook for the Collection and Use of Solar Resource Data for Solar Energy Applications*. (February), 1–236. https://doi.org/10.18777/ieashc-task46-2015-0001

Shashua-Bar, L., & Hoffman, M. E. (2003). Geometry and orientation aspects in passive cooling of canyon streets with trees . *Energy & Buildings* , Vol. 35, pp. 61–68. https://doi.org/10.1016/S0378-7788(02)00080-4

Simpson, J. R. (2002). Improved estimates of tree-shade effects on residential energy use. *Energy and Buildings*, *34*(10), 1067–1076. https://doi.org/10.1016/S0378-7788(02)00028-2

Soares, J., Oliveira, A. P., Božnar, M. Z., Mlakar, P., Escobedo, J. F., & Machado, A. J. (2004). Modeling hourly diffuse solar-radiation in the city of São Paulo using a neural-network technique. *Applied Energy*, *79*(2), 201–214. https://doi.org/10.1016/j.apenergy.2003.11.004

Stephens, G. L., Vane, D. G., Boain, R. J., Mace, G. G., Sassen, K., Wang, Z., … CloudSat Science Team, T. (2002). the Cloudsat Mission and the a-Train. *Bulletin of the American Meteorological Society*, *83*(12), 1771–1790. https://doi.org/10.1175/BAMS-83-12-1771

Stewart, J. Q., & MacCracken, C. D. (1940). The General Illumination during a Total Solar Eclipse. *The Astrophysical Journal*, *91*, 51. https://doi.org/10.1086/144146

Ŝúri, M., & Hofierka, J. (2004). A new GIS-based solar radiation model and its application to photovoltaic assessments. *Transactions in GIS*, *8*(2), 175–190. https://doi.org/10.1111/j.1467-9671.2004.00174.x

Tomson, T., Russak, V., & Kallis, A. (2008). Ch 10 - Dynamic Behavior of Solar Radiation. In *Modeling Solar Radiation at the Earth's Surface: Recent Advances*.

Tooke, T. R. (2009). *REMOTE SENSING APPLICATIONS FOR VEGETATION* (Vol. 2007). University of British Columbia.

Tooke, T. R., Coops, N. C., Christen, A., Gurtuna, O., & Prévot, A. (2012). Integrated irradiance modelling in the urban environment based on remotely sensed data. *Solar Energy*, *86*(10), 2923–2934. https://doi.org/10.1016/j.solener.2012.06.026

Tooke, T. R., Coops, N. C., Voogt, J. a., & Meitner, M. J. (2011). Tree structure influences on rooftop-received solar radiation. *Landscape and Urban Planning*, *102*(2), 73–81. https://doi.org/10.1016/j.landurbplan.2011.03.011

Tovar-pescador, J. (2008). Ch 3 - Modelling the Statistical Properties of Solar Radiation and Proposal of a Technique Based on Boltzmann Statistics. In *Modeling Solar Radiation at the Earth's Surface: Recent Advances*.

Tuller, S. E. (1976). The relationship between diffuse, total and extra terrestrial solar radiation. *Solar Energy*, *18*(3), 259–263. https://doi.org/10.1016/0038-092X(76)90025-6

UCAR. (2014). Regions and Features of the Sun | UCAR Center for Science Education. Retrieved February 13, 2019, from https://scied.ucar.edu/sun-features-regions

Vaquero, J. M. (2007). Historical sunspot observations: A review. *Advances in Space Research*, *40*(7), 929–941. https://doi.org/10.1016/j.asr.2007.01.087

Versteegh, G. J. M. (2005). Solar forcing of climate. 2: Evidence from the past. *Space Science Reviews*, *120*(3–4), 243–286. https://doi.org/10.1007/s11214-005-7047-4

Voogt, J., & Oke, T. (1997). Complete urban surface temperatures. *Journal of Applied Meteorology*, 1117–1132. Retrieved from http://journals.ametsoc.org/doi/abs/10.1175/1520-0450(1997)036%3C1117%3ACUST%3E2.0.CO%3B2

Wang, K., Wang, T., & Liu, X. (2018). A review: Individual tree species classification using integrated airborne LiDAR and optical imagery with a focus on the urban environment. *Forests*, *10*(1), 1–18. https://doi.org/10.3390/f10010001

Wang, L., & Zhang, Y. (2016). *LiDAR Ground Filtering Algorithm for Urban Areas Using Scan Line Based Segmentation*. 1–14. Retrieved from http://arxiv.org/abs/1603.00912

Weaver, A. J., & Wiebe, E. C. (2006). Micro Meteorological Network in Greater Victoria Schools www.victoriaweather.ca. *CMOS Bulletin*, *34*(4), 184–190.

Webb, B. (2017). The use of urban climatology in local climate change strategies: a comparative perspective. *International Planning Studies*, *22*(2), 68–84. https://doi.org/10.1080/13563475.2016.1169916

Wen, Q., Jiang, K., Wang, W., Liu, Q., Guo, Q., Li, L., & Wang, P. (2019). Automatic building extraction from google earth images under complex backgrounds based on deep instance segmentation network. *Sensors (Switzerland)*, *19*(2). https://doi.org/10.3390/s19020333

Wiginton, L. K. K., Nguyen, H. T. T., & Pearce, J. M. M. (2010). Quantifying rooftop solar photovoltaic potential for regional renewable energy policy. *Computers, Environment and Urban Systems*, *34*(4), 345–357. https://doi.org/10.1016/j.compenvurbsys.2010.01.001

Wilby, R. L. (2008). Constructing climate change scenarios of urban heat island intensity and air quality. *Environment and Planning B: Planning and Design*, *35*(5), 902–919.

Wilks, D. S. (2006). *Statistical Methods in the Atmospheric Sciences*. Retrieved from http://books.google.com/books?id=_b4R9j2Iy7EC&pgis=1

Wilks, D. S. (2011). *Statistical Methods in the Atmospheric Sciences*. Retrieved from http://books.google.com/books?id=IJuCVtQ0ySIC&pgis=1

Williams, D. (2018). Sun Fact Sheet. Retrieved February 14, 2019, from NASA Goddard Space Flight Center website: https://nssdc.gsfc.nasa.gov/planetary/factsheet/sunfact.html

Williams, G. E. (1993). History of the Earth’s Obliquity. *Earth-Science Reviews*, *34*(1), 1–45. https://doi.org/10.1016/0301-9268(90)90006-C

Wittmann, A. D., & Xu, Z. (1988). A catalogue of sunspot obervations from 165 BC to 1684. *Vistas in Astronomy*, *31*(I), 119–145.

Wong, L. T., & Chow, W. K. (2001). Solar radiation model. *Applied Energy*, *69*, 191–224. Retrieved from http://www.physics.arizona.edu/~cronin/Solar/References/Irradiance Models and Data/WOC01.pdf

Woyte, A., Belmans, R., & Nijs, J. (2007). Fluctuations in instantaneous clearness index: Analysis and statistics. *Solar Energy*, *81*(2), 195–206. https://doi.org/10.1016/j.solener.2006.03.001

Yang, J., Kumar, M., Pyrgou, A., Chong, A., Santamouris, M., Kolokotsa, D., & Eang, S. (2018). Green and cool roofs ’ urban heat island mitigation potential in tropical climate. *Solar Energy*, *173*(February), 597–609. https://doi.org/10.1016/j.solener.2018.08.006

Young, A. T. (1980). On the Rayleigh-Scattering Optical Depth of the Atmosphere. *Journal of Applied Meteorology*, Vol. 20, pp. 328–330. https://doi.org/10.1175/1520-0450(1981)020<0328:otrsod>2.0.co;2

Yu, B., Liu, H., Wu, J., & Lin, W. M. (2009). Investigating impacts of urban morphology on spatio-temporal variations of solar radiation with airborne LIDAR data and a solar flux model: a case study of downtown Houston. *International Journal of Remote Sensing*, *30*(17), 4359–4385. Retrieved from http://ezproxy.library.uvic.ca/login?url=http://search.ebscohost.com/login.aspx?direct=true&db=a9h&AN=43840955&site=ehost-live&scope=site

Zachos, J., Pagani, M., Sloan, L., Thomas, E., Billups, K., Zachos, J., … Billups, K. (2017). *Trends , Rhythms , and Aberrations in Global Climate 65 Ma to Present*. *292*(5517), 686–693.

Zarzalejo, L. F. (2008). Ch 18 - Solar Radiation Derived from Satellite Images. In *Modeling Solar Radiation at the Earth’s Surface: Recent Advances* (pp. 449–461).

Zelenka, A., Czeplak, G., D’Agostino, V., Josefsson, W., Maxwell, E., Perez, R., … Festa, R. (1992). Techniques for supplementing solar radiation network data. In *Report IEA Task*. Retrieved from http://scholar.google.com/scholar?hl=en&btnG=Search&q=intitle:Techniques+for+supplementing+solar+radiation+network+data#0

Zelenka, A., Perez, R., Seals, R., & Renné, D. (1999). Effective accuracy of satellite-derived hourly irradiances. *Theoretical and Applied …*, *207*, 199–207. Retrieved from http://www.springerlink.com/index/82qjndwmxjhqx25a.pdf

Zölch, T., Maderspacher, J., Wamsler, C., & Pauleit, S. (2016). Using green infrastructure for urban climate-proofing: An evaluation of heat mitigation measures at the micro-scale. *Urban Forestry and Urban Greening*, *20*, 305–316. https://doi.org/10.1016/j.ufug.2016.09.011

Appendix A

BASH script used in tandem with MySQL script (Appendix B) that passes the positional parameters of year and month ($1 / $2, respectively) from a list of dates called in the same command.

```
#!/bin/bash

filename="$1_$2_av_hr"

mysql -u (USERNAME) -p (PASSWORD) -P3306 -h (SERVER) -p`cat
/etc/security/mysql/(LOCATIONOFPASSWORD)`> ./${1}/${filename}.csv  <<STOP

SET time_zone='-08:00';
SET @table:='$1_$2';
SET @select:="SELECT
                    DATE_FORMAT(FROM_UNIXTIME(timekey), '%Y-%m-%d
%H:00:00') AS Hours,
                    station.name AS stn,
                    station.id AS stn_id,
                    sensor.id AS sen_id,
                    stn_coordinates.elevation as Elevation,
                    FORMAT(stn_coordinates.latitude,8) as Latitude,
                    (FORMAT(stn_coordinates.longitude,8)-360) as Longitude,
                    COUNT(value) AS cnt,
                    FORMAT(AVG(value), 1) AS avg_hrly";
SET @from1:="FROM sdata_";
SET @from2:=" as Year,sensor,station,stn_coordinates ";

SET @where:="WHERE fieldid=40 AND sensor.id=Year.sensorid AND station.id<>0
AND station.id<>32767 AND station.id IS NOT NULL AND station.id=sensor.stationid
AND stn_coordinates.id=station.id
GROUP BY Sensorid, Hours
ORDER BY stn, Hours";

SET @stmt:=concat(@select," ",@from1,@table,@from2,@where);

prepare query from @stmt;
execute query;

\q

STOP
test $? = 0 && echo "$1_$2 Batch job ended well"
```

Appendix B

MySQL script that uses nested averaging functions to produce average hourly irradiance for each station, for a particular month (June in this case), from a 10 year (2005 – 2014, inclusive) period.

```
SELECT Hours, Station, Sensorid,AVG(avg_irradiance) AS avg_hourly_irradiance,
COUNT(avg_irradiance) AS Cnt,
stn_coordinates.elevation as Elevation,
format(stn_coordinates.latitude,8) as Latitude,
(format(stn_coordinates.longitude,8)-360) as Longitude
FROM
        ((SELECT
                DATE_FORMAT(FROM_UNIXTIME(timekey), '%m-%d-%H') AS Hours,
                station.name AS Station,
                sensor.id AS Sensorid,
                AVG(value) AS avg_irradiance
        FROM
                sdata_2005_06 Year,sensor,station
        WHERE
                fieldid=40 AND station.id=sensor.stationid
                AND sensor.id=Year.sensorid
                AND station.id<>0 AND station.id<>32767 AND station.id IS NOT NULL
        GROUP BY sensorid, Hours)
        UNION ALL
        (SELECT
                DATE_FORMAT(FROM_UNIXTIME(timekey),'%m-%d-%H') AS Hours,
                station.name AS Station,
                sensor.id AS Sensorid,
                AVG(value) AS avg_irradiance
        FROM
                sdata_2006_06 Year,sensor,station
        WHERE
                fieldid=40 AND station.id=sensor.stationid
                AND sensor.id=Year.sensorid
                AND station.id<>0 AND station.id<>32767 AND station.id IS NOT NULL
        GROUP BY sensorid, Hours)
        UNION ALL
        (SELECT
                DATE_FORMAT(FROM_UNIXTIME(timekey),'%m-%d-%H') AS Hours,
```

```
                station.name AS Station,
                sensor.id AS Sensorid,
                AVG(value) AS avg_irradiance
        FROM
                sdata_2007_06 Year,sensor,station
        WHERE
                fieldid=40 AND station.id=sensor.stationid
                AND sensor.id=Year.sensorid
                AND station.id<>0 AND station.id<>32767 AND station.id IS NOT
NULL
        GROUP BY sensorid, Hours)
        UNION ALL
        (SELECT
                DATE_FORMAT(FROM_UNIXTIME(timekey), '%m-%d-%H') AS
Hours,
                station.name AS Station,
                sensor.id AS Sensorid,
                AVG(value) AS avg_irradiance
        FROM
                sdata_2008_06 Year,sensor,station
        WHERE
                fieldid=40 AND station.id=sensor.stationid
                AND sensor.id=Year.sensorid
                AND station.id<>0 AND station.id<>32767 AND station.id IS NOT
NULL
        GROUP BY sensorid, Hours)
        UNION ALL
        (SELECT
                DATE_FORMAT(FROM_UNIXTIME(timekey), '%m-%d-%H') AS
Hours,
                station.name AS Station,
                sensor.id AS Sensorid,
                AVG(value) AS avg_irradiance
        FROM
                sdata_2009_06 Year,sensor,station
        WHERE
                fieldid=40 AND station.id=sensor.stationid
                AND sensor.id=Year.sensorid
                AND station.id<>0 AND station.id<>32767 AND station.id IS NOT
NULL
        GROUP BY sensorid, Hours)
        UNION ALL
        (SELECT
                DATE_FORMAT(FROM_UNIXTIME(timekey), '%m-%d-%H') AS
Hours,
                station.name AS Station,
```

```
		sensor.id AS Sensorid,
		AVG(value) AS avg_irradiance
	FROM
		sdata_2010_06 Year,sensor,station
	WHERE
		fieldid=40 AND station.id=sensor.stationid
		AND sensor.id=Year.sensorid
		AND station.id<>0 AND station.id<>32767 AND station.id IS NOT
NULL
	GROUP BY sensorid, Hours)
	UNION ALL
	(SELECT
		DATE_FORMAT(FROM_UNIXTIME(timekey), '%m-%d-%H') AS
Hours,
		station.name AS Station,
		sensor.id AS Sensorid,
		AVG(value) AS avg_irradiance
	FROM
		sdata_2011_06 Year,sensor,station
	WHERE
		fieldid=40 AND station.id=sensor.stationid
		AND sensor.id=Year.sensorid
		AND station.id<>0 AND station.id<>32767 AND station.id IS NOT
NULL
	GROUP BY sensorid, Hours)
	UNION ALL
	(SELECT
		DATE_FORMAT(FROM_UNIXTIME(timekey), '%m-%d-%H') AS
Hours,
		station.name AS Station,
		sensor.id AS Sensorid,
		AVG(value) AS avg_irradiance
	FROM
		sdata_2012_06 Year,sensor,station
	WHERE
		fieldid=40 AND station.id=sensor.stationid
		AND sensor.id=Year.sensorid
		AND station.id<>0 AND station.id<>32767 AND station.id IS NOT
NULL
	GROUP BY sensorid, Hours)
	UNION ALL
	(SELECT
		DATE_FORMAT(FROM_UNIXTIME(timekey), '%m-%d-%H') AS
Hours,
		station.name AS Station,
		sensor.id AS Sensorid,
```

```
                AVG(value) AS avg_irradiance
        FROM
                sdata_2013_06 Year,sensor,station
        WHERE
                fieldid=40 AND station.id=sensor.stationid
                AND sensor.id=Year.sensorid
                AND station.id<>0 AND station.id<>32767 AND station.id IS NOT
NULL
        GROUP BY sensorid, Hours)
        UNION ALL
        (SELECT
                DATE_FORMAT(FROM_UNIXTIME(timekey), '%m-%d-%H') AS
Hours,
                station.name AS Station,
                sensor.id AS Sensorid,
                AVG(value) AS avg_irradiance
        FROM
                sdata_2014_06 Year,sensor,station
        WHERE
                fieldid=40 AND station.id=sensor.stationid
                AND sensor.id=Year.sensorid
                AND station.id<>0 AND station.id<>32767 AND station.id IS NOT
NULL
        GROUP BY sensorid, Hours)) AS unionofavgyrltables, stn_coordinates, sensor
   where stn_coordinates.id=sensor.stationid AND Sensorid = sensor.id
GROUP BY Hours, Station
ORDER BY Station, Hours
```

Appendix C

ArcGIS geoprocessing script for interpolation and creation of a time-enabled mosaic dataset of interpolated surfaces points for each day of the year using Empirical Bayesian Kriging.

```
import arcpy, datetime
# Check out the ArcGIS Spatial Analyst extension for using the interpolation tool
arcpy.CheckOutExtension("spatial")
arcpy.CheckOutExtension("GeoStats")
arcpy.env.overwriteOutput = True
arcpy.env.workspace = r"C:\\Users\\Chris\\Desktop\\interpolation\\Interpolation.gdb"

# Get the layer time properties
lyr =
arcpy.mapping.Layer(r"C:\\Users\\Chris\\Desktop\\interpolation\\k_daily_plotted.lyr")
lyrTime = lyr.time

# Calculate the number of iterations based on the time extent and timestep interval
startTime = lyrTime.startTime
endTime = lyrTime.endTime
timeExtent = endTime - startTime
timeStepInterval = lyrTime.timeStepInterval

iterations = timeExtent.days / timeStepInterval.interval

# Get the time field containing the time values associated
# with the data in the time-enabled layer
startTimeField = str(lyrTime.startTimeField)

# Specify the output mosaic dataset to which the interpolated rasters will be added
outputMosaicDataset =
r"C:\\Users\\Chris\\Desktop\\interpolation\\interpolation.gdb\\A_FINAL_EBK_bessel"

i = 0
while i <= iterations:
   # Formulate the time query and increment the time by the timeStepInterval
   currentTime = str(startTime + (i*timeStepInterval))
   timeQuery = "\"" + startTimeField + "\"" + " = date '" + currentTime + "'"

   # Create an in-memory feature layer containing points that are valid at each timestep
   tempFeatureLyr = "tempTimeLayer" + str(i)
   arcpy.MakeFeatureLayer_management(lyr, tempFeatureLyr, timeQuery)

   # Create an interpolated raster surface using the points valid at each timestep
   outRaster =
```

```
r"C:\\Users\\Chris\\Desktop\\interpolation\\interpolation.gdb\\A_FINAL_EBK_bessel" +
(str(i)).zfill(4)
    print outRaster
    arcpy.EmpiricalBayesianKriging_ga(tempFeatureLyr, "k_daily", "",outRaster, "250",
"EMPIRICAL", "100", "1", "100", "NBRTYPE=StandardCircular RADIUS=78773
ANGLE=0 NBR_MAX=15 NBR_MIN=10 SECTOR_TYPE=ONE_SECTOR",
"PREDICTION", "0.5", "EXCEED", "", "K_BESSEL")

    # Add the newly created raster surface to a Mosaic Dataset
    arcpy.AddRastersToMosaicDataset_management(outputMosaicDataset, "Raster
Dataset", outRaster)

    i = i + 1

# Calculate the statistics on the output Mosaic Dataset for
# classifying data after new rasters are added
arcpy.CalculateStatistics_management(outputMosaicDataset,"1","1","#")
```

Appendix D

Python script that prepares arguments/files/parameters for running another script containing the diffuse fraction standard models.

```
#!/usr/bin/env python3
import sys
import os
from Models import *
# Title: CalculateDiffuseFraction.py
# Author: Chris Krasowski
# Input: 0 or more command line arguments and models from the Model.py file
#               None: Provides user information on the available command line
arguments
#               --list: Displays a list of available models to run on a csv
#               filename: Runs all available models on the csv
#               filename [models]: Runs any models given with the filename on the csv
# Output: A single csv file containing the results of the spcified models
#               or None (Input == None or Input == --list)

#Constants

DOY_COLUMN = 0
GLOBAL_RADIATION_COLUMN = -1


def Apply_Scaling_Factor(Scaling_Factor, Value_To_Scale):
        """Input: a scaling factor and a value to scale; Output: The value scaled by the
factor provided
                Applies the scaling factor"""
        return float(Scaling_Factor) * float(Value_To_Scale)

def Check_for_Scaling():
        """Input: None; Output: User's decision to scale and scaling factors
                Asks the user for input on whether to include a scaling factor with the
output"""
        print("Would You like to apply scaling to the models?")
        while True:
                Answer = raw_input("(Y or N)")
                if Answer.lower() == "n" or Answer.lower() == "no":
                        return False, -1, -1
                elif Answer.lower() == "y" or Answer.lower() == "yes":
                        print("Please input the value to scale the global irradiance")
                        Scales = []
                        while True:
```

```
                Answer = raw_input("Please input a number between 0-
1: ")
                try:
                    if float(Answer) >= 0 and float(Answer) <= 1:
                        Scales.append(float(Answer))
                        break
                except:
                    pass
                print("Not a valid scaling factor")
            print("Please input the value to scale the diffuse irradiance")
            while True:
                Answer = raw_input("Please input a number between 0-1:
")
                try:
                    if float(Answer) >= 0 and float(Answer) <= 1:
                        Scales.append(float(Answer))
                        break
                except:
                    pass
                print("Not a valid scaling factor")
            return True, Scales[0], Scales[1]
        else:
            print("Invalid input")

def Write_To_Ouput_File(Results, Output_File, Model, Day_Of_Year,
Global_Radiation, Scaling = False, Global_Scaling_Factor = 1, Diffuse_Scaling_Factor =
1):
    """Input: Result of a Model, an Ouput file, the model, the day of year and the
Global_Radiation; Output: The string written to file
        Writes the results to the specified output file"""
    if Scaling:
        Output_String = "%s,%s,%.4f,%.4f,%.4f,%.4f\n" % (Day_Of_Year,
Model.__name__, float(Global_Radiation), Results,
Apply_Scaling_Factor(Global_Scaling_Factor,
            Global_Radiation),
Apply_Scaling_Factor(Diffuse_Scaling_Factor, Results))
    else:
        Output_String = "%s,%s,%.4f,%.4f\n" % (Day_Of_Year,
Model.__name__, float(Global_Radiation), Results)
    Output_File.write(Output_String)
    return Output_String

def Split_Line(Line):
    """Input: any string; Output: Numeric values from the string or None if < 2
numeric values
        Splits the input line into numeric components"""
```

```
    Line_List = Line.split(",")
    if len(Line_List) < 2 or Line_List[0].isalpha():
        return None
    Output_List = []
    for i in Line_List:
        Output_List.append(i.strip())
    return Output_List

def Get_Models():
    """Input: None; Output: List of models from the Models.py file
        Reads the Models.py file and adds any function the list of available
models"""
    Model_File = open("Models.py", "r")
    Model_List = []
    for Line in Model_File:
        if Line.startswith("def"):
            Line_Split = Line.split(" ")
            Line_Split = Line_Split[1].split("(")
            Model_List.append(globals()[Line_Split[0]])
    return Model_List

def Get_Output_Filename(Filename):
    """Input: Filename to change; Output: New Filename
        Adds _with_diffuse followed by the extension to the original filename"""
    Filename = Filename.split(".")
    New_Filename = Filename[0]
    for i in Filename[1:-1]:
        New_Filename += "." +i
    New_Filename += "_with_diffuse."+ Filename[-1]
    return New_Filename

def Run_Calculation(Filename, Models, Scaling = False, Global_Scaling_Factor = 1,
Diffuse_Scaling_Factor = 1):
    """Input: A filename and a list of models; Output: The model(s) run through the
script
        Runs through each line of the input file and applies the model to the file; if
a scaling factor is provided applies the scaling factor"""
    try:
        Input_File = open(Filename, "r")
    except FileNotFoundError:
        print("%s Not Found, please ensure %s is correct and try again" %
(Filename, Filename))
        return None
    Filename = Get_Output_Filename(Filename)
    Output_File = open(Filename, "w")
    for Lines in Input_File:
```

```
        Numbers = Split_Line(Lines)
        if Numbers == None:
            if Lines != "\n":
                if Scaling:

    Output_File.write("DOY,Model,Global,Diffuse,GlobalScaled(%f),DiffuseScaled
(%f)\n" % (Global_Scaling_Factor, Diffuse_Scaling_Factor))
                else:
                    Output_File.write("DOY,Model,Global,Diffuse\n")
            continue
        for Single_Model in Models:
            Output =
Single_Model(Numbers[GLOBAL_RADIATION_COLUMN])
            if Output == None:
                continue
            Write_To_Ouput_File(Output, Output_File, Single_Model,
Numbers[DOY_COLUMN], Numbers[GLOBAL_RADIATION_COLUMN], Scaling,
Global_Scaling_Factor, Diffuse_Scaling_Factor)
    Input_File.close()
    Output_File.close()
    return Models

def Main():
    """Input: None; Ouput: None
        Checks commandline arguments for parameters and ask if the user wants
to apply a scaling factor"""
    All_Models = Get_Models()
    # User passes --list to the script
    if len(sys.argv) > 1 and sys.argv[1] == "--list":
        for i in All_Models:
            print("%s:\n%s\n" % (i.__name__, i.__doc__))
        exit()
    # User passes just a files to the script
    elif len(sys.argv) == 2:
        Scaling, Global_Scaling_Factor, Diffuse_Scaling_Factor =
Check_for_Scaling()
        Models_Run = Run_Calculation(sys.argv[1], All_Models, Scaling,
Global_Scaling_Factor, Diffuse_Scaling_Factor)
    # User passes the file and a list of models to the script
    elif len(sys.argv) > 2:
        Models = []
        for i in sys.argv[2:]:
            for k in All_Models:
                if i == k.__name__:
                    Models.append(globals()[i])
                    break
```

```
            if i in globals() and globals()[i] in Models:
                continue
            print("%s is not a valid model" % i)
        if len(Models) == 0:
            exit("No models were successfully passed to the script exiting...")
        Scaling, Global_Scaling_Factor, Diffuse_Scaling_Factor = Check_for_Scaling()
        Models_Run = Run_Calculation(sys.argv[1], Models, Scaling, Global_Scaling_Factor, Diffuse_Scaling_Factor)
    # User passes no arguments with the script
    else:
        exit("%s: missing file operand.\nUsage: %s FILENAME [MODELS]\nUse --list to get model names" % (os.path.basename(__file__), os.path.basename(__file__)))
    if Models_Run == None:
        exit()
    for i in Models_Run:
        print("%s run successfully" % i.__name__)

if __name__ == "__main__":
    Main()
```

Appendix E

Python Script containing diffuse fraction models that get called in to the CalculateDifuseFraction.py execution script as functions.

```
#!/usr/bin/env python3
# Title: Models.py
# Author: Chris Krasowski
#The functions in this file will be imported into the CalcluateDiffuseFraction.py script
#automatically
# The doc string for each model will be displayed when the user uses the --list argument
# Any function added to this file must take Irradiance as its only input and must output a
float

import math


def Orgill_Hollands(Irradiance):
	"""kd = 1.557 - 1.84 * kt for 0.35 <= kt <= 0.75; kd = 1.0 - 0.249 * kt for kt <
0.35; and kd = 0.177 for kt > 0.75"""
	Irradiance = float(Irradiance)
	if Irradiance < 0.35:
		return 1 - (0.249*Irradiance)
	elif Irradiance <= 0.75 and Irradiance >= 0.35:
		return 1.557 - (1.84*Irradiance)
	elif Irradiance > 0.75:
		return 0.177

def Reindl_Et_Al(Irradiance):
	"""kd = 1.45 - 1.67 *kt for 0.3 < kt > 0.78; kd = 1.02 - 0.248 * kt for kt <= 0.3,
and kd = 0.147 for kt >= 0.78"""
	Irradiance = float(Irradiance)
	if Irradiance <= 0.3:
		return 1.02 - (0.248 * Irradiance)
	elif Irradiance > 0.3 and Irradiance < 0.78:
		return 1.45 - (1.67 * Irradiance)
	elif Irradiance >= 0.78:
		return 0.147

def Boland_Et_Al(Irradiance):
	"""1/(1+e^(7.997(kt -0.586)))"""
	Irradiance = float(Irradiance)
	a = Irradiance - 0.586
	a = a*7.997
```

```
    return 1 / (1 + math.pow(math.e,a))

def Hawlader(Irradiance):
    """kd = 1.135 - 0.9422 * kt - 0.3878 * kt^2 for 0.225 < kt < 0.775; kd = 0.915 for
kt <= 0.225 and kd = 0.215 for kt >= 0.775"""
    Irradiance = float(Irradiance)
    if Irradiance <= 0.225:
        return 0.915
    elif Irradiance > 0.225 and Irradiance < 0.775:
        return 1.135 - (0.9422 * Irradiance) - (0.3878 * (Irradiance ** 2))
    elif Irradiance >= 0.775:
        return 0.215

def Miguel_Et_Al(Irradiance):
    """kd = 0.724 + 2.738 * kt - 8.32 * kt^2 + 4.967 * kt^3 for 0.21 < kt < 0.76; kd =
0.995 - 0.081 * kt for kt <= 0.21 and kd = 0.18 for kt >= 0.76"""
    Irradiance = float(Irradiance)
    if Irradiance <= 0.21:
        return 0.995 - (0.081 * Irradiance)
    elif Irradiance > 0.21 and Irradiance < 0.76:
        return 0.724 + (2.738 * Irradiance) - (8.32 * (Irradiance ** 2)) + (4.967 *
(Irradiance ** 3))
    elif Irradiance >= 0.76:
        return 0.18

def Karatasou_Et_Al(Irradiance):
    """kd = 0.9995 - 0.05 * kt - 2.4156 * kt^2 + 1.4926 * kt^3 for 0 < kt <= 0.78; and
kd = 0.20 for kt > 0.78"""
    Irradiance = float(Irradiance)
    if Irradiance > 0 and Irradiance <= 0.78:
        return 0.9995 - (0.05 * Irradiance) - (2.4156 * (Irradiance ** 2)) +
(1.4926 * (Irradiance ** 3))
    elif Irradiance > 0.78:
        return 0.20

def Erbs_Et_al(Irradiance):
    """kd = 0.951 - 0.1604 * kt + 4.388 * kt^2 - 16.638 * kt^3 + 12.336 * kt^4 for
0.22 < kt <= 0.80; kd = 1.0 - 0.09 * kt for kt <= 0.22 and kd = 0.165 for kt > 0.80"""
    Irradiance = float(Irradiance)
    if Irradiance <= 0.22:
        return 1.0 - (0.09 * Irradiance)
    elif Irradiance > 0.22 and Irradiance <= 0.80:
        return 0.951 - (0.1604 * Irradiance) + (4.388 * (Irradiance ** 2)) -
(16.638 * (Irradiance ** 3)) + (12.336 * (Irradiance ** 4))
    elif Irradiance > 0.80:
        return 0.165
```

```
def Chandrasekaren_and_Kumar(Irradiance):
	"""kd = 0.9686 + 0.1325 * kt + 1.4183 * kt^2 - 10.1862 * kt^3 + 8.3733 * kt^4
for 0.24 < kt <= 0.80; kd = 1.0086 - 0.178 * kt for kt <= 0.24, and kd = 0.197 for kt >
0.80"""
	Irradiance = float(Irradiance)
	if Irradiance <= 0.24:
		return 1.0086 - (0.178 * Irradiance)
	elif Irradiance > 0.24 and Irradiance <= 0.80:
		return 0.951 + (0.1325 * Irradiance) + (1.4183 * (Irradiance ** 2)) -
(10.1862 * (Irradiance ** 3)) + (8.3733 * (Irradiance ** 4))
	elif Irradiance > 0.80:
		return 0.197

def Oliveira_Et_Al(Irradiance):
	"""kd = 0.97 + 0.8 * kt - 3.0 * kt^2 - 3.1 * kt^3 + 5.2 * kt^4 for 0.17 < kt <=
0.75; kd = 1.0 for kt <= 0.17, and kd = 0.17 for kt > 0.75"""
	Irradiance = float(Irradiance)
	if Irradiance <= 0.17:
		return 1.0
	elif Irradiance > 0.17 and Irradiance <= 0.75:
		return 0.97 + (0.8 * Irradiance) - (3.0 * (Irradiance ** 2)) - (3.1 *
(Irradiance ** 3)) + (5.2 * (Irradiance ** 4))
	elif Irradiance > 0.75:
		return 0.17

def Soares_Et_Al(Irradiance):
	"""kd = 0.90 + 1.1 * kt - 4.5 * kt^2 + 0.01 * kt^3 + 3.14 * kt^4 for 0.17 < kt <=
0.75; kd = 1.0 for kt <= 0.17, and kd = 0.17 for kt < 0.75"""
	Irradiance = float(Irradiance)
	if Irradiance <= 0.17:
		return 1.0
	elif Irradiance < 0.17 and Irradiance <= 0.75:
		return 0.90 + (1.1 * Irradiance) - (4.5 * (Irradiance ** 2)) + (0.01 *
(Irradiance ** 3)) + (3.14 * (Irradiance ** 4))
	elif Irradiance > 0.75:
		return 0.17

if __name__ == "__main__":
	Main()
```

Appendix F

The Python Solar Analyst geoprocessing script that includes raster file name handling and parallel (multiprocessing) processing functions.

```
import multiprocessing
import time
import arcpy
import os

def split_lines(line):
        """this splits the lines that get split outside in the final_function"""
        the_split= line.split(",")
        DOY = the_split[0]
        k_daily = the_split[-2]
        diffuse = the_split[-1]
        return DOY, k_daily, diffuse

def get_inRaster(DOY):
        """return the address of the copied raster in each temp folder specific to each raster_DOY"""
        temp_directory = r"C:\data\FINAL_TEST\temp\raster_"+ str(DOY)
        inRaster = temp_directory+ "\idwnatflt_final_copy.tif"
        return inRaster, temp_directory

def final_function(line):
        start_time= time.time()
        arcpy.CheckOutExtension("Spatial")
        arcpy.env.overwriteOutput = True

        # Assign the variables out of split_lines into new vars called DOY, K_daily, diffuse
        DOY, k_daily, diffuse = split_lines(line)
        # Bring the variables from get_inRaster function into the local variable scope
        inRaster, temp_directory = get_inRaster(DOY)
        arcpy.env.scratchWorkspace = temp_directory
        latitude = 48.4222
        skySize = 200
        timeConfig = arcpy.sa.TimeWithinDay(DOY,0, 24)
        dayInterval = 14
        hourInterval = 0.2
        zFactor = 1
        calcDirections = 32
        zenithDivisions = 18
        azimuthDivisions = 16
        diffuseProp = diffuse
```

```
    transmittivity = k_daily
    outDirectRad = ""
    outDiffuseRad = ""
    outDirectDur = ""

    # Execute AreaSolarRadiation
    outGlobalRad = arcpy.sa.AreaSolarRadiation(inRaster, latitude, skySize,
timeConfig,
      dayInterval, hourInterval, "NOINTERVAL", zFactor, "FROM_DEM",
      calcDirections, zenithDivisions, azimuthDivisions, "UNIFORM_SKY",
      diffuseProp, transmittivity, outDirectRad, outDiffuseRad, outDirectDur)

    # Save the output
    outGlobalRad.save(r"C:\data\FINAL_TEST\outputs\global_"+str(DOY).zfill(4)+
"\global_"+str(DOY).zfill(4))
    end_time = time.time()
    outputfile=open("outputfile.txt","a")
    outputfile.write("\nthe model run for " + str(DOY) + " DOY has completed
successfully")
    outputfile.write(" and took %f seconds to run\n" % (end_time - start_time))
    outputfile.close()
#To test this script only passing manual DOY/ atm params use the below
#if __name__ == "__main__":
#    final_function("266,0.4269347,0.771440152")


def main():
    start= time.time()
    output_file = open("outputfile.txt", "a")
    output_file.write("\nThe entire script started at " +str(time.ctime(start)))
    output_file.close()
    # Check out any necessary licenses
    arcpy.env.workspace = r"C:\data\FINAL_TEST\final_test"
    arcpy.env.overwriteOutput = True
    filename = "k_daily_annual.txt"
    input_file = open(filename, "r")
    lines_from_filename = []
    for i in input_file:
        lines_from_filename.append(i)
    p = multiprocessing.Pool(12)
    p.map(final_function, lines_from_filename)
    # Put in a timestamp at the end of the script
    end = time.time()
    duration = end - start
    hours, remainder = divmod(duration, 3600)
    minutes, seconds = divmod(remainder, 60)
```

```
    output_file = open("outputfile.txt", "a")
    output_file.write("\nThe entire script started at " +str(time.ctime(start))+ " and finished at " +str(time.ctime(end)))
    output_file.write("\nThe entire script completed in %dh:%dm:%fs" % (hours, minutes, seconds))
    output_file.close()
    p.close()
    p.join()
if __name__=='__main__':
    main()
```

Appendix G

Python script used to handle Arcpy error associated with folders and rasters in Solar Analyst (in_Raster needing to be in its own unique folder). The script copies the DSM “idwnatflt_final.tif” into a folder named with the DOY appended, scrubbed from the k_daily file.

```
import os
import shutil

def get_inRaster(DOY):
    """copies the inraster to a temporary folder, returns the address to this folder"""
    temp_directory = r"C:\data\FINAL_TEST\temp\raster_"+ str(DOY)
    out_directory = r"C:\data\FINAL_TEST\outputs\global_"+str(DOY).zfill(4)
    #First make sure that if a directory is made that already exists we handle the
exception with "except OSError: pass" statement.
    try:
        os.mkdir(temp_directory)
    except OSError:
        pass
    try:
        os.mkdir(out_directory)
    except OSError:
        pass
    #Copy the master raster into the newly created directory. Arcpy error forces us to
put raster into its own unique temp dir - sharing error.
    shutil.copyfile(r"C:\data\FINAL_TEST\inputs\idwnatflt_final.tif",
temp_directory+ "\idwnatflt_final_copy.tif")
filename = r"C:\data\LFINAL_TEST\k_daily.txt"
input_file = open(filename, "r")
for line in input_file:
    the_split= line.split(",")
    DOY = the_split[0]
    get_inRaster(DOY)
```